UNIVERSITY OF OSLO
Institutt for geofag Avdeling
MetOs

Characteristics of cirrus clouds over ALOMAR and their dependence on atmospheric conditions

Masteroppgave i geofag; meteorologi og oseanografi

Nina Elisabeth Larsgård

25th April 2008

Abstract

This thesis is a short investigation of cirrus clouds above the ALOMAR observatory at Andøya. Ice clouds are one of the main uncertainties in the cloud effects in atmospheric modelling. Especially ice clouds in the arctic need further investigation.

This study uses the Tropospheric Lidar at ALOMAR to investigate some aspects, as cloud top and base heights, optical depth and ice crystal shape, of ice clouds above Andøya(69°N 16°E). The LIDAR is an instrument well suited to investigate the smaller particles in the atmosphere as it operates on shorter wavelengths than for example the RADAR. A short one year climatology has been given as an overview of the cloud occurrence in the LIDAR data from 2006. The cloud altitudes have also been found from the LIDAR data using existing algorithms, and along with temperature data from radiosondes have these altitudes been compared with cloud data from the CALIPSO satellite. The CALIPSO satellite carries a LIDAR system (CALIOP) that makes vertical profiles of the atmosphere.

The height is found by comparing the LIDAR signal to a threshold found in a cloud and aerosol free region above the cloud. The optical depth has been extracted from the LIDAR signal with the particular integration method from Cadet et al. (2005). The ratio between the two polarizations of the 532 nm channel has been found to investigate the shape of the ice crystals. The connection between the weather situation in each case and the clouds found in the LIDAR data is also shown in this thesis.

The height results show that the clouds found in the ALOMAR data is mostly cirrus clouds because of their high altitude and low temperatures. The optical depth classified the clouds investigated as thin to opaque in two of the cases, and the last case was classified as an opaque cirrus to thin altostratus. The depolarization ratio results show that at least for the cases used in this thesis will often some parts of the cirrus clouds consist of horizontally oriented ice crystals. They also seem to consist mostly of platelike crystals. This is interesting because many other studies have shown that irregular crystals are more common. However, test should be made to confirm that the results in this thesis are correct.

The cirrus clouds investigated in this thesis were connected to large frontal systems. The cirrus clouds are located some distance away from the fronts, and the cloud cover thickens as the front moves closer. The clouds deepen towards altostratus type cloud as the front moved closer, this have also been seen in one of the cases presented in this thesis.

Acknowledgements

First of all, I would like to thank my supervisor Jón Egill Kristjánsson. He gave me the opportunity to work with a subject that I really wanted to work with, and has been really helpful throughout this process. Bertrand Cadet also deserves a lot of credit for answering all my questions, helping me with my writing and with my programs. Without him would this have taken a lot more time than it has done. My co-supervisor Frode Stordal also deserves thanks for all help during the last year. I was lucky enough to visit the ALOMAR facility during January 2007 and I would like to thank Michael Gausa, which also served as my co-supervisor, and the rest of the people at ALOMAR for a great visit. All the other people that I have met trough the work with my thesis, including Max Frioud, Carlos Toledano, Gunnar Wollan, Bjørn Røsting and Kerstin Stebel, also deserves a thank you for their help and inspiration.

The other students at the MetOs department have also been a great inspiration to me, and we have had lots of fun during the last years. I am also really grateful to my friends outside the meteorology and oceanography department which made me relax and kept me from obsessing too much with this thesis. I would also like to thank my parents for all the support they have given me throughout my studies. At last I would like to thank my dear Nicolay who has listened to all my ranting a bout cirrus clouds and Matlab programs and fixed annoying things at my computer.

Nina Elisabeth Larsgård
25th April 2008

> Nothing in life is to be feared, it is only to be understood. Now is the time to understand more, so that we may fear less
>
> — *Marie Curie*

The ALOMAR data was compared with data from the CALIPSO satellite, these data were obtained from the NASA Langley Research Center Atmospheric Science Data Center. Satellite images were obtained from the Dundee satellite station (http://www.sat.dundee.ac.uk/) and radiosonde profiles were obtained from the University of Wyoming
(http://weather.uwyo.edu/upperair/sounding.html). Weather charts have been made by DNMI.

Contents

Chapter 1

Introduction

Climate change has become one of the most talked of subjects during the last couple of years. IPCC presented their fourth assessment report: Climate Change 2007 early in 2007. This report stated, with more confidence than earlier that the observed increase in globally averaged temperatures originates mostly from an increase in anthropogenic emissions of greenhouse gases. Al Gore with his documentary "An Inconvenient truth", which premiered in the beginning of 2006, was another catalyst to the debate. This film brought some of the climate research closer to the public and was widely debated the following year. Al Gore and IPCC was awarded the Nobel Peace Prize in 2007 "for their efforts to build up and disseminate greater knowledge about man-made climate change, and to lay the foundations for the measures that are needed to counteract such change." (Committee, 2007).

There are however many factors that determine the climate that still needs to be better understood to remove some of the uncertainties in the climate models and in the IPCC

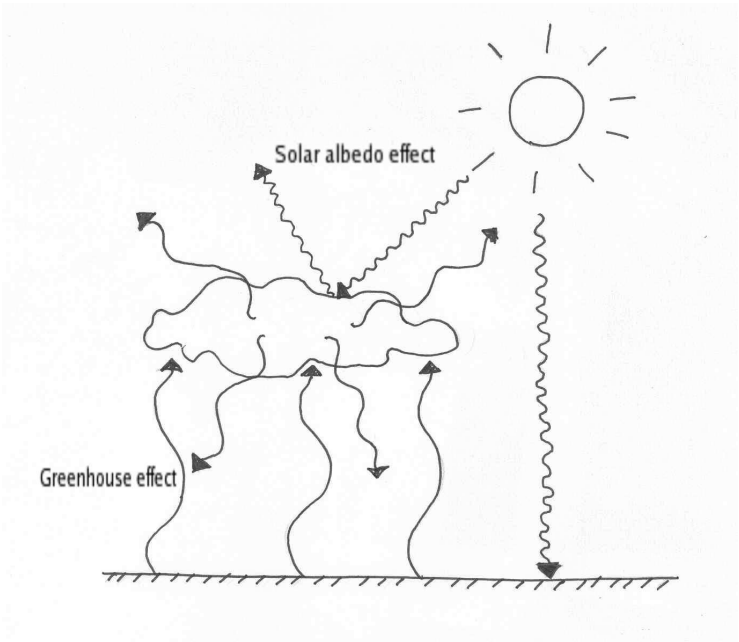

Figure 1.1: The solar albedo effect and the greenhouse effect of clouds. The solar albedo effect will reflect sunlight which leads to cooling. The Greenhouse effect will trap terrestrial radiation and cause a warming.

reports. Some of the major uncertainties are the effect of aerosols and clouds on the net radiative forcing. The clouds have both a cooling and a warming effect on the atmosphere due to the solar albedo effect and the greenhouse effect. Figure 1.1 shows how the sunlight is reflected off the top of the clouds due to the solar albedo effect which will lead to a cooling. The figure also shows how the long waved terrestrial radiation is absorbed by the clouds and re-emitted to the rest of atmosphere thereby causing a warming effect. For low- and middle-level clouds has it been found that the solar albedo effect dominates and they will have a net cooling effect on the earth's climate(Lynch et al., 2002). A net warming effect has been suggested for high level clouds as cirrus clouds. This is however not as clear as for the lower clouds, because the formation mechanisms and properties of the high cirrus clouds are not fully understood(Lynch et al., 2002).

The clouds will also act as feedback mechanisms in the earth's climate. Feedbacks can either be positive and increase the effect of a forcing, or negative and act to decrease the effect of a forcing. A general approach to feedback handling has been described in Lindzen et al. (2001). This article also describes the so called Iris-effect of high clouds, where the high cloudy areas will increase or decrease in response to changes in the surface temperature to counteract such changes. This hypothesis has been highly debated, but this emphasises the need for a better understanding of how the feedback mechanisms of high clouds are connected to the climate. The sea surface temperature(SST) has also been connected to the high cirrus clouds through feedback mechanisms, as described in Ramanathan and Collins (1991). This article states that a warmer ocean would cause more evaporation, which would lead to more high clouds. These high clouds would then lead to further warming because of the greenhouse effect, which would cause even more high clouds to form. The thermostat hypothesis presented in Ramanathan and Collins (1991) stated that this accumulated cirrus layer would eventually reflect enough sunlight to prevent further warming.

The effect of the ice crystals within cirrus clouds on the interaction between the cirrus clouds and the solar and terrestrial radiation has been a very uncertain part of this work. The following example of this uncertainty is given in the introduction of (Intrieri et al., 1993). A comparison with 15 GCM[1]s showed that these GMSs were much in agreement in simulations where clear sky was assumed. This changed when clouds where introduced. The sensitivity to climate forcing would then vary with as much as a factor of three between the different models, due to differences in the treatment of the clouds.

1.1 Description of earlier work

There have been several earlier investigations about ice crystal shapes and sizes. Some, for example Mason (1994) and Bailey and Hallett (2002), has used laboratory experiments that controlled temperatures, supersaturation and nucleation materials to find how and when the ice crystals formed. The Mason (1994) article describes a connection between air temperature, supersaturation and crystal habit found from experiments. This article reports a close connection between ice crystal shape and temperature, but it seems focused on the simplest forms of ice crystals. The Bailey and Hallett (2002) article goes beyond the simplest forms of ice crystals and finds polycrystals to be more usual than in earlier reports. Some flight campaigns have been made to retrieve information about ice crystals.

[1]General Circulation Models

The ASTAR experiment described in Gayet et al. (2007) was a flight campaign situated in the Arctic. This experiment used both in situ measurements from a Cloud Particle Imager (CPI) and other in situ instruments, and LIDAR data from an airborne LIDAR. The extinction values found from the LIDAR data was then compared with the in situ measurements.

Lidar measurements have been found useful for investigating the vertical structure of cirrus clouds and for finding more accurate cirrus cloud boundaries. Several techniques for retrieving the cloud base and top altitude from Lidar profiles are discussed in the Platt et al. (1994) article. These techniques were developed to be used to find statistics on cloud base height during the Experimental Cloud Lidar Pilot Study (ECLIPS). This study included several different Lidar systems and was specifically initiated to find good datasets on cloud-base altitude(Platt et al., 1994). Another extensive cirrus cloud study was presented in Goldfarb et al. (2001). In this study was the optical depth calculated for cirrus clouds found in a two-year analysis of lidar measurements from the Observatoire de Haute Provence(OHP). This showed that almost 20% of the detected cirrus clouds was subvisible cirrus, which are cirrus that are invisible for the human eye and with optical depths below 0.03. Other studies have connected the depolarization of the lidar signal from the 532 nm wavelength to scattering by different types if ice crystals. Extensive algorithms have been developed to make a connection between the shapes of the ice crystals and the depolarization ratio. Noel et al. (2002) uses ray-tracing code and lidar measurements to form a technique for classification of ice crystal shapes from this lidar depolarization ratio. This article also showed a strong dependence between temperature and ice crystal shape as many the former articles have done.

1.2 Description of the assignment

The reason for choosing this subject is a wish to improve the understanding of ice clouds. The connection between atmospheric conditions and ice crystal shape and size is especially important to investigate. Both shape and size are of major importance when finding the radiational properties of the ice crystals as, this affects how the radiation is scattered through ice crystals. This will again affect how the ice clouds contribute to the radiational balance through the greenhouse and solar albedo effects. Due to the high altitude and thin appearance of cirrus clouds has investigations of this problem shown difficult. In situ measurements are limited and expensive, although very useful for finding the ice crystals shape. The LIDAR is another instrument that is useful for finding information about cirrus clouds, which is the instrument used in this thesis. This instrument is sensitive to smaller particles than for example the RADAR, and is therefore especially useful for investigating cirrus clouds. The object of the work in this thesis has been to characterize some of the microphysical properties of ice crystals in cirrus clouds above Andøya(69°N,16°E). These properties have also been viewed in the context of meteorological conditions and temperature. Data from the tropospheric lidar at Andøya has been used and compared with additional data from the satellite CALIPSO. The CALIPSO[2] satellite carry an active downward facing LIDAR together with passive instruments to provide global information about aerosols and clouds(Liu et al., 2006)(Winker et al., 2003). The CALIPSO satellite was launched in spring 2006 and data from the beginning of June 2006 is available for

[2]Cloud-Aerosol LIDAR Infrared pathfinder Satellite Observations

comparisons with the ALOMAR data. The measurements from 2006 have therefore been chosen for the climatology in this thesis. Some cases have been chosen for a closer look on the clouds and to make some comparisons between the ALOMAR and CALIPSO data. Parameters that have been investigated in this work include cloud top and base altitudes, cloud optical thickness and depolarization ratio. Together will these variables give information about microphysical properties of the cloud. A special emphasis has been laid at the ice crystal shape, which can be partially understood by the depolarization ratio.

The first part of this document will present some theory and background information about cirrus clouds and use of the LIDAR. The second part describes the methods used to extract information about the heights, optical depth and depolarization ratio of the clouds. The third part presents the results which include a one-year climatology from the 2006 data and an analysis of some cases chosen from the latter part of 2006. The cloud top and base, optical depth and depolarization ratio are all presented for the clouds in each case. If the CALIPSO satellite passed close enough to the ALOMAR location(69°N, 16°E) is the height and location be compared with the CALIPSO data. The height and location is also compared with data from the CALIPSO satellite. At last have weather charts from The Norwegian Meteorological Institute (DNMI[3]) been used to connect the clouds to the weather situation in each case. The last part of this thesis will give an overall conclusion to the results found in the former section and possible further work will be presented.

[3]Det Norske Meteorologiske Institutt

Chapter 2

Cirrus clouds

The investigation of cirrus clouds can be made with several different approaches depending on the goal of the investigation. This chapter describes how cirrus clouds are defined and the place of the cirrus clouds among the other cloud types. This first section also describes some the different variations of cirrus clouds, as the cirrus radiatus cloud seen in figure 2.1. The different spatial scales that the cirrus clouds can be investigated on are also described. The information that can be found and the instrumentation that can be used on each scale are also presented

Figure 2.1: Cirrus radiatus above the meteorological institute at Blindern, Oslo, (Photo: Nina E. Larsgård)

Genus	WMO abbreviation	height class
Cirrus	Ci	High clouds
Cirrocumulus	Cc	
Cirrostratus	Cs	
Altocumulus	Ac	Middle clouds
Altostratus	As	
Nimbostratus	Ns	
Stratocumulus	Sc	Low clouds
Stratus	St	
Cumulus	Cu	
Cumulonimbus	Cb	

Table 2.1: Main classification of clouds (Waagen Hans, 2006)

2.1 Definition and variations of cirrus clouds

The world meteorological organization (WMO) has categorized clouds into ten main types which can be classified according to their height: high, medium and low. This main classification can be seen in table 2.1. The ten main types, or cloud genera, can be further subdivided into cloud species and varieties according to structure or shape of the clouds (Dunlop, 2001). A more extensive table than 2.1 can be found in appendix A.

Numerous types and shapes of cirrus clouds can be found, but they are defined as being high, consisting of ice and they are generally stable and long lived. This definition is based, as the other cloud definitions, mostly on the visual properties of the cloud. The visual properties also distinguish the regular cirrus clouds from the two other types of high clouds; cirrostratus and cirrocumulus. Throughout this thesis will cirrus clouds mean all these three types of high clouds collectively. The regular cirrus clouds are usually fibrous small patches of clouds, and does not show the large spatial extent of the cirrostratus or the ripples and cloud patches that characterize the cirrocumulus(Alcorn, 2007). The contrail cirrus clouds that form in the exhaust of airplanes and the comma shaped cirrus unicus are perhaps the easiest types of cirrus to recognize. A striking variety of cirrus clouds is the cirrus radiatus, which form parallel bands that seem to converge towards the horizon. This type of cloud can be seen in figure 2.1 in the beginning of this chapter. Striking optical phenomena as halos and sundogs can also be contributed to thin cirrus cloud layers. The precipitation from cirrus clouds will not reach the ground. It evaporates some distance below the cloud base. The cirrus unicus displays a comma shape that appears due to precipitation of heavy ice crystals that fall into a layer with stronger winds that drag the ice crystals some distance before they sublimate. The height of cirrus clouds will be in the range 4 - 15 km, and will change with the seasons and the locations on which they appear. One classification of cirrus height vs. latitude can be seen in table 2.2. This table shows that the high clouds are highest in the tropical region. This is because the higher temperature of the tropical region will lead to a higher tropopause and the moist air will rise higher before clouds are formed.

étage	Polar Region	Temperate Region	Tropical Region
High	3 - 8 km	5 - 13 km	6 - 18 km
Middle	2 - 4 km	2 - 7 km	2 - 8 km
Low	0 - 2 km	0 - 2 km	0 - 2 km

Table 2.2: Typical cloud heights in different regions (Waagen Hans, 2006). The difference between the regions is caused by the differences in mean surface temperature.

Identification of cirrus clouds

Cirrus clouds can be visually identified by their fibrous and hair-like appearance. These clouds are normally optically thin and may, as an added problem to their investigation, be subvisible. Subvisible cirrus clouds are cirrus that can not be detected with the human eye, which have an optical depth that is lower than 0.03(Lynch et al., 2002). Cirrus clouds can also be identified with LIDARs as the ice crystals will change the polarization of the 532 nm wavelength. Clouds that show up in both of the polarizations of the 532nm light will therefore consist of ice.

The temperature at the base of the cloud can be a good first estimation of whether or not a cloud can be classified as a cirrus cloud. Ice crystals can exist when the temperature is below $0°C$, but it is possible to have ice, water or a mixture of the two in a cloud with cloud temperatures between 0 and approximately -40°C. This possibility arises because of the need of an ice nuclei to effectively freeze water droplets into ice crystals at temperatures below $-40°$. Supercooled water droplets may exist in abundance in temperatures down to approximately $-15°C$(Rogers and Yau, 1989). Ice crystals will gradually become the dominant cloud particle as the temperature decreases and both homogeneous and heterogeneous nucleation becomes more effective. Both of these nucleation methods will be further described in a later section in this thesis. The homogeneous nucleation method will become the dominant process in the $-45°C$ - $-35°C$ temperature range(Lynch et al., 2002). Clouds with temperatures lower than this range will therefore definitely consist of ice crystals only. However, ice crystals will begin to dominate in clouds with temperatures somewhat lower than $-15°C$. A temperature threshold for cirrus clouds have been set to approximately $-25°C$ in Goldfarb et al. (2001). This threshold, and the temperature range where homogeneous nucleation occurs, has been used in this thesis as a first step toward classifying the clouds in the cases as cirrus clouds.

2.2 Cirrus clouds on the global scale

Cirrus clouds are high ice clouds, which can be found globally and do not depend on latitude or whether the surface below is sea or land(Liou, 1986). The coverage by cirrus clouds is not well documented. Liou (1986) operates with a cirrus cloud coverage at about 20%, but other numbers, as 30%(Zhang and Mace, 2006) or even as high as 50-70((Lynch et al., 2002),(Noel et al., 2006)), have also been presented. One of the reasons for the low documentation of the cirrus cloud coverage is that they are optically thin. They can be difficult to detect both because they can be subvisual and because thicker, lower clouds

can obstruct their identification when the lidar is facing upward from the earth[1]. The impact of the cirrus clouds on the climate is difficult to find without proper estimation about the cirrus coverage. Human activities can also have an impact on the formation and coverage of cirrus clouds. Aviation induced clouds are usually cirrus formed in the exhaust of planes, and are called contrail clouds. Cirrus contrails form cloud streaks that are easily identified, one example is figure 2.2. These clouds had time to expand and become large sheets of clouds long after the planes had passed.

Figure 2.2: Contrail cirrus, (Photo: Nina E. Larsgård)

Proper collection of information about cirrus cloud coverage is needed to find the best estimates of the influence of the cirrus clouds on the radiational balance. One way to get global information about this is to use measurements made by satellites. Figure 2.3 shows one global map of the average of cirrus cloud cover in % of cloud cover. This figure is taken from Stordal et al. (2005), which is an article that discusses the effect of aircraft traffic on cirrus cloud cover. The figure is based on ISCCP[2] data. This project used data from several satellites both geostationary(METEOSAT, GMS and GOES) and polar orbiting(NOAA afternoon and morning orbiters)(Stordal et al., 2005). Other satellites that can be used to find this type of information are CLOUDSAT and CALIPSO. It can be seen from the figure, that the highest percentage of cirrus cloud cover can be found in the tropics and above landmasses as northern America, eastern Asia and Australia. The high amount of cirrus cover in the tropics is connected to the Intertropical Convergence Zone (ITCZ)(Lynch et al., 2002). Cumulonimbus convection will cause a high amount of cirrus formation in this area. High cirrus cover is usually connected to baroclinic fronts and lows, and orographic lifting for the landmasses outside the tropics.

[1]Airborne and spaceborne LIDARS are pointing downwards, in this case will higher clouds obstruct the lower ones.

[2]International Satellite Cloud Climatology Project

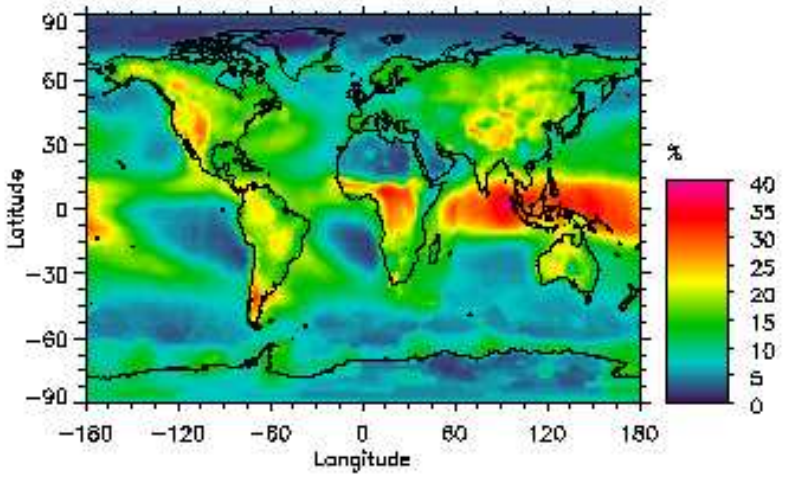

Fig. 1. Global map of average cirrus cover based on ISCCP VIS/IR data for the period 1984–1999 (in % cloud cover).

Figure 2.3: Global map of average cirrus cover based on ISCCP VIS/IR data for the period 1984-1999(in % of cloud cover). (Figure 1 in (Stordal et al., 2005))

2.2.1 Radiative impact of cirrus clouds

The radiative impact of cirrus clouds are an important factor in the global radiative budget. As can be seen in figure 2.4, cirrus clouds have both a solar albedo effect and a greenhouse effect. The solar albedo effect will reflect sunlight and lead to a cooling at the ground. The greenhouse effect will trap outgoing terrestrial radiation and lead to a warming at the ground. Several factors decide which of these two effects that dominates for each cloud. These effects include temperature, cloud height and the thermal contrast to the surface in addition the radiative properties of the cloud(Wang Pao, 2002). Dense clouds can usually be approximated as blackbodies[3] in the IR. The temperature of the cloud will then decide the outgoing infrared radiation flux through Stefan-Boltzmanns law ($F = \sigma T^4$, $\sigma = 5.67 \times 10^{-8} Jm^{-2}$). This temperature is closely connected to the cloud height. Cirrus clouds on the other hand can not be approximated as blackbodies due to their low optical depth. They can not be described as blackbodies because they generally consist of large ice crystals in low number densitiesLiou (1986). The assumption of localized thermodynamic equilibrium when concerning infrared emissions can therefore not be used. Their significance to the radiational budget comes from two different properties of the cirrus clouds. Firstly, the cirrus clouds are long-lasting and cover an extensive part of the atmosphere. Secondly, these clouds are located high in the atmosphere where the temperature is low. They will therefore have a strong interaction with any infrared radiation through Kirchoff's law(Wang Pao, 2002). But how much the cirrus clouds affect the radiational balance is closely connected to the radiative and microphysical properties of the individual cirrus clouds. These properties can vary greatly. Size and shape of the ice crystals varies with the atmospheric conditions, and these properties have a strong impact on how both solar and terrestrial radiation

[3]hypothetical body which absorbs all incoming radiation completely, and reemits with maximum possible emission(Wallace and Hobbs, 1977)

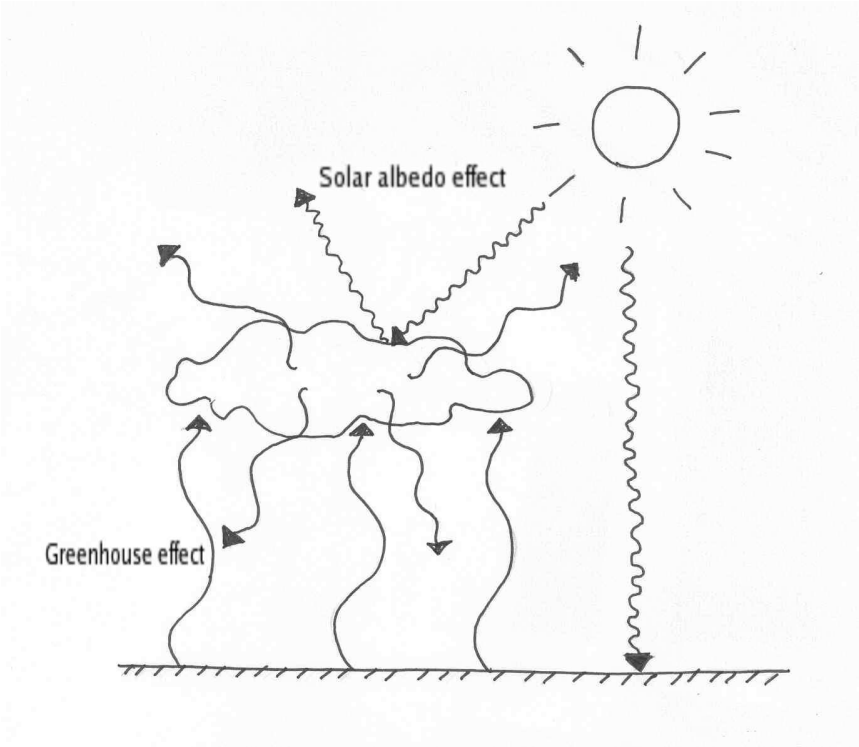

Figure 2.4: The solar albedo effect and greenhouse effect of clouds

interacts with the clouds. Properties as the volume absorption coefficient and the volume extinction coefficient are closely connected to the size distribution of the ice crystals, so any change in this distribution will give changes in the radiative forcing by the cloud(Wang Pao, 2002). Variations in cirrus height or cover will also affect the radiational effect of the clouds. If the cirrus clouds are lifted to higher altitudes will the greenhouse effect from them also be increased as they reach lower temperatures. This positive feedback can also be seen when the cloud cover increases(Liou, 2002). Both the horizontal extend and the vertical structure of the cirrus clouds is important for the clouds effect on the radiational balance(Liou, 1986). All this leads to one fact. The microphysics of the cirrus clouds needs to be well enough understood to make the most effective cloud schemes for use in GCMs. These improved schemes will then improve some of the uncertainties in these models.

2.2.2 Remote sensing of cirrus clouds by satellites

Using satellites for meteorological purposes

Satellites have been used for meteorological purposes since the early 60's when the first satellites where launched(Lynch et al., 2002). They have proved to be a good measure to receive global information about clouds, because they can cover great areas of the earth. Information from large spatial and temporal scales can be collected with satellites(Lynch et al., 2002). Remote sensing instruments on satellites can give a global view of the current weather situation, and thereby connect the cloud patterns with the disturbances in the atmosphere. Ideally when making any global classification one should obtain information at all times and at all locations, but this is an impossible task. One should rather

depend on collecting information from different types of satellites to get the full view of the atmosphere. The two main types of satellites used for meteorological purposes are the geostationary and the polar-orbiting satellites. The first type follows the earth's rotation and will therefore follow one location for a long period of time. The limitations of this type of satellite are the portion of the earth that can be viewed and the specific viewing zenith angle of the satellite(Lynch et al., 2002). The geostationary satellites are not capable of viewing the Polar Regions as their view is limited by the shape of the earth(Lynch et al., 2002). The polar-orbiting satellites follow paths that take them around the earth, and they cover most of the earth during their total orbiting cycle. The total cycle is quite long, but the satellite can make several orbits around the earth during one day(Lynch et al., 2002). The equator areas are least covered and the polar areas are best covered from the polar orbiting satellite. The CALIPSO satellite, from which data is used in this thesis, is a polar orbiting satellite. The calculations will be less dependent on the limitations of the individual satellite by using information from both geostationary and sun synchronous satellites.

There are several ongoing missions with goals to increase the knowledge of the different components of the atmosphere and thereby also knowledge of the climate. These missions can involve single satellites or several, and one way to get as much information as possible is to make several satellites fly in formation. The number of data that is available for analysis and comparison will then be increased. The data from the various instruments on the different satellites may also be compared for practically the same place and time. The A-train constellation is a formation of six satellites, Aqua, CloudSat, CALIPSO, PARASOL, Aura and OCO(will be launched in December 2008 (Orbital, 2007)) with several different instruments for atmospheric measurement. They follow the same path and the last satellite lags the first with approximately 15 minutes. This will give data with an extensive view of the atmosphere and its components. The CALIPSO satellite in this formation has been used to find some of the results in this thesis. The main instrument on this satellite is a LIDAR, and CALIPSO is the first satellite that carries this instrument for a longer period of time[4].

Retrieving cirrus information from satellites

Cirrus cloud information can be difficult to obtain from satellites. Their semitransparent nature is one problem. It can also be difficult to discriminate between cirrus and other clouds, or even between cirrus and other background information(Lynch et al., 2002). These problems can make it difficult to positively identify cirrus from IR and visible images. Cirrus clouds can be seen as some of the whitest areas in IR-images from satellites(Liou, 1986). The coldest objects will appear as the brightest in these IR-images. The cirrus clouds are, as discussed earlier, very high and therefore also very cold clouds. These images are best to use when viewing large and substantial cirrus clouds in connection to the current weather situation. Spaceborne LIDARs can be a better alternative when investigating just cirrus clouds. The CALIOP instrument onboard the CALIPSO satellite is one example. A spaceborne LIDAR can be used to measure the same properties as the ground based Lidars, and the data can be used in much of the same ways. One major difference between the two types of LIDARs is that the spaceborne Lidars are pointed down toward the earth.

[4]The CALIPSO LIDAR is based on experiences from the earlier and shorter LITE experiment (Winker et al., 2003)

Reflection from the ground will therefore also be detected. The spacebourne Lidars are an important contribution to the remote sensing of cirrus clouds. These instruments detect all types of cirrus, even the sub-visual cirrus clouds that go undetetected by IR-measurements. Thick clouds may pose a problem when using LIDARs, as this can cause the lidar beam to become completely attenuated. Several extensive studies of cirrus clouds by spaceborne Lidars are needed to get a proper global cirrus climatology(Lynch et al., 2002). This proper cirrus climatology is needed to better understand how the cirrus interacts with the rest of the atmosphere. Especially important is their interaction with solar and thermal infrared radiation.

2.3 Cirrus clouds on the microphysical scale

The microphysical composition of cirrus clouds will, as mentioned earlier, influence how the cloud interacts with the solar and terrestrial radiation. Either in situ measurements, as flight campaigns and balloon measurements, or remote sensing measurement, as LIDAR or RADAR, are needed to extract information about the microphysical parameters of the clouds.

2.3.1 Ice crystals in cirrus clouds

Ice crystals appear in several different shapes and sizes. They can have clean geometrical shapes as hexagonal plates and columns, more complex geometrical shapes as bullet rosettes and dendrites, or non-geometrical shapes as graupel. The last shape appears mostly for older ice crystals which have partly melted. The formation of the different ice crystal shapes is controlled by the way the water freezes in a crystal lattice. This basic crystal structure is hexagonal and most (pristine) ice crystals have therefore some sort of hexagonal structure too. As the ice crystal grows, local differences in the atmospheric surrounding (i.e. water vapour concentration) will make the different parts of the crystal grow at different rates(Lynch et al., 2002). Especially sharp edges and points will grow more easily. This effect can also change the ice crystal shape when atmospheric surrounding changes(Mason, 1994). Older ice crystals will in addition become more complex by two other means. Firstly, aggregation may add to the complexity as ice crystals merge together or even break apart while still growing(Rogers and Yau, 1989). Secondly, melting and riming will change the structure of the ice crystals. All these processes lead to the almost unlimited number of ice crystal shapes. Some of the possible ice crystals shapes can be found in figure 2.5. Both simple shapes, as the hexagonal plate and simple needles, and more complex shapes as the bullet rosette and dendrites can be seen in this figure.

There have been several different hypotheses about how the different shapes of ice crystals appear and which of them are the most common. Early investigation of ice crystals in clouds reported mostly pristine forms of crystals as the column, plate and dendrite, probably because these types are the ones that are easiest to classify. Later studies found that middle-aged clouds has an abundance of more complex shapes of ice crystals, with the bullet rosette, and its different types, as an important contribution((Korolev et al., 1999),(Bailey and Hallett, 2002)). It is usually believed that cirrus clouds consist of mainly columns, plates and bullets(Liou, 1986). How and under which conditions the different types of ice crystals grow, has not been easily answered. Some studies have investigated how temperature and vapour pressure affected the ice crystal growth(Mason, 1994). But

Figure 2.5: A variety of different shapes of ice crystals. Source: snowcrystals.com

also the effect of different kinds of aerosols as freezing nuclei has been investigated(Bailey and Hallett, 2002). The studies of temperature vs. ice crystal shapes have often lead to the following vertical structure of the ice crystals within the cirrus cloud: Columns and polycrystals dominate the upper regions of cirrus clouds as these occur at the lowest temperature((Noel et al., 2002),(Noel et al., 2004),(Mason, 1994),(Noel et al., 2006)). The percentage of planar ice crystals has been highest in the lower warmer regions of the cloud and decreases with increasing height and decreasing temperature in these studies. But other studies, as the one described in Heymsfield and Platt (1984) has found mostly planar crystals in form of hollow or solid columns and hexagonal plates at the top of the cloud. The previously mentioned studies have focused on mid-latitude and tropical cirrus clouds. Since the clouds above ALOMAR mostly are arctic clouds may these show some differences from the tropical and midlatitude cirrus clouds.

The largest particles will normally dominate at the cloud base in ice clouds, because the heavier ice crystals will tend to fall. The small particles will dominate for nonprecipitating water clouds on the other hand, as they rise and grow with updrafts within the cloud(Platt

et al., 1994). When the ice crystal reaches the base or edge of the cloud they will begin to sublimate as the humidity is reduced due to mixing with the dryer air outside the cloud boundary(Whiteway et al., 2004). The shapes of the ice crystals will then generally become rounder which lowers their depolarization ratio so that columns and polycrystals may be mistaken as platelike crystals(Noel et al., 2006). The sublimation of the ice crystals will also cause a cooling of the air. The result of this cooling can be turbulence and downdrafts due to unstable buoyant forces(Whiteway et al., 2004).

Ice Crystal formation

Ice crystal formation in cirrus clouds have generally been found, from field experiments, to occur at the top of the cirrus clouds(Whiteway et al., 2004). Ice crystals can be formed by two types of phase transitions(Rogers and Yau, 1989). Water molecules can condense into a water droplet before this droplet freezes to an ice crystal, or the crystal can form by directly going from the vapour phase to the solid phase as an ice crystal. How the phase transition occurs also depend on nucleation processes and ice crystals in clouds can form either by homogeneous or heterogeneous nucleation. The homogeneous nucleation occurs when the water molecules are arranged in an ice like pattern by statistical fluctuations. Homogeneous nucleation is theoretically possible for both ice crystal formation from both the liquid and the vapour phase. But this type will occur less often in the atmosphere because of the extreme supersaturation with respect to water that is needed for homogenous nucleation from the vapour phase(Rogers and Yau, 1989). Homogenous nucleation from the liquid phase on the other hand are likely to occur for temperatures below $-40°$. This type of nucleation is controlled by temperature, because the temperature controls the size of the particles that can be formed by chance aggregations. The temperature threshold for ice crystal formation depends on the size of the ice crystal that forms. Wallace and Hobbs (1977) states that some ice crystals with radius around 20 -60 μm have been found to nucleate at approximately $-36°$ and ice crystals just a few micrometers in radius at $-39°$. The temperature threshold for homogeneous nucleation is therefore not an absolute limit, but rather an approximation to where homogeneous nucleation could have occurred.

Heterogeneous nucleation occurs when a foreign particle or substrate causes ice crystals to be formed(Rogers and Yau, 1989). The several different ways heterogeneous nucleation can occur are shown in figure 2.6. The first possible form of heterogeneous nucleation is the heterogeneous deposition. The water molecules will then freeze upon the freezing nuclei by direct deposition without going through condensation to water droplet first. The second form in the figure goes through condensation to water droplet before it freezes it to an ice crystal. The third form freezes a supercooled water droplet by direct contact, and the last possible way for homogeneous nucleation is for an ice nucleus that freezes the droplet after it has been immersed in the droplet(Rogers and Yau, 1989).

Only a few aerosol types can serve as ice nuclei. The best aerosols for ice nucleation are the ones that are not easily dissolved in water and that have a molecular structure that closely resembles ice (Bailey and Hallett, 2002). The water molecules that stick to the aerosol surface will also align themselves in an ice like structure when the structure of the aerosol is close to the structure of ice, and the water will form an ice crystal. Some types of aerosols that are easily found used as ice nuclei in the atmosphere are clay type aerosols as kaolinite and organic aerosols as small remnants of plants or plankton.

2.3.2 Microphysical properties of cirrus clouds

The microphysical properties of cirrus clouds are of vital importance for their effect on radiation. The size and shape of the ice crystals influence how the light is scattered through the cloud. How the different ice crystal shapes are distributed through the cloud can also effect how the clouds interact with radiation(Lynch et al., 2002). Other microphysical properties as ice water content and size distribution in the clouds can also be interesting to look at.

Depolarization

Ice crystals are complex structures with many planes of refraction. Light scattered by ice crystals will therefore likely have a change in polarization. Early work with the linearly polarized Lidars(Schotland et al., 1971) showed that Lidars could be used to distinguish between ice and water clouds because of this effect. The laser light emitted from a lidar system is linearly polarized. Some of the light will be perpendicularly polarized with respect to the transmitted light because of the depolarization effect when the light is received by the telescope . The ratio between these two polarizations of the light is called the depolarization ratio and can for example be used to find information about the shape of the ice crystals.

The ice crystal depolarization is not the only cause of depolarization, and to extract correct information about the ice crystal one needs to take the other effects into account. The molecules in a pure atmosphere will also cause some depolarization (Young, 1982)

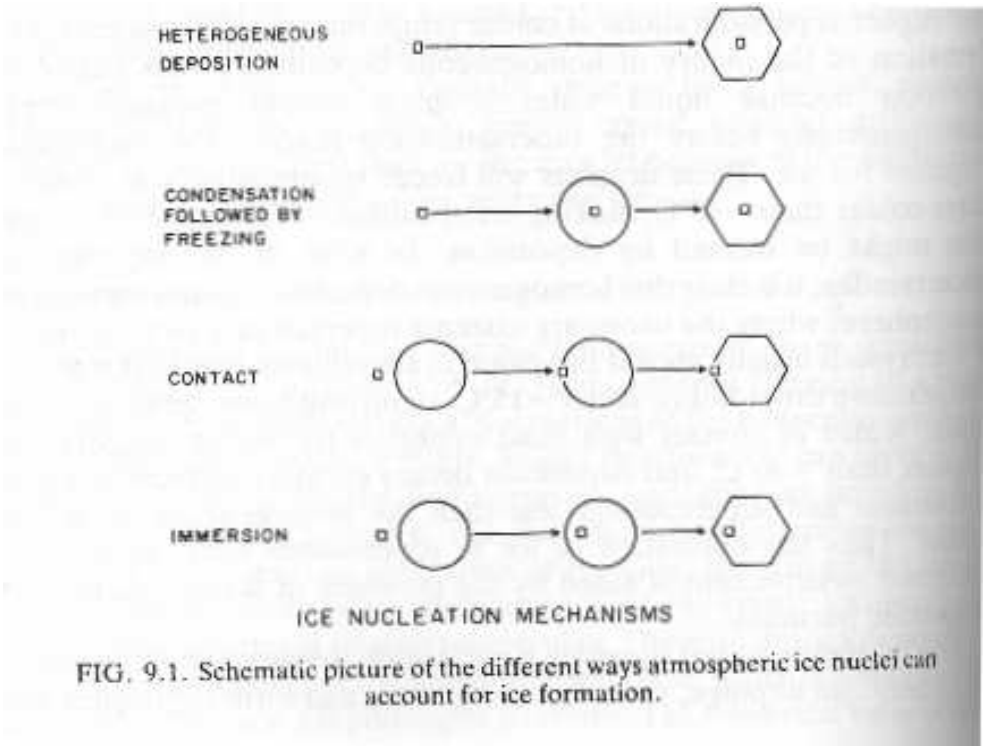

FIG. 9.1. Schematic picture of the different ways atmospheric ice nuclei can account for ice formation.

Figure 2.6: Different types of heterogeneous nucleation. Source: chapter 9 in Rogers and Yau (1989)

and an estimation of this depolarization from the Cabannes line is 0.37%. The Cabannes line is the central line in the spectrum of the scattered light, which together with some rotational side bands gives the total Rayleigh scattering of air molecules(Young, 1982). The depolarization ratio of 0.37% comes from the following depolarization equation for the Cabannes line when the light is vertically polarized:

$$\rho_O^c = \frac{3\epsilon}{180 + 4\epsilon} \tag{2.1}$$

$$\epsilon = 0.22 \tag{2.2}$$

$$\rightarrow \rho_v^c = 0.365\% \tag{2.3}$$

This equation is from Table 1 in Young (1982)[5]. The variable ϵ is a measure of the anisotropy in a molecules polarizability and an effective value of ϵ for air if 0.22. The effect of molecular depolarization must be included in the equations of the depolarization ratio to avoid biased results. Another source for depolarization is water droplets. The spherical nature of the liquid droplets does not lead to polarization during single scattering events, but multiple scattering and asymmetrical raindrops[6] may cause some change in the polarization. Spherical water droplets will ideally give a depolarization ratio value at 0, but multiple scattering will cause the depolarization ratio to increase. One way to identify bias from multiple scattering is to look at the optical depth. High optical depths will increase the multiple scattering effect, especially in the higher parts of the cloud and should be avoided(Noel et al., 2002). Another way of eliminating the possibility of water droplets is to look at the cloud layer temperature. From section 2.3.1, the cloud layer temperature must be below approximately $-40°C$ to avoid any liquid water. However, the possibility for liquid water decreases exponentially as the temperature drops below 0°, so this is not an absolute limit. Another effect that can change the polarization is riming or partially melting of the ice crystals(Sassen, 1991). The riming or melting will increase the depolarization ratio, since the complexity of the surface will grow with the changes on the crystal. Older ice clouds, for which melting and riming would have had time to be more effective, will therefore exhibit larger depolarization ratios than a younger cloud, which consist of more pristine ice crystals.

An effect that can give a small depolarization ratio values is when a large group of pristine ice crystals is uniformly oriented(Sassen, 1991). This effect may cause misinterpretations of the depolarization ratio. A layer in a cloud that displays a depolarization at 0, would normally be understood as a layer of water droplets, but could also indicate horizontally oriented crystals, either plates or columns. This value arises because the light is directly reflected off the bottom surface of the crystal without any depolarization, as can be seen in figure 2.7. This figure shows that the light beams that hit the ice crystals will remain parallel polarized after it is reflected of the bottom surface of the ice crystal. Any horizontally oriented ice crystals will also affect the solar radiation transfer in the clouds, as the general radiative transfer equation no longer is valid in this case(Liou, 1986). How often horizontal orientation of the ice crystals occur will therefore also affect the radiational balance. (Noel et al., 2004) stated that horizontally oriented ice crystals where

[5] ρ is the depolarization, subscript O signifies unpolarized light, subscript v signifies vertically polarized light and superscript c signifies the Cabannes line.

[6] Large water droplets loose their spherical from as they fall due to air resistance (Rogers and Yau, 1989)

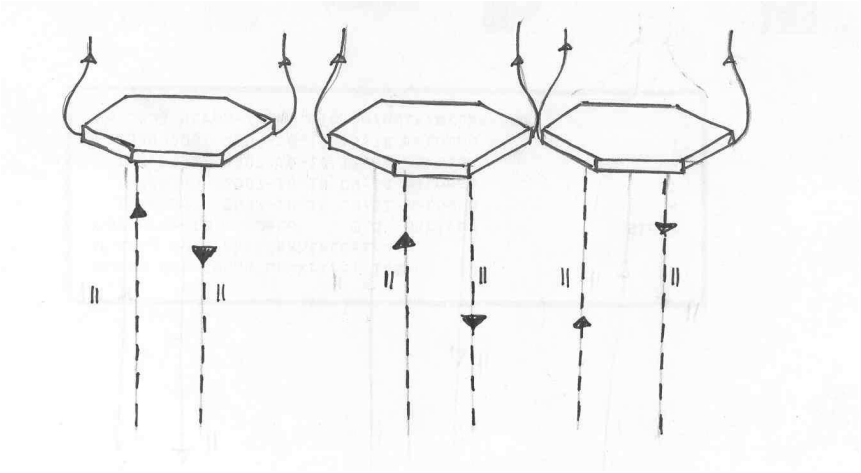

Figure 2.7: Horizontally oriented ice crystals does not change the polarisation of the laser light

commonly found both midlatitude and high-latitude cirrus clouds. One option to find a better depolarization ratio in cases with possible horizontal orientation is to regularly tilt the lidar some degrees off its regular axis. This tilting has not been made in the cases used in this thesis. A possible horizontal orientation can be identified by looking at the intensity of the backscattered signal if no tilt has been made, or for systems where this tilt is not possible. Horizontally oriented particles will be more likely than water molecules if the area with 0 depolarization ratio also has an exceptionally high backscattered intensity. The orientation of the ice crystals depend on the flow pattern around them as they fall. Brownian effects will tend to randomize the orientation of the of the smallest ice crystals, $> 10\mu m$ (Lynch et al., 2002). The air flows will dominate over the Brownian effects for the larger particles. Both these flows and local electric fields may cause the particles to be horizontally oriented. The critical parameter is the Reynolds number of the flow when the flow pattern around the ice crystals decides their orientation. If the Reynolds number is between 1-5 the particles will fall randomly(Lynch et al., 2002). Small eddies will form in the rear flow of the crystal ff the particles are larger and the Reynolds number of the flow around them reaches 20-200. These eddies tend to stabilize the crystal end keep it in the horizontal orientation. These eddies will not follow that close to the crystal anymore when the crystals get bigger, and the Reynolds number is above 200. This will cause the orientation of the crystal to fluctuate. Figure 2.8 shows these three types of falling for plates and columns. The identification of ice crystal shapes from depolarization ratio is a difficult task, and the previously mentioned effects complicate the identification. The connection between the depolarization ratio and the shape, or more precisely the shape ratio $Q = \frac{l}{2r}$ where l is the crystal length and r the base radius, has been confirmed and analysed through simulations with ray-tracing code (Noel et al., 2001). A later article by the same author (Noel et al., 2004) defines the shape classification displayed in table 2.3 which is used in this thesis. The important points from this table are the limit depolarization values of 0.25 and 0.5 between the different crystal shape categories.

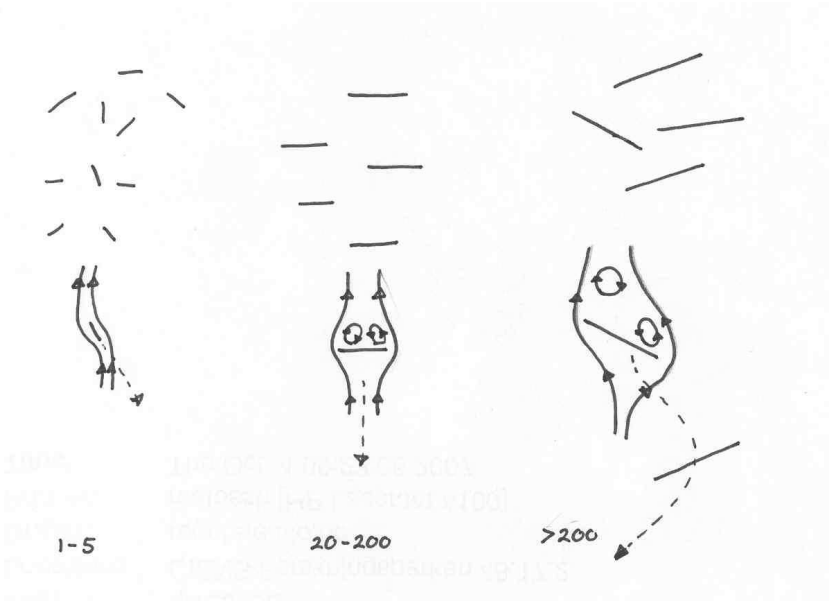

Figure 2.8: Fall patterns of plates/columns under different terminal fall speed Reynolds numbers. The smallest ice crystals, with Reynolds numbers from 1-5 will fall randomly. Ice crystals with Reynolds numbers from 20 to 200 will fall horizontally and large ice crystals with Reynolds numbers above 200 will fall randomly. Adopted and slightly modified from figure 3.8 in Lynch et al. (2002)

Crystal shape	Depolarization ratio	Shape ratio
Thin plate like crystals	$\delta < 0.25$	$Q < 0.1$
Irregular/intermediate crystals	$0.25 < \delta < 0.5$	$0.1 < Q < 1.5$
Columnar crystals	$\delta > 0.5$	$Q > 1.5$

Table 2.3: Classification of ice crystal shapes through depolarization ratio

Category	τ range	Description
Subvisual	<0.03	Invisible against the blue sky
Thin	0.03-0.3	Translucent, retains a bluish colour
Opaque	0.3-3.0	Usually appears white
Altostratus	>3.0	Disk of sun becomes indistinct

Table 2.4: Cirrus cloud categories and approximate optical depths based on cloud transparency and colour(table 2.1 in Lynch et al. (2002)). These limits are found with the 0.694 μm wavelength.

Optical depth and subvisible cirrus

The optical depth is a variable that describes how much light that is attenuated by an atmospheric feature as a cloud or an aerosol layer. Optical depth is an important factor to extract, as this variable is needed to solve the general radiation transfer equations(Liou, 1986). The following criteria must be met to measure whether a cloud is subvisual or not: the optical depth in the visible(0.649 μm) must be below 0.03 for the cloud to be classified as subvisual(Lynch et al., 2002). The optical depth is also a way of identifying cirrus clouds from other cloud types. Table 2.4 from chapter 2.3 in Lynch et al. (2002) shows a distinction between tree types of cirrus clouds and the boundary value for distinction between cirrus and altostratus clouds.

Cirrus clouds are in this table divided into three categories depending on their visibility: subvisible, thin and opaque. The subvisible cirrus cloud can not be seen with the naked eye, the thin cirrus is visible, but translucent and the opaque cirrus is clearly visible and usually white. Table 2.4 shows these three categories and the range of the optical depth associated with each category. The forth category in the table is the altostratus cloud. The cirrus clouds will turn into this type of cloud if they grow thick and the optical depth reaches 3.0. The optical depth limit for subvisible cirrus clouds are 0.03. The SVC[7] clouds seems to be colder (-50 -90°) and to consist of smaller particles around $< 50\mu$m in diameter, in addition to being thinner than other cirrus clouds. There have also been some indications that at these subvisible cirrus clouds can be connected to high pressure systems(Liou, 1986). Visually the SVCs can be detected only to a limited extend. Optical phenomena around the sun or moon that is generated by small particles may be a sign of subvisible cirrus. This challenge in the detection of the subvisible cirrus clouds come from the radiative properties of ice. The main interaction between ice crystals in the atmosphere and radiation in the visible part of the spectra is scattering. The optically thin SVCs do not scatter the visible part of the light spectre efficiently enough to be detected. This optical effect will also explain why passive remote sensing tools do not detect SVCs. These subvisible clouds will be detected more easily with LIDARs, because they scatter the LIDAR wavelengths more efficiently than the visible wavelengths.

2.3.3 In situ measurement of cirrus clouds

In situ measurements of cirrus clouds are made by flight campaigns or balloon measurements depending on the information needed. Flight campaigns are needed for most

[7]SubVisible Cirrus

Figure 2.9: Digital images of the ice crystals observed by the SPEC Cloud Particle Imager(CPI). All particles are less than 0.5 mm in length. Source(text and image): http://www.specinc.com/

microphysical purposes, as information about ice crystal size and shape, and radiosondes are used to find information about variables as temperature and humidity. These types of measurements are needed in the search of a good description of the cirrus cloud microphysics. Connected insitu and LIDAR measurements are needed to check the connections between the LIDAR data and actual microphysical properties. In this thesis are insitu measurements not an important part since neither flight campaigns nor radiosonde measurements where made in connections to the lidar measurements used.

The airplanes in flight campaigns are equipped with several different instruments for detecting the atmospheric properties within the cloud. A relatively new instrument that uses advanced imaging techniques is the CPI. A CPI or Cloud Particle Imager is an instrument that can be used to find the microphysical properties of the cloud. Campaigns that have used this instrument include the Emerald airborne campaigns in Australia (Whiteway et al., 2004) and the FIRE ACE campaigns in the Arctic (Lawson et al., 2001). A CPI was used together with an airborne LIDAR during the ASTAR experiment (Arctic Study of Aerosols, Clouds and Radiation) described in Gayet et al. (2007). This case study encountered ice crystals precipitating from a cirrus cloud above the flight path. From the CPI data was the ice crystals found to be mostly irregular, and the LIDAR data showed depolarization ratios up to approximately 50% in the area where these ice crystals resided. These results are similar to what have been found in other studies((Bailey and Hallett, 2002),(Noel et al., 2002)). The CPI measures the particle size, shape and concentration in

addition to making high definition digital images of the ice crystals. It can also be used to discriminate between spherical water droplets and nonspherical ice crystals(Lawson et al., 2001). Figure 2.9 shows images from a SPEC CPI. This image shows some of the different types of ice crystals that can occur. Both regular shapes as the columns, and more complex shapes as the bullet rosette in the upper right corner or the column capped with sectored plates in the lower left corner can be seen in this image. SPEC[8] is a company that specializes in aircraft instrumentation to be used in cloud physics(SPEC, 2008). An older technique to find the ice particle content in a cloud is to use a movie film covered in a solution of Formvar[9] and ethylene dichloride(Wallace and Hobbs, 1977). This film is then exposed out in the cloud air so that ice particles can get trapped in the solution. When the ice and the ethylene dichloride have evaporated will just the plastic shell that covered the ice crystal remain on the film and these can then be counted(Wallace and Hobbs, 1977). These are not the only instruments and techniques for in situ measurement of microphysical properties. A more extensive description of possible in situ measurements should be sought other places as in situ measurements have no part further in this thesis.

The instruments that detect the cloud microphysical properties are used together with other instruments to connect these data with the atmospheric conditions. These other instruments include instruments measuring properties like temperature, relative humidity or liquid water content. These in situ measurements are of great importance to get the best possible results from the cloud measurements with Lidars. The in situ measurements then serve as validation points for the algorithms used to find the microphysical properties from the lidar data. The in situ measurements by flight campaigns are therefore more useful as a validation source than for making any global statistics. The cost of flight campaigns is too high to make global statistics. The area coverage by the planes can additionally be quite low and the uncertainties in these types of measurements can be large(Zhang and Mace, 2006). Balloon measurements are more easily made, but only cover one location. They will also follow the wind and therefore not necessarily encounter any of the interesting clouds.

2.4 Cirrus clouds on the Mesoscale

Cirrus clouds are connected to larger synoptic features. Their formation is also linked to these features. This section describes their formation mechanisms and the instruments that can investigate cirrus clouds on the Mesoscale.

2.4.1 The formation of cirrus clouds

The formation mechanisms of cirrus clouds can be divided into five categories, where four are natural and one is anthropogenic(Lynch et al., 2002). These five different categories and their formation mechanisms can be seen in table 2.5 from Lynch et al. (2002)

The first possibility of formation and development of the cirrus clouds is therefore Mesoscale (or synoptic) motions and features. Layer clouds, as the stratus and cirrus clouds, are formed by forced lifting of stable air(Wallace and Hobbs, 1977). An example of this process is the cloud formations that appear when a warm front approaches. For the warm front, warm air from the warm sector of the front will rise slowly above the

[8]Stratton Park Engineering Company INC

[9]Formvar is a form of plastic

Category	Mechanism
Synoptic (jet stream, frontal, etc)	Top-down generation
Injection cirrus	Thunderstorm anvil
Mountain-wave updraft	Orographic, terrain-induced
Cold trap	Tropopause-topped thin layer
Contrail-cirrus	Rapid cooling of aircraft exhausts

Table 2.5: Breakdown of cirrus clouds by generating mechanism, table 2.2 from Lynch et al. (2002)

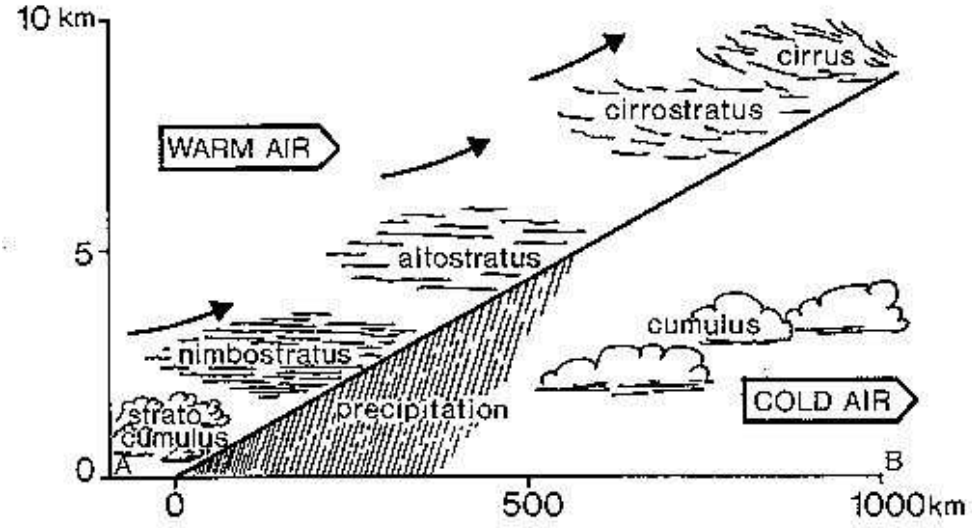

Figure 2.10: Cloud features following a warm front. Source: http://freedom-in-the-air.com/_oneclick_uploads/2007/05/warm-front.jpg

colder air and this will lead to the formation of clouds. The first clouds will be very high cirrus clouds that gradually spread across the sky. As the front moves closer, cirrostratus clouds will appear. They might be very thin, mostly subvisible or only seen as a very thin veil across the sky. Stratus types of clouds will form later, followed by more extensive, denser and precipitating clouds as seen in figure 2.10. Cirrus clouds, especially very high cirrus clouds may therefore be an indication of bad weather to come. The height of the clouds will decrease as the front moves closer(Wallace and Hobbs, 1977). The previously mentioned figure displays a model of the warm front as given by the classical Norwegian model defined by Vilhelm Bjerknes and the other participants of the Bergen School.

But cirrus clouds can also be formed as the last stage of a cumulunimbus cloud. This formation type is the injection category of cirrus formation in table 2.5. During this stage the anvil of the cumulunimbus cloud will become glaciated and spread out horizontally as it reaches the tropopause(Wallace and Hobbs, 1977). The updraft in which ice formation occurs is relatively strong, up to a few meters per second, resulting from the strong updrafts that feed the thunderstorm. This high updraft will tend to increase ice particle concentration in the cloud(Lynch et al., 2002). The remnants of the glaciated anvil are called anvil cirrus. This anvil cirrus may remain some time after the rest of the cumu-

lunimbus cloud has dispersed. The orographic cirrus formed by mountains is also formed by strong updrafts resulting from air that is pressed up mountain sides (Lynch et al., 2002). The only anthropogenic source of cirrus cloud is formed in the exhaust of airplanes. This exhaust consists of plenty of moisture and condensation nuclei. These rapidly forms condensation trails, often consisting of a high amount of small ice crystals(Lynch et al., 2002). The last form of cirrus clouds, the cirrocumulus cloud, begins its development as a cirrostratus layer. Cirrocumulus clouds are then formed from this layer by movements that break the cloud layer up into small cumulus shaped elements. These movements are caused by heating of the cloud bases from ground heat radiation and cooling at the cloud tops as the clouds radiates back into space. These effects cause small convective cells to form inside the cloud layer, and these break the layer into smaller features(Wallace and Hobbs, 1977). The last natural category in table 2.5 is the cold trap cirrus. These are thin to subvisible cirrus clouds that form in the tropics at very high altitudes (15-20 km) and very low temperatures ($-70°$ to $-90°$). These clouds are only formed in the tropics and will therefore be of no importance for the ALOMAR data (Lynch et al., 2002). As seen from this section, the main formation mechanisms of cirrus clouds are synoptic scale disturbances as an approaching warm front. These clouds can also be formed as secondary features of other clouds or because of orographic features. Liou (1986) states that cirrus and cirrostratus probably are associated with high pressure systems or upper level troughs. Cirrus unicus are related to either Mesoscale or larger-scale synoptic disturbances. The vertical and horizontal extent of the clouds is some of the interesting cloud features to be found on this scale. The vertical profiles of the cirrus clouds can be found with a LIDAR. This instrument can also find the boundary heights of the cirrus clouds quite accurately. Precise base heights are especially difficult to obtain with other means than active remote sensing tools(Liou, 1986)

2.4.2 Remote sensing of cirrus clouds by LIDAR/RADAR

The LIDAR and the RADAR are two remote sensing tools that are especially well suited for detecting atmospheric features as clouds, aerosols and precipitation. They are both build on many of the same principles in scattering and geometric optics. Molecules and particles scatter radiation in the atmosphere, and how the radiation is scattered depends on the type of radiation and the type of scatterer. There are two different scattering regimes for spherical scatterers depending on the relationship between the size of the particle and the wavelength of the radiation. Rayleigh scattering occur when the size of the particle is much smaller that the wavelength of the incident radiation. Air molecules scatter light in this way, and thereby explain why the sky is blue(Liou, 2002). When the size of the particle is comparable or larger than the wavelength of the radiation will the light be scattered by Lorentz-Mie scattering. This type of scattering is more complex than the Rayleigh scattering.[10]

Usually, when detecting cloud and precipitation particles, basic geometric optics are used where one assumes that the particles are much larger than the incident wavelength. The light beams can then be localized as geometrical rays(Liou, 2002). This means that the smallest objects that can be detected by the methods using these principles are of sizes similar to the wavelength of the radiation.

[10]more about scattering in the atmosphere can be found in appendix B

Conventional meteorological Radars[11] are useful for detecting precipitation sized particles as they operate on cm-wavelengths in the electromagnetic spectre. But this means that the smaller particles, and therefore non-precipitating clouds as cirrus, go undetected by these types of RADARs. To detect smaller particles one can use Radars that operates on mm-wavelengths instead. These have proved especially useful when measuring the liquid or ice water content of clouds, and are valuable additions to LIDAR measurements of clouds(Lynch et al., 2002). The Lidar[12] can detect smaller particles than the RADAR because it operates on shorter wavelengths. This smaller wavelength makes the lidar a valuable tool for detecting aerosols, but also for detecting the small ice crystals in cirrus clouds. Another advantage with the LIDAR in connection to cirrus clouds is the possibility to detect the polarization of the light that returns. This polarization gives information about the phase of the scattering object and a more extensive description of this can be found in section 2.3.2. The LIDAR is therefore the most useful remote sensing tool when investigating ice clouds. The Lidar gives information as vertical profiles of the atmosphere and the clouds. The vertical structure of the different cloud parameters can therefore be found from the LIDAR data. To extract these types of information one first has to look at the lidar equation.

The lidar equation

In the basis for all work with this instrument lies the LIDAR-equation. This equation gives the power received by the detector as a function of the qualities of the instrument, the light attenuation by the atmosphere and the interaction between the light and the target medium, as well as the range to the target medium and the wavelength of the light(Matthey, 2000). There are two basic parameters in this equation; the extinction coefficient and the backscatter coefficient. These two parameters arise from the interaction between the beam and the atmospheric constituents. When the light interacts with any particle or molecule in the atmosphere the light can either return to the detector by backscattering, or not return by either being absorbed by the particle or scattered away from the detector. The extinction is therefore the light that is absorbed or scattered away by the atmosphere and the backscatter coefficient is the ratio between the backscattered light and the beam intensities(Frioud, 2003). The LIDAR equation for the received power of the signal is given as follows:

$$P(r,\lambda) = E_0 K \eta(\lambda) O(r) \frac{A}{r^2} \frac{c}{2} \beta(r,\lambda) exp\left(-2\int_0^r \alpha(r',\lambda)dr'\right) \tag{2.4}$$

It is often better to use the energy instead of the power, since the time of each pulse made by the laser is known. The energy received can be found by noting that $E = P * \tau$, where τ is the integration period(single pulse integration time)(Frioud, 2003):

$$E(r,\lambda) = E_0 K \eta(\lambda) O(r) \frac{A}{r^2} \frac{c\tau}{2} \beta(r,\lambda) exp\left(-2\int_0^r \alpha(r',\lambda)dr'\right) \tag{2.5}$$

The following are the different constants and variables in this equation:
Received variables and physical factors

[11]Radio Detection And Ranging
[12]Light Detection And Ranging

- P: Received power
- E: Received energy
- c: The light speed: $8.0 * 10^3 \frac{m}{s}$

Instrument dependent factors

- E_0: The energy pulse emitted from the laser
- P_t: Transmitted power from the laser
- λ: wavelength
- A: effective area of the receiver lens or telescope
- S: Instrument factor. This factor depends on the efficiencies of the transmitter and the receiver and takes into account the overlap function. This variable can also be rewritten as follows:

$$S = K\eta(\lambda)O(r) \tag{2.6}$$

  Where:

  - K: the optical efficiency of the lidar transmitter and receiver sub-systems expressed as a constant.
  - $\eta(\lambda)$: The quantum efficiency of the detector, which is wavelength dependent.
  - *O(r)*: Overlap function, which gives how much of the laser irradiation area which is inside the receiver's field-of-view. This function depends on the setup of the LIDAR.

Atmosphere and particle dependent factors

- α: Extinction coefficient
- β_v: Volume backscattering coefficient
- r: Range, height, distance from the instrument

The extinction coefficient and the backscattering coefficient are the two variables one wishes to extract from the received energy. All other information from the scattering by the atmospheric constituents can be calculated from these two variables.

Acquisition modes

Lidars have two different acquisition modes, the photon-counting and the analogue mode. The single currents from single photons can be counted if the signal received is weak enough. This mode is the photon counting mode. The noise is easier to extract in this mode because the noise pulses are much smaller than the actual signal pulses, and the noise can therefore be removed by threshold considerations(Frioud, 2003). The photons will arrive so close that it is impossible to discriminate one from the other when the signal is strong. Then it is better to measure the total current. This mode is called the Analog mode of acquisition.

Noise type	Ph.-count.	Analog
Noise in signal(quantum, photon noise)	x	x
Background ambient noise	x	x
Photoelectron noise	x	x
Dark (-current) noise	x	x
Gain noise		x
Thermal (Johnson) noise		x

Table 2.6: Type of noise encountered in lidar measurement depending on the detection mode

But, as will be shown in the noise section, this mode is more vulnerable to noise. The Analog mode will be easiest to use in the lower part of the atmosphere. This is because in this part will more of the laser beam be scattered back to the receiver. For the higher part of the atmosphere, the photon counting mode will be the best, because less light is scattered back from this area.

Noise and overlap problems with the LIDAR

Both overlap between the light beam and the telescope field of view and noise are issues that weaken the signal accuracy(Frioud, 2003). These effects need to be accounted for to extract meaningful information from the received signal. The overlap between the light beam and the telescopic field of view is not complete until some distance from the LIDAR. These two cones will not overlap at all at a closer distance from the LIDAR, and this lowest part of the atmosphere will therefore go completely undetected. This geometrical property gives an unwanted range dependency in the effective Lidar signal P(r). The Range Corrected Signal is calculated by multiplying the Lidar signal with the square of the range(Frioud, 2003) to remove this range dependency:

$$RCS(r) = P(r) * R^2 \tag{2.7}$$

Even though the backscattered signal falls off with the square of the range, will the background noise remain constant(Platt et al., 1994). There are several different types of noise that will affect the measured signal. These noises need to be accounted for to minimize errors in the measured signal. Some of the noise originates from the background, and some from the instruments and some of the noises depend on the detection mode. It is the fluctuations in each noise type that is problematic. If the noise sources did not fluctuate, they could just be accounted for in constants. A presentation of the noises and how they are connected to the detection mode can be seen in table 2.6 taken from Matthey (2000). From this table it can be seen that the Analog mode has more noise sources and is therefore more vulnerable to noises than the photon counting mode.

The photon or quantum noise in the signal is created when the signal enters the detector and during the conversion of photons to photoelectrons. This type of noise will therefore only exist when the detector receives a signal. The atmospheric background noise is light detected by the receiver which does not originate from the laser, for example sunlight that enters the detector during the day. All undesired optical radiation that enters the system falls in this noise category, both from natural and artificial sources. The dark current noise is caused by the photodetector. When no light is sent upon its surface this component still

produces a current, mostly due to loose electrons from thermal release(Matthey, 2000). This noise is therefore dependent on the temperature of the photodetectors. The thermal noise is due to an extra current in the Analog mode. This current rises from a heating of the current carriers due to the resistance in the photodetectors. These are just some of the noise sources that can affect the lidar, and they need to be removed before an analysis of the lidar signal can be made. The signal to noise ratio is usually given by the following equation:

$$SNR = \frac{S}{\sqrt{\sum_{i=1}^{k} \sigma_k^2}} \tag{2.8}$$

Where S is the signal and σ is the standard deviation for each of the noises k[13]. One wishes to make this signal-to-noise ratio as low as possible to improve the quality of the measured signal. One operation that will improve this ratio is binning. Binning means that an average is made over a predefined number of data points from the measured signal. Together, the overlap effects and the noise effects will degrade the signal quality with increasing height. Several different techniques exist to counteract the noise problems. These include removing noise by subtracting noise measurements from atmospheric measurements or smoothing the signal, i.e. taking the average between some of the closest profiles. The latter one needs to be treated with caution to avoid removal of the interesting features in the lidar profiles.

Retrieving β and α (inversion techniques)

The goal of working with the Lidar is to measure how the energy is backscattered from the atmospheric constituents or how it is attenuated by the atmosphere. The measure of these processes are the backscattering coefficient, β, and the atmospheric extinction, α, which both are found in the Lidar equation. Herein lies the difficulty; to get information of either one, we need information about the other. There is an unknown relation between β and α, and this relation needs to be found or decided before extinction and the backscatter coefficient can be calculated(Frioud, 2003). Two solutions, that are widely used to solve this problem, are the Klett single-component solution and the Fernald two-component solution. Both of these techniques are suitable for elastic backscattering(Frioud, 2003). The Klett single-component solution assumes the following simple relation between the extinction and the backscattering: $\beta(r) = C_1(\alpha(r))_2^C$. Where C_1 and C_2[14] are constants and $\beta(r)$ and $\alpha(r)$ are the range dependent backscattering and extinction coefficient(Frioud, 2003). This solution is based on an assumption that the lidar ratio, that is the ratio between the extinction coefficient and the backscattering coefficient, is a constant through the cloud:

$$LR = \frac{\alpha(r)}{\beta(r)} \tag{2.9}$$

The accurate extinction α can then be found for dense clouds with the Klett method(Lynch et al., 2002). The Fernald solution is more suitable for thinner clouds and finds accurate values for the backscattering β. The extinction coefficient is in this case strongly dependent on the value of C_2(Lynch et al., 2002). The programs used to find the cirrus properties in

[13] k is here just the number of different noises

[14] C_2 is here the backscattering to extinction ratio, $C_2 = \frac{\beta(r)}{\alpha(r)} = \frac{1}{LR}$(Lynch et al., 2002)

this thesis use another approach than the previously mentioned Klett and Fernald inversion techniques. The RCS from the LIDAR is instead fitted to a molecular profile to find the backscattering ratio. This is an approach similar to what is used in Cadet et al. (2005) to find the optical depth and in Platt et al. (1994) to find cloud height. The backscattering ratio can then further be used to find the other parameters. More about how the different variables are retrieved can be found in the next chapter.

Chapter 3

Method

The main data used in this thesis was LIDAR data from the tropospheric LIDAR at ALOMAR. LIDAR data from the CALIOP LIDAR onboard the CALIPSO satellite has been used to compare with the ALOMAR data in some of the cases. Molecular profiles from the MSIS-90 model have been used to normalize the raw lidar signal. Temperature profiles, mostly from radiosondes but also from the MSIS-90 model, have been found to extract information about the cloud temperature and the tropopause. The clouds found in these data have been compared with the weather situation from each case. Weather charts from met.no and IR-satellite images have been used for this purpose. The different sources for data will be further described in this section. The variables retrieved from these data, and how they are retrieved is also described.

3.1 The ALOMAR observatory

The ALOMAR (Arctic Lidar Observatory of Middle Atmosphere Research) observatory belongs to the Andøya Rocket Range, which is governing balloon and sounding rocket operations for scientific use in the Arctic. The Rocket range as been in operation since 1962, and the ALOMAR observatory was finished in 1994 (Alomar, 2006a). Operation of the Tropospheric LIDAR used in this thesis began in 2005. The location of the observatory, as well as the Rocket Range is on Andøya (69°N 16°E) an island by the coast of northern Norway (Frioud et al., 2006b). The location of ALOMAR can be seen in figure 3.1. The ALOMAR facilities are located on top of the Ramnan Mountain 379 m ASL.

Research about the arctic is proving more and more important for understanding the global climate. Because of its location on the edge of the Arctic, both arctic and non-arctic phenomena can be measured at ALOMAR. This is an excellent position for observation of arctic aerosols and clouds, as well as anthropogenic aerosol layers from for example Europe or Asia.

The observatory has, in addition to the Tropospheric LIDAR used in this thesis, LIDARs for studies of Noctilucent Clouds, Ozone profiling, and Sodium Density measurements. These LIDARs focus mainly on higher layers in the atmosphere than what the tropospheric LIDAR does. Additional instruments connected to the ALOMAR observatory include RADARs, a sun photometer (CIMEL) and the possibility for balloon releases from Andøya Rocket Range, to which the observatory is associated. Information about these instruments and the observatory in general can be found on the ALOMAR web pages: alomar.rocketrange.no.

Figure 3.1: Map of northern Europe showing the location of the ALOMAR observatory at Andøya ($69°N$,$16°E$). Source: Google map

3.1.1 The tropospheric LIDAR at ALOMAR

The tropospheric LIDAR at ALOMAR have been in operation since 2005. It is a LIDAR that can detect both Raman and Rayleigh wavelengths. These wavelengths can give information about specific molecules as N_2 and H2O. The latter gives profiles of the scattered intensity from atmospheric particles as aerosol and cloud particles. More about Rayleigh and Raman scattering can be found in appendix B. The principle of a LIDAR is the following(Matthey, 2000): Light pulses are sent into the atmosphere. This light will be scattered by the different atmospheric components it encounters. How the light is scattered will depend on the type of component and on the wavelength of the light emitted from the LIDAR. The LIDAR telescope will receive the backscattered light and send it trough the rest of the LIDAR system. The light signal will be transformed to an electrical signal, and this will be stored as atmospheric profiles. Information from the atmospheric components can then be extracted from these profiles.

Table 3.1 show the specifications for the tropospheric LIDAR system at ALOMAR (Frioud et al., 2006a). The important points from this table are the channels the tropospheric LIDAR operates on, the temporal resolution and the spatial resolution. The tropospheric LIDAR operates on both elastic Rayleigh wavelengths and on Raman wavelengths as can be seen from the table[1]. The elastic channels operates on the wavelengths 1064 nm, 355 nm, 532 nm, and the Raman channel on the wavelength 387 nm. Raman wavelengths are used to detect specific gases in the atmosphere. The 387 nm wavelength is for example used to find H_2O profiles. Additional Raman detection channels operating on the 408nm, 660 nm and 608 nm will be added in the future(Frioud et al., 2006b). The important

[1]Several different types of LIDARs exist. Examples are the Rayleigh, Raman, Doppler and DIAL LIDARs. The different LIDARs are useful for finding different types of information. A short overview can be found in Veerabuthiran (2003a)/Veerabuthiran (2003b).

Characteristic	ALOMAR
Latitude, longitude	69°N, 16°E
Altitude	379 m
Laser type	Nd:YAG
Wavelengths emitted	335, 532, 1064 nm
Wavelengths detected (Rayleigh)	335, 532(∥), 532(⊥), 1064 nm
Wavelengths detected (Raman)	387 nm (408, 607, 660nm)[a]
Pulse energies	120, 290, 610 mJ
Repetition rate	30 Hz
Temporal resolution	70 s
Spatial resolution	7.5 m
Beam full divergence	400-700 μrad

Table 3.1: Specifications of the tropospheric LIDAR, modified from Frioud et al. (2006a)

[a]Raman channels to be added in the future

channel for this thesis is the 532 channel. The polarization of the 532 nm wavelength can be changed by ice crystals in the atmosphere, and the two different polarizations are detected in separate channels: 532(∥)[2]nm and 532(⊥)[3]nm. The information from these channels can then be used to find information about the ice in the atmosphere. The data from these two channels can be used to find the depolarization ratio, which is one of the parameters investigated in this thesis. The temporal and spatial resolution of the LIDAR system can also be found in table 3.1. The temporal resolution: $\Delta t = 70s$, gives the time between each shot made with the lidar, and therefore also the time between each profile. The spatial resolution: $\Delta z = 7.5m$, gives the distance between the bins. For each profile are there a total number of 8192 bins in which signal values are stored. This means that profiles can be made that reaches almost 62 km above the ALOMAR site.

Laser and Harmonics generator

The LIDAR is an active remote sensing tool that has its own radiation source in the laser. The laser emits short pulses of radiation that will be scattered in a specific way for different components in the atmosphere. The backscattered light can then be used to find information about these components. The laser on the tropospheric LIDAR at ALOMAR is an Nd:YAG laser which emits at the 1064 nm wavelength. Nd:YAG corresponds to the crystal used in the laser to acquire optical gain, which is a way to increase the power of the signal. The crystal is a neodymium-doped yttrium aluminium garnet, with the chemical formula Nd:$Y_3Al_5O_{12}$. A doped crystal has a small amount of an impurity, here neodymium (Nd^{3+}), which alters the optical properties of crystal slightly. The optical properties of the crystal can be customized to specific uses when adding such impurities. Some of the 1064 nm light will be transformed into 532 nm light and 355 nm light in the harmonics generator. These wavelengths correspond to the second and third harmonics respectively (Frioud et al., 2006a). The reason for doing this is that light from the two harmonics in addition to the original 1064 light, will give more information about the

[2]parallel
[3]perpendicular

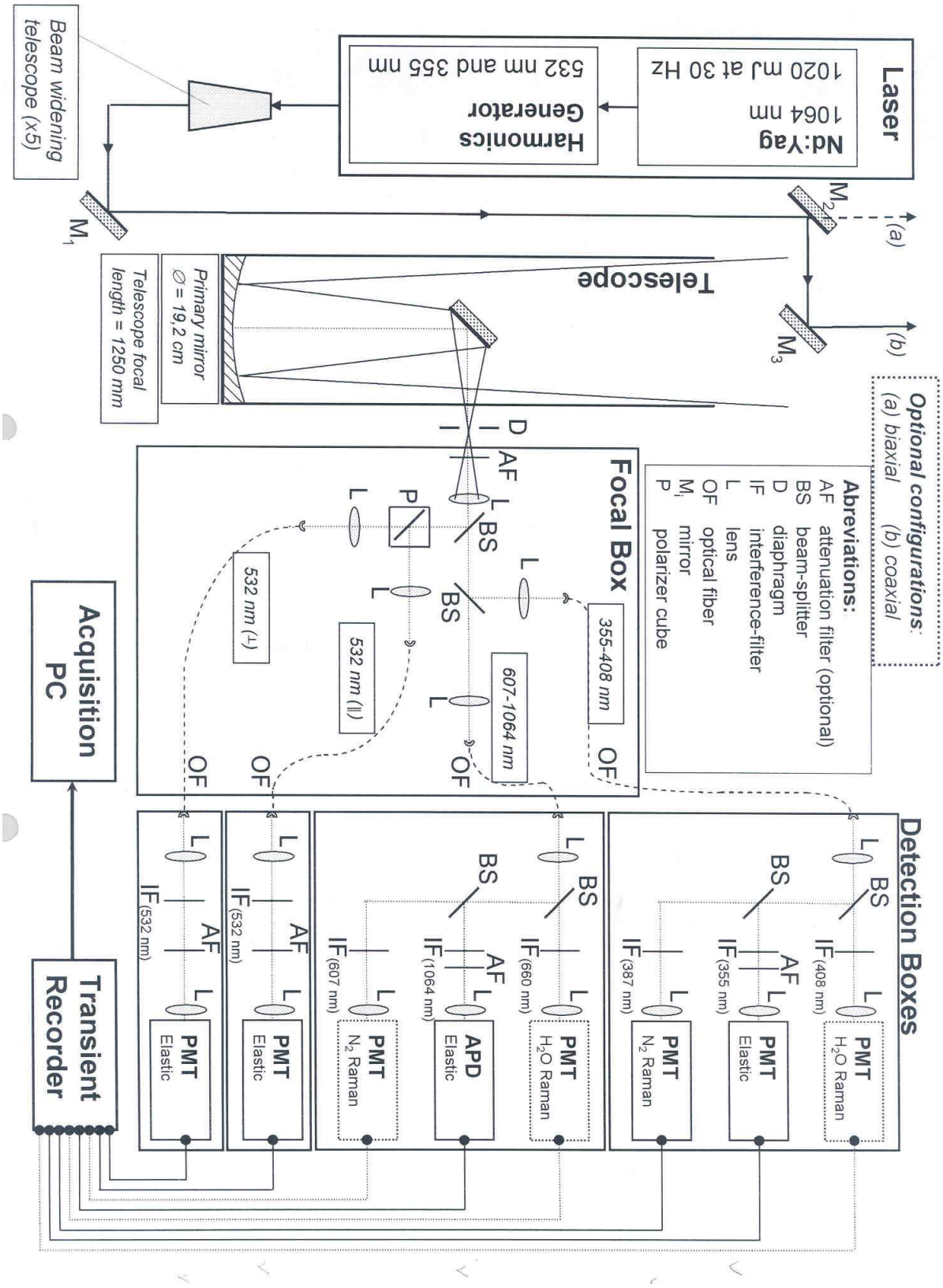

Figure 3.2: Setup of the tropospheric LIDAR. The dotted lines from the detection boxes to the transient recorder indicate channels that are not yet in use.

atmospheric constituents. The 532 channel has in addition the possibility to be parallel and perpendicularly polarized. The 532 light emitted is linearly polarised but when the light is received it can be more or less orthogonally polarized because of scattering. The ratio between the linearly polarized light received and the orthogonally polarized light can be used to find more information about ice structures in the lights path. The light beam is widened by the beam widening telescope after the beam has gone through the harmonics generator. This telescope widens the beam 5 times, and the beam divergence will at the same time be reduced to less than 140 μrad (Frioud et al., 2006a). Then the light is reflected by mirrors out of the observatory so that the beam is parallel with the receiving telescope. The positions of the last two mirrors decide the configurations of the LIDAR. There are two options: biaxial and coaxial. The axis of the emitted beam and the axis of the receiving telescopes view are parallel with the biaxial configuration, but they do not share the same axis. This means that the beam will have to reach a certain height before the telescope has the possibility to receive any scattered signal from the beam. This overlap problem will be described in the telescope section. The axes of the beam and the telescope are placed on top of each other with the coaxial configuration.

Telescope

The object of the telescope is to receive the backscattered light from the laser and guide it into the detection system of the LIDAR. Figure 3.3 shows that the telescope and the laser must be placed close to one another to have the full overlap between the laser beam and the telescopic view as low as possible. The signal will not give the information needed below the full overlap. In the case of the tropospheric LIDAR, the full overlap is at approximately 1 km. The telescope of the tropospheric LIDAR is of the Newtonian type and has a primary mirror with a 19.2 cm diameter, and the telescopic focal length is 1250 mm. The Newtonian type telescope is a reflecting telescope, which means that it uses mirrors, instead of lenses to form the image. The primary mirror of a Newtonian telescope is usually parabolic and the secondary mirror is flat. Another reflecting telescope in use with LIDAR systems is the Cassegrainian type. The received light is focused by the primary mirror onto a second mirror that directs the light into the focal box. The primary mirror for the Cassegrainian type is parabolic, and the hyperbolic secondary mirror reflects the light out of the telescope through a hole in the primary mirror. Figure 3.4 shows the light path through these two types of telescopes.

Focal box

The object of the focal box is to separate the different wavelengths the system can detect. First the light goes through a lens to focus the light to a parallel beam. The second obstacle for the light is a beam splitter that separates the 532 nm light from the rest of the wavelengths. Some of the 532 nm light may have changed polarization, and this effect needs to be accounted for. Therefore the light goes through a polarizer cube that splits the parallel polarized light from the perpendicularly polarized before it goes into the detection box. The rest of the light goes through a second beam splitter and is separated into one part with light from the violet part of the spectrum, 355-408 nm, and a second part with light from the red part of the spectrum, 607-1064 nm. After being split the light leaves the focal box through optical fibres and enters their separate detection boxes.

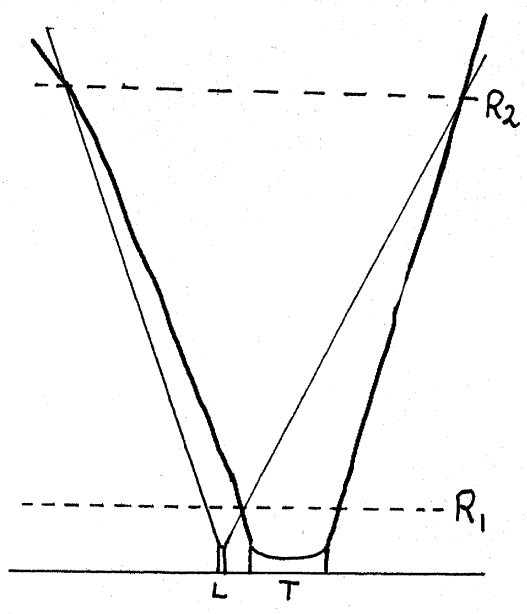

Figure 3.3: Overlap between the laser beam and the field of view of the telescope. T is the telescope, L is the Laser, R1 is the height where the overlap between the laser and the telescope begins, and R2 is the height where the full overlap begins.

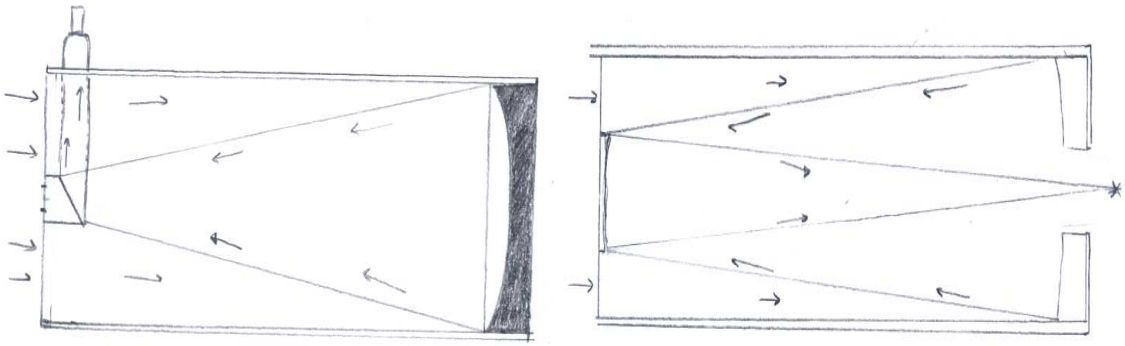

(a) Newtonian (b) Cassegrainian

Figure 3.4: Schematics for two types of telescopes in use with LIDARs

Detection Boxes

The object of the detection boxes is to detect the light. This is done either with photomultiplier tubes or avalanche photodiode detectors. These two instruments ensure that valid signals reach the transient recorder. Specifics about these two instruments can be found If more than one wavelength enters the detection box will these be separated before the light is transformed to electric signals. Some of the channels, for example 408 nm and 660 nm,

are not yet[4] put in to use. These channels are still accounted for in the description of the system because they could be put in to use later.

UV to Violet wavelengths: The light from the violet part of the spectrum is lead into its own detection box. Two beam splitters split the light into 408 nm, 387 nm and 355 nm in this detection box. The two violet channels, 408 nm and 387nm, go through an interference-filter, to exclude any other unwanted wavelengths, before entering the photomultiplier tube[5], in which the light is detected. The light closest to ultraviolet, 355 nm, goes through an attenuation filter in addition to the interference filter before entering the PMT.

532 nm[6]: The green wavelength has two detection boxes because this wavelength can be polarized in both parallel and perpendicular direction; both of these are detected individually. Before the light reaches the PMTs it goes through both interference filter and attenuation filter as for the 1064 nm light and the 355 nm light.

Orange to NIR wavelengths: This part of the light is on the edge between the near infrared (NIR) and visible part of the shortwave spectre. The NIR part ranges from 700 nm to 4μm. Two beam splitters in the detection box separate the light into 607 nm (orange), 660 nm (red) and 1064 nm (NIR). In the current set up of the LIDAR, only the 1064 channel is detected. Before it reaches the Avalanche Photodiode Detector (APD), it goes through both an interference filter and an attenuation filter.

Transient recorder and acquisition pc

The object of the transient recorder is to transform the light signals into electronic signals. These signals are then sent to the acquisition pc to be recorded. The transient recorder is of the LICEL TR 20-160 type, and for each channel the electronic signal is analyzed by one Analog and one photon counting mode. The photon counting mode is counting and analyzing every photon, so this mode gives information very accurately as long as the number of photons received simultaneously does not exceed a certain limit. For the ALOMAR Tropospheric LIDAR this limit is at 250 MHz. The Analog mode records the signal current. The recorded signal will therefore be more affected by noise in the system than for the photon counting mode, but it will be more accurate when the number of photons exceeds the photon counting mode limit. The Analog mode will also have its limitations, and the acquisition rate will therefore give the range resolution. For this system the raw resolution is 7.5 m. (Frioud et al., 2006a). The temporal resolution, the time between measurements is chosen to be 70 s.

In the acquisition pc all signals are recorded in the Licel raw data format, with an ASCII-heading, and then the atmospheric data from all channels in binary format. All measurements from the tropospheric LIDAR in this format, both atmospheric and noise, are collected in a database on the ALOMAR server with a hierarchical order where noises and atmospheric measurements from the same day are collected in the same folder. In addition to the measurement database, additional information, for example about weather conditions or tests of the system, is collected in a protocol book. This book is currently not in digital format, but may be digitalized in the future.

[4]spring 2008
[5]Further on: PMT
[6]Also called the green channels

3.1.2 Measurements taken with tropospheric LIDAR

When making measurements with the Tropospheric LIDAR at ALOMAR at least two sets of data should be recorded; a measurement of the atmospheric signal and a measurement of the background noise. If the conditions are favourable, several atmospheric and noise measurements can be made. If the atmospheric measurement time is more than a couple of hours, it can be useful to record noise signals from both before and after the atmospheric signal is made. This method will secure that the noise measured is as close as possible to the noise that is in the measured atmospheric signal. Actual noise measurements are made by blocking the laser while running the system. Measurements with the LIDAR are strongly dependent on weather conditions. Too many clouds, especially low thick clouds, might block the laser beam from reaching desired altitudes. The strong backscattering from these clouds can also overshadow more interesting signals below the clouds. Strong winds are also unfavourable since they may cause sand grains and other foreign objects to enter room with the telescopes, or strong turbulences that can damage the telescopes. If these small objects enter they can obstruct the light needed for the LIDAR by covering small areas of the mirrors or lenses, or even make scratches and lines that compromise the optical properties of these parts. Due to this, the hatch above the telescope room should not be opened when wind speed exceeds 12 $\frac{m}{s}$.

3.1.3 Retrieving Cloud height with the tropospheric LIDAR

The first variables which are useful to obtain when studying clouds are the cloud top and base height. First of all, these can be used together with temperature data to obtain the cloud temperature. With the temperature known, one can make a first assumption about whether there is a pure ice cloud, water cloud or mixed phase. These heights are also needed when calculating optical depth, for example in equation 3.1 where one integrates from cloud top to cloud base. But cloud heights will vary within a cloud system, because clouds generally are at least partially inhomogeneous(Platt et al., 1994). Information about cloud height depends on what one defines as the cloud edges. Platt et al. (1994) uses this general definition of cloud base: "..it is convenient to define cloud-base altitude as that altitude above which solid hydrometeors exist and can be detected, be they droplets, ice particles, or rain." There are a few different ways to obtain the cloud height, and which method that is used depends on the type of cloud one wishes to investigate and the quality of the signal (Platt et al., 1994).[7] The result from each of these methods might also depend on which wavelength that is used for the calculation. The smallest sized particle a specified channel can detect is proportional to the wavelength of the channel, so the 532 nm channels should be able to detect smaller particles than the 1064 channel. However in this thesis have the 1064 nm channel have been used in the cloud height calculation. This was because the heights calculated seemed to fit better with the cloud when the 1064 wavelength was used than when the 532 nm wavelength was used. This could have resulted from a stronger signal in the 1064 nm channel for the data used in this thesis. The fact that a lower wavelength would detect smaller particles also explains the differences in cloud height determinations between LIDARs and RADARs. The RADAR, which operates on a longer wavelength, will not detect smaller particles as accurately as the LIDAR. There will be a number of smaller hydrometeors around the cloud edges, because new particles

[7] More about scattering in the atmosphere can be found in appendix B.

begin to grow when entering the cloud, and old ones evaporate when leaving the cloud. The LIDAR will identify more of the small particles on the edge of a cloud and it may of this reason set the cloud base lower than the base height determined by RADAR.

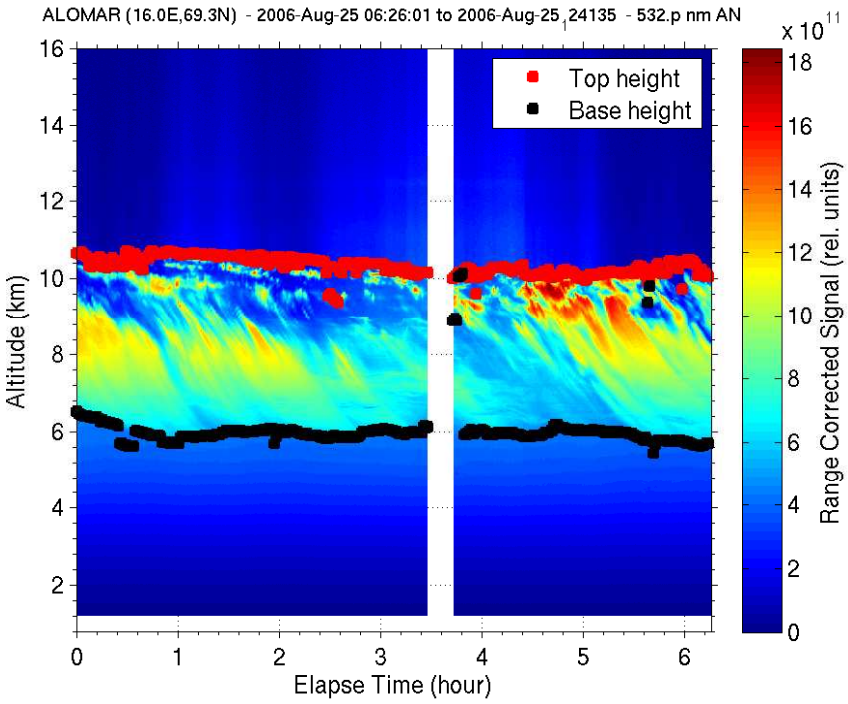

Figure 3.5: Detected cloud top and base altitudes 25 August 2006

One example of the cloud height calculations can be seen in figure 3.5. In this figure can it be seen that the fit between the cloud and the calculated cloud boundary heights is quite good. There are however some base heights that have been found too high, especially in the first set of measurement

The threshold method and two other methods for cloud detection is presented in the Platt et al. (1994) article. The threshold method is used for the cloud detection in this thesis. The objective of this method is to find the cloud boundary heights by comparing the signal from clear background air with the rest of the signal. The threshold value is found by taking the 3rd standard deviation of the signal in an area with only clear background air above the cloud. The third standard deviation is assumed to avoid noise spikes to be interpretated as clouds. If one assumes that the noise in the signal follows approximately the normal distribution will 99.7% of the noise values be within the 3rd standard deviation. The threshold value is compared with the signal. A cloud is found if the signal is larger than the threshold value. This testing for clouds would ideally begin with the signal at the highest range and down to the lowest. However, an upper and a lower limit have been set for the cloud detection instead. The higher limit is set because of noise problems. Analog channels have been used throughout this thesis and the Analog channels can be very noisy in the upper part of the channel (see section 2.4.2). The high amount of noise in the upper parts of the signal can be classified as clouds by the program if no upper cloud limit has been set. A solution to this problem could be to glue the signal from the Analog and the photon counting mode together, but this have not been done in this thesis. The lower limit is set because only cirrus clouds are supposed to be investigated. This lower limit

has been set to the altitude where the temperature is $-25°C$ or colder inn Goldfarb et al. (2001), a paper investigating cirrus with the threshold method. This value was reached at approximately 7 km in the data from Goldfarb et al. (2001). Since ALOMAR($69°N$, $16°E$) is situated further north than OHP[8]($44°N$ $6°E$) is this limit often lower than 7 km for the ALOMAR observatory. The values of these two limits have been changed to the best suitable value for each case, but in the one year climatology have the high cirrus limit been 15 km and the low cirrus limit been 6 km.

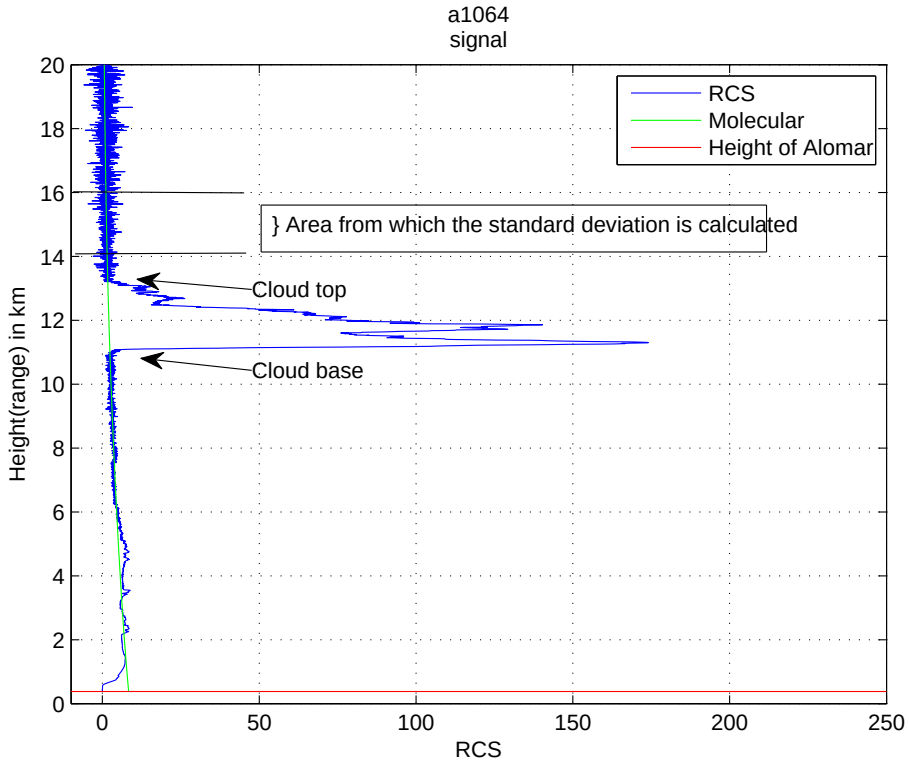

Figure 3.6: Principle of height determination by the threshold method. Range corrected signal is given in blue, the molecular profile is given in green and the red line gives the height of the ALOMAR site above sea level. This figure is made from the 12:35 profile from the 15th of September 2006. (Normalization heights: 9km/5km, Cirrus limits: 15km/6 km)

Figure 3.6 shows an ALOMAR LIDAR profile from the 15th of September. This particular profile was taken at 12:35 and was made with data from the Analog 1064 nm channel. An area with clear background air, from 14 km to 16 km, which is used to determine the threshold value is marked on the figure along with the cloud top and base. The 3rd standard deviation in the marked area is used as the threshold value. This threshold value is a possible error source in the height calculation. The cloud top might be underestimated because the noise in the marked area. The threshold value may be higher than the lidar signal value is at the actual cloud top height. The cloud base height might be overestimated by the same reason.

[8]Observatoire de Haute Provence(France)

3.1.4 Retrieving optical depth with the tropospheric LIDAR

A number of different methods exist for extracting the optical depth of clouds from LIDAR data. Four methods; the Molecular Integration method, the Particular Integration Method, the Klett Inversion Method and the Nitrogen Integration Method, are tested on datasets from two LIDARS in the Cadet et al. (2005) article. The Molecular Integration[9] method is based on evaluating the difference between the observed LIDAR return above[10] the cloud top and a theoretical molecular return in absence of a cloud. This method is used for retrieving the optical depth from elastic signals, but it is sensitive to the signal-to-noise ratio(Cadet et al., 2005). The method also depends on the existence of a particle free zone below the cloud to retrieve the optical depth. The Particular Integration Method[11] uses the following equation to find the optical depth:

$$\tau_c = \int_{z_base}^{z_top} LR(z')\beta_c(z')dz' \tag{3.1}$$

Where τ_c is the optical depth, z_{top} and z_{base} is the cloud boundary heights, LR(z') is the range dependent LIDAR ratio, and $\beta_c(z')$ is the range dependent particle volume backscattering coefficient. This method will in some ways be easier than the MI method, since it does not need a particle free zone, and it is less sensitive to the signal-to-noise ratio. The problem with this method is that one needs information about the effective Lidar ratio, and the Lidar ratio can vary within the cloud. This variable depends highly on the microphysical properties of the cloud and can range between 5 sr for small needles and 150 sr for hollow crystals(Cadet et al., 2005). The Klett inversion method is used to invert the elastic lidar data, and needs a reference extinction coefficient and a range independent value of the lidar ratio. This method uses the Klett forward and backward solution described in section 2.4.2 to find the optimal lidar ratio. The last method from Cadet et al. (2005), Nitrogen Integration, uses the inelastic Raman signal. This signal is only sensitive to the attenuation properties of the particles, and it is unaffected by the scattering properties. But the Raman signal is weak compared to the Rayleigh signals so this method can be less accurate. The Cadet et al. (2005) article concludes that the best way to determine the optical depth is to use a combination of the MI method and the PI method, and that for determining the optical depth on a routine basis, the PI is the best alternative. The PI method, through equation 3.1, have been used in this thesis to calculate the optical depth for a few cases in 2006. The particle backscattering coefficient has been found through the following equations found in Goldfarb et al. (2001). The scattering ratio(SR) is calculated first from equation 3.2, where $\beta_{aerosol} + \beta_{Rayleigh}$ is the raw signal[12], and $\beta_{Rayleigh}$ is the molecular backscattering.

$$SR = \frac{\beta_{aerosol} + \beta_{Rayleigh}}{\beta_{Rayleigh}} \tag{3.2}$$

$$\beta_{Rayleigh} = \sigma_{Rayleigh} * n_{air}(z) \tag{3.3}$$

$$\sigma_{Rayleigh}(532nm) = 5.7 \times 10^{-32} m^2 sr^{-1} \tag{3.4}$$

[9] MI method

[10] when the LIDAR is directed upwards in the atmosphere

[11] PI method

[12] The raw signal consist of the backscattering from both molecules, subscripted by Rayleigh, and aerosols/clouds, subscripted by aerosols

The molecular backscattering is found from equation 3.3, where $\sigma_{rayleigh}$ is the Rayleigh backscattering cross section, and $n_{air}(z)$ is the density of air found from the MSIS-model(Goldfarb et al., 2001). These equations can then be used to find the following equation for the particle backscattering coefficient:

$$\beta_c = \sigma_{Rayleigh} n_{air}(z)(SR(z) - 1) \tag{3.5}$$

The cloud boundary heights have been found with the method described in section 3.1.3. A constant value of 20 have been assumed for the LIDAR ratio(LR), which is close to the 18.2 sr value used in Goldfarb et al. (2001), even though this is a coarse assumption since the LIDAR ratio actually is range dependent. The equation for the optical depth can now be rewritten to what is used both in this thesis and the Goldfarb et al. (2001) article:

$$\tau_c = (LR)\sigma_{Rayleigh} \int_{z_base}^{z_top} n_{air}(z)(SR(z) - 1)dz \tag{3.6}$$

The optical depth has been found in the Analog 1064 nm channel. The limits of the optical depth for the different types of cirrus clouds (subvisible, thin, opaque and the limit to the thicker altostratus cloud in table 2.4) are based on data from the 0.694 μm wavelength(Lynch et al., 2002). These limits have still been used in this thesis, but must be considered as an approximation since the 1064 nm wavelength have been used and not the 649 nm wavelength. The two main error sources in this equation is the assumption that the LIDAR ratio is constant, which have been explained earlier, and the calculation of the cloud boundary heights. If the cloud boundary heights are not calculated correctly will parts of the cloud be left out of the optical depth calculation, or areas outside of the cloud will be included. This may therefore either lead to an underestimation, or an overestimation of the optical depth.

3.1.5 Retrieving depolarization ratio with the tropospheric LIDAR

An equation that connects the depolarization ratio(δ) with the returned lidar signal is needed to calculate the depolarization ratio. For an ideal system is this connection given by:

$$\delta = \frac{I_\perp}{I_\parallel} \tag{3.7}$$

Where $I_\perp$ and $I_\parallel$ is the scattering intensities for the perpendicular($\perp$) and parallel($\parallel$) polarization channels respectively. If the received power from the two channels is given this relation also be expressed with the backscattering cross section(β) and the atmospheric transmission(τ),. The received power(P_r) from the perpendicularly and parallel[13] polarized light is given by the following equations(Schotland et al., 1971):

$$P_{r\parallel}(Z) = P_{T\parallel} \frac{A_R h}{8\pi Z^2} \beta_\parallel(Z) \exp -2\tau_\parallel \tag{3.8}$$

$$P_{r\perp}(Z) = P_{T\parallel} \frac{A_R h}{8\pi Z^2} \beta_\perp(Z) \exp -(\tau_\parallel + \tau_\perp) \tag{3.9}$$

[13]In respect to the polarization of the transmitted light

Where P_T is the transmitted power, A_R is the effective area of the receiver telescope, Z is the range and h is the pulse length. The atmospheric transmission $exp(-\tau)$ is given for both the parallel polarization and the perpendicular polarization. These can differ if a stable orientation of ice crystals occur(Schotland et al., 1971). The depolarisation ratio is given by: $\delta = \frac{P_{r\perp}}{P_{r\parallel}}$ as for the intensities. The equation for the depolarization ratio can be simplified to the following because of the similarities between the equation for $P_{r\parallel}$ and $P_{r\perp}$:

$$\delta(Z) = \frac{\beta_\perp(Z)}{\beta_\parallel} exp(\tau_\parallel - \tau_\perp) \tag{3.10}$$

The equation 3.7 requires an ideal system, and bias in the results can therefore be created by non-ideal factors in the system. This problem can be avoided by taking these effects into account in the equation in the form of a constant. This constant, k, the overall effective cross-talk factor includes the cross-talk between the two polarization channels, and non-ideal properties of the optics in the system (Biele et al., 2000). A new equation for the depolarization ratio can be derived when one includes this factor along with the molecular depolarization ratio and uses the scattering ratio, given by this equation:

$$SR = \frac{\beta^R + \beta^A}{\beta^r} = 1 + \frac{\beta^A}{\beta^R} \tag{3.11}$$

Where A represents the aerosol or particle backscattering coefficient, and R represents the molecular or Rayleigh backscattering coefficient Goldfarb et al. (2001). When the scattering ratio is used, one can easily change between the volume depolarization ratio, which includes both molecular, and aerosol/particle effects and the aerosol/particle depolarization ratio which just include the aerosol/particle effect. The difference is in equation 3.11 where the scattering ratio includes a molecular part: $\frac{\beta^r}{\beta^r} = 1$ and an aerosol/particle part: $\frac{\beta^A}{\beta^R}$. Only the effect from the particles remains for the rest of the calculations when one is subtracted from the scattering ratio: $S - 1$. The equations for the volume depolarization ratio (subscripted by v) and the aerosol/particle depolarisation ratio (subscripted by a) is as follows: Alomar (2006b)

$$\delta_v = \frac{(k + \delta_m) \cdot SR_s^{meas} - k \cdot (1 + k \cdot \delta_m) \cdot SR_p^{meas}}{(1 + k \cdot \delta_m) \cdot SR_p^{meas} - k \cdot (k + \delta_m) \cdot SR_s^{meas}} \tag{3.12}$$

$$\delta_a = \frac{(k + \delta_m) \cdot (SR_s^{meas} - 1) - k \cdot (1 + k \cdot \delta_m) \cdot (SR_p^{meas} - 1)}{(1 + k \cdot \delta_m) \cdot (SR_p^{meas} - 1) - k \cdot (k + \delta_m) \cdot (SR_s^{meas} - 1)} \tag{3.13}$$

Where k is the overall cross-talk factor, δ_m is the molecular depolarization and SR is the scattering ratio. Equation 3.13 has been used in the calculations of depolarization ratio later in this thesis. One needs estimations of the cross-talk factor k and the molecular depolarization ratio δ_m to use these equations. An actual estimation of this factor in February 2006 gave $k \cong 3.2\%$Alomar (2006b). This factor may have changed during 2006, since another estimation from October 2005 gave $k \cong 4.7\%$, this change may lead to errors and more uncertainties in the calculations, but the k from 2006 is used due to lack of a later estimation. The effect of changing the value of k has been investigated in the results. The same presentation gave an estimation of the molecular depolarization ratio

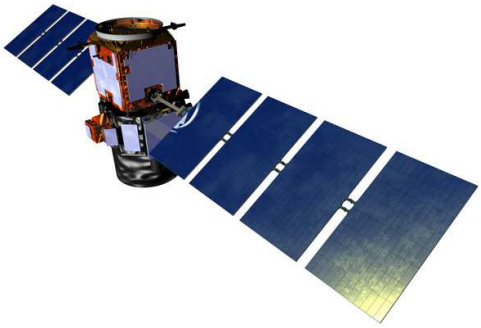

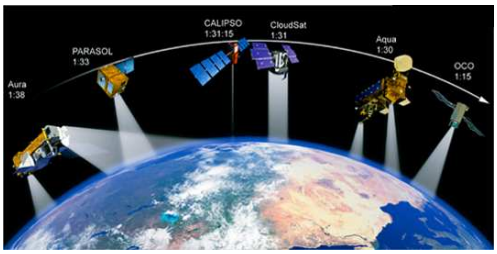

(a) The CALIPSO satellite. Source: http://www-calipso.larc.nasa.gov/resources/image_gallery.php

(b) The A-train constellation

for the ALOMAR optics: 0.37% which is the same as the value calculated earlier from the (Young, 1982) article.

3.2 Data from the CALIPSO satellite

3.2.1 Description of the CALIPSO satellite

The CALIPSO satellite was launched in 2006, as a part of the A-train constellation. The A-train constellation is a formation of six satellites; Aqua, CloudSat, CALIPSO, PARASOL, AURA and OCO(will be launched in December 2008 Orbital (2007)). These satellites all have instruments for atmospheric measurements. They follow the same path and the last satellite lags the first with approximately 15 minutes. The data from the various satellites will overlap because these satellites are flying in a formation. This will give an extensive view of the atmosphere and its components. The CALIPSO satellite carries a Cloud and Aerosol LIDAR with Orthogonal Polarization(CALIOP), an Imaging Infrared Radiometer(IIR) and a Wide Field Camera(WFC). Only data from the CALIOP instrument is used in this thesis. A summary of the CALIOP specifications can be found in table 3.2. The wavelengths, the spatial resolutions and the pulse rate of the CALIOP instrument are important things to note from this table. CALIOP operates on two wavelengths, 1064 nm and 532 nm. Both polarizations of the 532 channel; 532($\parallel$) and 532($\perp$), are detected.

The spatial resolution of the CALIOP system is originally 30 m in the vertical and 333 m in the horizontal(Winker et al., 2003). The data from the higher altitudes are averaged to reduce the required telemetry(Winker et al., 2003) so in the upper troposphere is the resolution 1 km in the horizontal and 60 m in the vertical, and in the stratosphere is the resolution 5 km in the horizontal and 180 m in the vertical. More about this resolution can be found in the next subsection. The pulse rate of the CALIOP system is 20.2 Hz which is lower than for the ALOMAR tropospheric LIDAR (pulse rate 30 Hz).

Characteristic	CALIOP
Laser type	Nd:Yag
Pulse rate	20.2 Hz
Wavelengths emitted	532, 1064 nm
Wavelengths detected	532($\parallel$), 532($\perp$), 1064 nm
Pulse energies	110 mJ each wavelength
Footprint	100 m
Spatial resolution:	
lower troposphere	333 m horiz. 30 m vert.
upper troposphere	1 km horiz. 60 m vert.
stratosphere	5 km horiz. 180 m vert.

Table 3.2: Specifications of CALIOP, the lidar onboard the CALIPSO satellite. Modified from Winker et al. (2003)

3.2.2 Description of the CALIPSO data products

The CALIPSO satellite project produces a range of data products, with several different uses. The data products available at the data ordering site from NASA (http://eoswwb.larc.nasa.gov/HBDOCS/langley_web_tool.html) are either Level 1 data products or Level 2 data products. This thesis uses Level 2 data products and these data were obtained from the NASA Langley Research Center Atmospheric Science Data Center. Six levels of data products are defined by the EOS[14](See page 6 of (Currey, 2006)). The Level 1 product available from the website is what EOS refers to as a Level 1B product. The data in this product is processed to sensor units and Geolocated. The Level 2 data are geophysical variables derived from the Level 1 data. These have similar resolution and location as the source data. The data products used in this thesis, are a part of the LIDAR Level 2 Cloud and Aerosol Layer Products. Clouds and Aerosols are reported separately in these products, and both the aerosol and the cloud data are generated at three different spatial scales: 1/3 km, 1 km and 5 km(Kusterer, 2007). The data product used in this thesis is the 1 km Cloud layer data, because of how the spatial scales and resolutions are connected. The three different products all range down to approximately 0.5 km below sea level, but the upper limits of cloud detection in the data products are limited by the spatial scales. The best spatial resolution is for the 1/3 km data products, but this product is only available up to 8.5 km above mean sea level. The next spatial scale: 1 km, is available up to 20.2 km above mean sea level. The last spatial scale, 5 km detects the information on a 5 km horizontal grid, and this product also includes stratospheric features. The Cloud data product with spatial scale 1 km will be the best to use, since the Cirrus cloud height range, as mentioned in section 2.1, is approximately from 6 km to 12 km. The full resolution of the 1/3 km layer products will be too low, and with the 1 km layer products will the resolution be better than for the 5 km layer.

The layer products consist of a number of data variables that can be one of two coupled data types. They can either be classified as column properties or layer properties(Kusterer, 2007). The atmosphere is then thought of as consisting of vertical columns that are measured. Measurements are then made and connected to these columns. Column variables

[14]Earth Observatory Systems

are variables that describe the location of the column, both temporal and geophysical. Typical variables from this data type are Latitude, Longitude and profile time. The layer properties are variables that belong to each detected feature, as optical depth or layer top and base altitudes. All information about the different properties can be found in Kusterer (2007). The column properties used in the calculations in this thesis are the Longitude, latitude, and profile time in UTC, Tropopause height. The latitude and longitude from the CALIPSO data is used to find the CALIPSO profiles that is closest to ALOMAR. These variables are given in degrees, and for the 1km layer product three laser pulses are averaged to generate the resolution and the value of the latitude and longitude are given from this temporal midpoint. Three values of the longitude and latitude are then reported. These are the value for the first and last pulse in addition to the temporal midpoint of these 15 shots. The profile time is used to compare the profiles between ALOMAR and CALIPSO in time. The best results will come from cases where the ALOMAR and CALIPSO measurements are close both in time and in space. The tropopause height is given in kilometres above the mean sea level. This value is derived by the Global Modelling and Assimilation Office (GMAO, more information on this can be found at http://gmao.gsfc.nasa.gov/overview.php) GEOS- 4 data product. This value is just used as an estimation of the maximal altitude at which cirrus clouds can reside. The layer properties used in the calculations in this thesis are layer top and base altitudes, and the midlayer temperature. Several other variables as layer optical depth and volume depolarization ratio are not yet available from the CALIPSO data. The layer top and base altitudes are compared with the ALOMAR data and used to see if the clouds detected by the ALOMAR LIDAR are similar to the clouds detected by CALIPSO.

3.2.3 Cloud detection with the CALIOP LIDAR

Two algorithm sequences are used to detect clouds in the data from the CALIOP LIDAR onboard the CALIPSO satellite. The Selective Iterated BoundarY Locator(SIBYL) is the first processing step of the CALIOP data(Winker et al., 2006). SIBYL identifies features in the LIDAR profiles by using a threshold method(Vaughan et al., 2005). A new threshold is found for each profile and altitudes are marked as a boundary for a feature if the signal exceeds this value. The next processing step is to identify the feature with the Scene Classification Algorithm (SCA)(Winker et al., 2006). The tropospheric features are first parted from the stratospheric features based on a height comparison. Clouds features are then parted from aerosol features based on the value of the 532 nm attenuated backscatter coefficient and on the value of the attenuated colorratio[15](Liu et al., 2005). More about CALIOP algorithms can be found in the following CALIOP Algorithm Theoretical Basis Documents: Winker et al. (2006), Vaughan et al. (2005) and Liu et al. (2005).

All altitudes detected from the CALIPSO data are given in km above mean sea level. The vertical resolution of the LIDAR in the altitude range for cirrus is 60 m (-0.5 km to 8.2 km: 30 m vertical resolution, 8.2 km to 20.2 km: 60 m vertical resolution, and above 20.2 km is the vertical resolution 180 m.) There are however many uncertainties in the detection of these altitudes, as for the cloud altitudes are calculated from the ALOMAR data. Weak scattering features are more difficult to detect from the background than strong scatterers and this may lead to errors form the actual cloud altitudes. This is especially a problem for optically thin cirrus. The confidence in the calculated height of the lower layer will

[15]ratio between the mean attenuated backscatter coefficient at 532 nm and 1064 nm.

be less than the confidence in the calculated heights for the higher layers if several cloud layers are detected in a profile. This is due to the signal attenuation from the overlaying clouds. This will not be the biggest problem when concerning cirrus clouds as they are often the highest clouds in profiles with multiple cloud features. ALOMAR measurements are only made during fair weather conditions with low cloud coverage, so this will not pose a problem in those measurements. The reported top altitude will have a better confidence than the base, since the base is detected after the signal has been attenuated by the cloud feature. The signal will then have been partially attenuated. The heights where the feature ends and the molecular atmosphere begin will there be increasingly difficult to find the due to noise issues.

This problem is reversed for the ALOMAR data, where the cloud base is detected with higher confidence than the cloud top, as the ALOMAR LIDAR measures from the base up and not from the top down as the satellite does. The detected base altitude for opaque features will in addition be an apparent height, and not the actual height, as the signal is attenuated and does not completely penetrate the cloud. This does not pose any problems with cirrus clouds as they are thinner. A last thing to have in mind is that the detection of exact cloud altitudes is more reliable for measurements made during night, than for measurements made during the day. This is because there is less noise when no sunlight is present. It is not as straightforward as for the ALOMAR data to extract information about cirrus clouds from the CALIPSO data. The ALOMAR tropospheric lidar is only operated during fair weather conditions and if any high density clouds are encountered will the measurements be stopped. These clouds will not be completely penetrated by the ALOMAR LIDAR. This means that it is likely that any cloud reported is a cirrus cloud. The CALIOP LIDAR, on the other hand, operates under all atmospheric conditions, and the weak scattering of cirrus clouds is easily lost when other scattering clouds are present. It is therefore not enough to just count the number of clouds to find the cirrus coverage. The cloud type needs to be determined first. There will be given information about the cloud type within the cloud and aerosol layer products in the future. The variable Feature Classification Flags will include information about the feature subtypes, but this is still not implemented for the current release. The cirrus extraction has therefore only been based on the altitudes of the cloud base and top. The top altitude have been compared to the tropopause height from the CALIPSO data, an any feature with top height above this level was not classified as a cirrus by the program. The base height limit was set to 6000 m as for the ALOMAR data

3.2.4 Comparing the CALIPSO and ALOMAR data

One needs to find the closest position either in time or in space to find the best fit between the CALIPSO and the ALOMAR data. The data should ideally be extrapolated to the actual ALOMAR location, but to do this one needs a proper estimation of the wind speed and direction. Morille et al. (2007) states that the closest in time approach should be used when comparing two sets of measurements from different instruments if the paths of the two instruments are parallel. The closest in space approach should be used when the path is perpendicular. The closest position in space has been used in this thesis, since the ALOMAR Lidar is stationary. The satellite moves at a very high velocity so that the closest position in time could be very far away from the ALOMAR location. The time difference between the CALIPSO and ALOMAR measurements will not necessarily be too

large when the CALIPSO satellite is at its closest location. All distances between ALOMAR and CALIPSO have been found by calculating the difference between the ALOMAR location($69°N, 16°E$) and the latitude and longitude given from the CALIPSO profiles. The shortest distance found was used as the closest profile to ALOMAR. The closest position in time was found by comparing the time of the middle profile from the ALOMAR profiles for the case with the time of the CALIPSO measurements. The CALIPSO profile closest to this profile was used as the closest fit to the data for the day in question.

3.3 Data from the MSIS-90 model and radiosondes

3.3.1 Description of the MSIS-90 model

The MSIS-90 model is used to get a molecular profile of the atmosphere and a temperature profile. This model can be found at the NASA web pages at http://modelweb.gsfc.nasa.gov/models/msis The model is based on an earlier tabulation of zonal averaged temperature and pressure, which have been supplemented with several other measurements(Hedin, 2006). This model is convenient because it gives easy access to profiles for specific latitudes and longitudes. There are two possible output tables from the MSIS model. The first table includes profiles of the neutral temperature, the exospheric temperature and the density of O, N_2 and O_2, in addition to the total density. The second includes profiles of the neutral temperature and the density of He, Ar, H and N. The first output table has been used since only the total density and the neutral temperature is needed here. The total density from the model is interpolated to have molecular profile values in the same levels as the LIDAR profile values. The LIDAR profile values are given for every 7.5 m above the ALOMAR site.

3.3.2 Calculating the molecular signal

The molecular signal is calculated with the scale function which scales the data from the MSIS model to the RCS. This assures that the molecular and LIDAR signal are comparable.

The total density from the MSIS model is also used to calculate the variable betam532, which is used when calculating the LIDAR ratio and optical depth. This variable is the combination of the $\sigma_{rayleigh}$ and $n_{air}(z)$ variables used to calculate the optical depth in Goldfarb et al. (2001). In this article the optical depth is calculated by the following equation:

$$\tau_{cirrus} = (LR)\sigma_{rayleigh} \int_{z_{min}}^{z_{max}} n_{air}(z)(SR(z) - 1)dz \tag{3.14}$$

In this equation LR represents the LIDAR ratio which is defined as the ratio between the extinction coefficient α and the backscattering coefficient β:

$$LR = \frac{\alpha(r)}{\beta(r)} \tag{3.15}$$

The variable n_{air} is the density of air calculated by the MSIS-E-90 atmosphere model, and SR represents the scattering ratio which is defined by the following relationship between

[16]Last accessed: 10th march 2008

the molecular and particle backscattering coefficient:

$$SR = \frac{\beta_p + \beta_m}{\beta_m} \tag{3.16}$$

The last variable in this equation is the Rayleigh backscattering cross section: $\sigma_{Rayleigh}$. The AMS glossary[17] states that the backscattering cross section is 'the ratio of the intensity scattered in the direction toward the source to the incident irradiance'. Rayleigh backscattering is an appropriate name as molecular scattering is a form of Rayleigh scattering, since the scattering medium in this case is the molecules in the atmosphere.(More about atmospheric scattering can be found in appendix B) This is a variable that together with the density of air gives the molecular backscattering coefficient: $\beta_{Rayleigh} = \sigma_{Rayleigh} * n_{air}(z)$. The $\sigma_{Rayleigh}$ value used for the 532 nm channel was given in Goldfarb et al. (2001): $\sigma_{Rayleigh}(532nm) = 5.7 \times 10^{-32} m^2 sr^{-1}$.

3.3.3 Retrieving the Temperature profile from MSIS and radiosonde data

A temperature profile is needed to check whether the temperature in the cloud layer is below the temperature needed for pure ice clouds. The temperature profiles used in this thesis are from radiosondes and from the MSIS model. The radiosonde measurements were made at Bodø radiosonde station($69°N, 14°E$) which have been in operation since 1957(Arntzen and Lystad, 2006). The measurements where accessed from the WebPages of the University of Wyoming: http://weather.uwyo.edu/upperair/sounding.html. These radiosonde measurements have been given as Stuve/Skew-T diagrams, and the cloud temperature and the height of the tropopause have been found from these. Actual radiosonde measurements are better than using the calculated data from the MSIS model, since model estimations can differ from the actual temperature MSIS model data was still used in the last case, 14 September 2006, because no radiosonde measurements were available from the Bodø radiosonde station at this date. As the molecular density is the temperature data from the MSIS model interpolated to the same levels as the LIDAR profiles have values.

3.4 Satellite images and Weather charts

The satellite images is from the Dundee Satellite Receiving Station[18], which stores satellite images from NOAA, SeaStar, Terra and Aqua polar orbiting satellites. Images from AVHRR, the scanning radiometer onboard the NOAA satellite, have been used(NOAA). This radiometer operates on five channels which include both visible and infrared wavelengths. The fifth channel been used in this thesis. This channel operates on 11.5-12.5 μm(AVHRR). This channel is used to find sea surface temperature in addition to day and night cloud mapping. The IR satellite images have been used since cirrus clouds are more easily seen in these images than in the visible satellite images(Lynch et al., 2002). The cloud features found in these images are compared with the weather charts and the clouds found in the LIDAR data.

[17] http://amsglossary.allenpress.com/glossary
[18] www.sat.dundee.ac.uk/

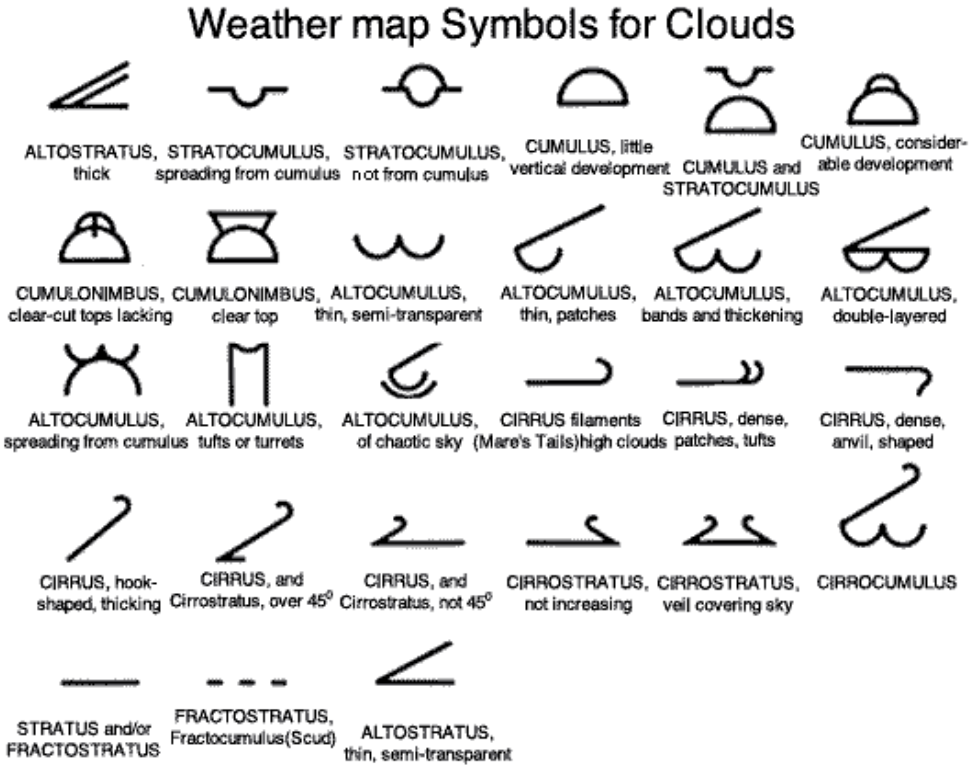

Figure 3.7: Cloud symbols used in the synoptic observations in some of the weather charts that can be found in the results. Source: www.weather.about.com/od/forecastingtechniques /ss/mapsymbols_5.htm (Accessed: 18.03.08)

All the weather charts used in this thesis are from the archive of DNMI[19] and made in their digital analysis tool DIANA. The charts cover the northern part of Europe, and display the main synoptic features that influence the clouds seen in the other data. The charts are chosen within the time period that measurements where taken with the tropospheric lidar for each case. Each analysis has two charts, one chart is an overview of the synoptic features in the north European area at that time, and the second is a closer view of northern Norway that also include observational data. The three cases used in this thesis have the following weather analysis charts. The 15th of August has charts from 18:00 (figures 4.15(a) and 4.15(b)). The 25th of August has charts from 09:00 (figures 4.23(a) and4.23(b)). The 15th of September has charts from 12:00 (figures 4.31(a) and 4.31(b)).

The cloud symbols used in the observational data can be seen in figure 3.7. The important symbols to note are those for cirrus cloud and those for altocumulus clouds, as these are often seen in the later results.

[19]Det Norske Meteorologiske Insitutt (The Norwegian Meteorological Insitute)

3.5 Rationale for obtaining information on cirrus cloud properties

Cirrus clouds can not be approximated as blackbodies, and they will also display a wide variability of optical properties because of the different ice crystal structures. This makes it difficult to obtain information about them with visible or IR radiometers (Liou, 1986). Data from satellites which only use passive remote sensing instruments is of the same reason less reliable. To obtain good information about cirrus with passive remote sensing tools, one usually has to combine data from several channels, and even from several instruments.

Another problem with obtaining information about cirrus clouds is their height; ice clouds are usually located just below the tropopause. This makes insitu measurements, for example plane campaigns, both time consuming and expensive even though they give valuable information about the cloud properties.

To obtain good, but also cost effective day-to-day measurements of cirrus clouds s it best to use active remote sensing tools as the LIDAR. There are several different variables that can be extracted from the received LIDAR signal, as the optical depth, heights and depolarization ratio. The LIDAR operates on a shorter wavelength than for example RADAR. This means that smaller particles can be detected. Height measurements with the LIDAR will for example be more accurate than measurements of the height with RADAR. The LIDAR is also a good tool for obtaining information about optical properties, and this is of vital importance when dealing with cirrus clouds. The crystalline shape of the ice particles will scatter the light more complexly than the spherical water droplets and therefore exhibit a wider range of possible optical quantities to obtain. The LIDAR has the advantage of operating with light with a well-defined polarization, with this information one can distinguish between ice and water in the clouds. The polarization of the light will in addition when be able to give more information about the ice crystals in the cloud. Measurements by the LIDAR of low and middle clouds, which are mostly water clouds, will be less good than for cirrus clouds due to absorption by the cloud particles and multiple scattering effects (Liou, 1986). Another problem with these types of clouds is that they generally have a larger optical thickness, and the LIDAR signal can be attenuated before the light has reached through the cloud. But the Lidar might be a good choice for cirrus and aerosol research.

Chapter 4

Results

This section begins with a one year climatology of the ALOMAR data from 2006. A short test of the k-value in the depolarization ratio equation is also included. Three cases are presented from this year. All the cases include LIDAR data from ALOMAR and CALIPSO, temperature data, satellite images and weather charts. The variables that are discussed in each case are the cloud heights, the optical depth and the depolarization ratio. The weather situation is discussed in the end of each case.

4.1 One year climatology: 2006

4.1.1 The ALOMAR database

The tropospheric LIDAR has been in operation since 2005. It has a database which included three years of measurements at the beginning of 2008. These three years was 2005, 2006 and 2007. The measurements can be divided into three types: regular atmospheric measurements, noise measurements, or test measurements. Noise measurements are measurements made by blocking the laser beam, and these are made to remove the noise from the atmospheric measurements. Test measurements are for example made when testing and adjusting the system. The 2006 data have been chosen as the dataset for this thesis since the CALIPSO measurements began in 2006 and several measurements where made with the tropospheric LIDAR during this year. A short statistical analysis has been made for this year, and cases, with both CALIPSO and ALOMAR data, have been chosen from the latter part of the year. The following figures show how measurement hours are distributed during these 2006.

Figure 4.1 shows the monthly distribution of the atmospheric measurement hours during 2006. The highest number of measurement hours where made in February. During this month was 111 measurement hours made. The second half of the year is the most interesting as these data can be compared with the CALIPSO data. It can be seen from the figure that several measurements were made from August until October, which is the early fall. Measurements from the winter season are wanted due to less light disturbance (night time lasts longer and there is less sunlight entering the receiver). There are no measurements during November and December in 2006, as can be seen from figure 4.1 The reason for this lack of atmospheric measurements during these winter months is a combination bad weather and problems with the equipment. Strong winds and precipitation can damage the telescopes, and the laser beam can not penetrate heavy cloud layers. The Lidar can

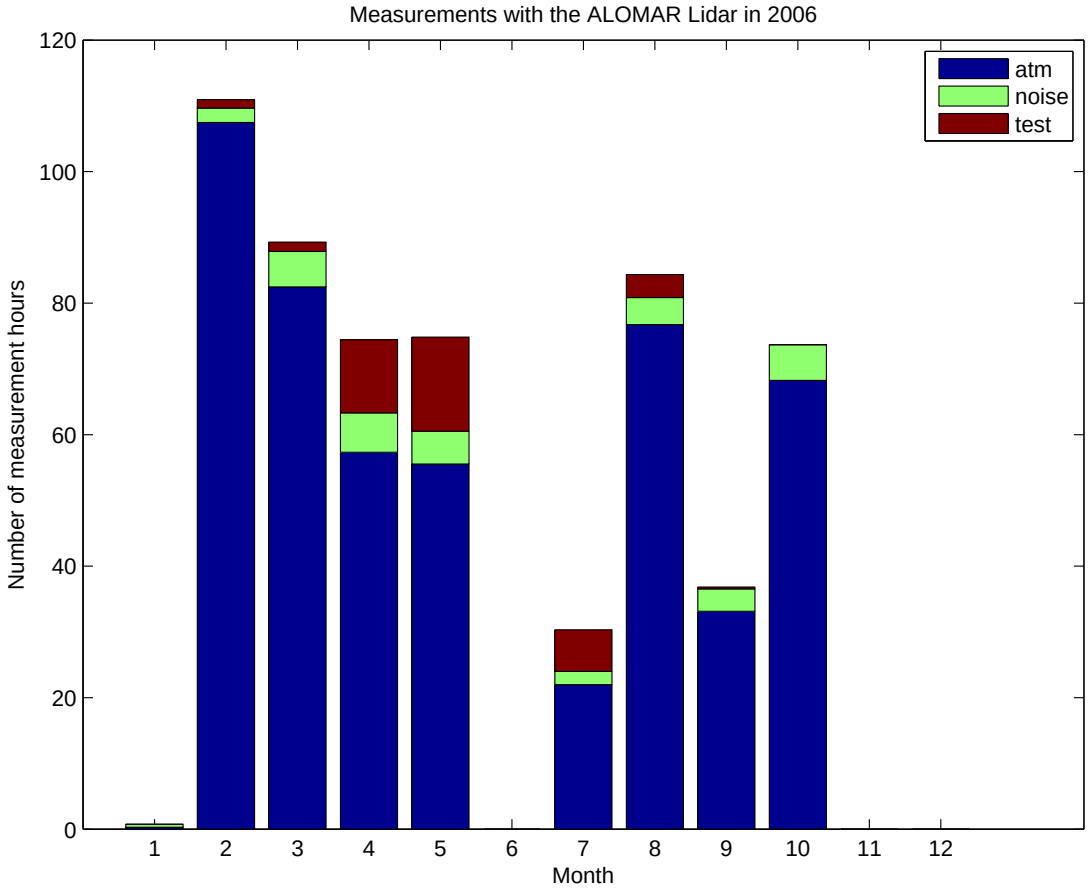

Figure 4.1: Number of measurement hours. The total column for each month consist of atmospheric measurements in blue, noise measurements in green and test measurements in red.

not make atmospheric measurements during such conditions. Problems with the lidar were discovered during October 2006, and technical work on the lidar in addition to bad weather lead to these months without measurements. The CALIPSO satellite was launched in June 2006 and there are data from 13th of June this year. The main focus has therefore been on the August to October measurements as these can be compared with the CALIPSO data. The highest number of measurements in this period is in August with 84 measurement hours, and two of the cases were found in this month: the 15th and the 25th of August. The last case chosen was the 15th of September.

4.1.2 The CALIPSO database

The CALIPSO database consists of data from the beginning of June 2006 up until the present day. These data include measurements from the CALIOP lidar and the Imaging Infrared Radiometer and images from the wide field camera. There are different versions of the data depending on the processing made. Both version V1.21 and V2.01 of the CALIOP data are available for browsing. These data can be found on the NASA webpage

Beta:	Early release products for users to gain familiarity with data formats and parameters. Users are strongly cautioned against the indiscriminate use of these data products as the bases for research findings, journal publications and/or presentations.
Provisional:	Limited comparisons with independent sources have been made and obvious artefacts fixed.
Validated stage 1:	Uncertainties are estimated from independent measurements at selected locations and times.
Validated stage 2:	Uncertainties are estimated from more widely distributed independent measurements.
Validated stage 3:	Uncertainties are estimated from independent measured representing global conditions.

Table 4.1: **Maturity Level Definitions:** The maturity of both the products and the individual parameters are indicated from these quality designators. This table is taken from Langley (2008)

http://www-calipso.larc.nasa.gov/products/lidar/browse_images/production/[1]. The version V2.01 displays data with much less noise than the earlier version, but are not yet available for the full dataset. The data available in this version includes the 2006 data, the two last months of the 2007 data and the 2008 data. The different data products are all followed by a quality statement to explain their reliability. An overall summery and links to the product specific quality statements can be found in Langley (2008). The maturity levels of the data are also described in Langley (2008). This level gives a description of the quality and what uncertainties that follows a specific product. The different maturity levels can be found in table 4.1.

The data used in this section are the LIDAR level 2 cloud and aerosol layer information product. The latest release of data was is January 2008, with the 2.01 version of the data. The maturity level of the level 2 Cloud and aerosol layer information was then Provisional. This means that the data should still be treated with caution, but any obvious errors have been removed. The quality statement for this individual data product(Langley, 2008) states that the estimation of the layer heights are quite accurate, with the exception of the previously mentioned uncertainties(3.2.2). The discrimination between clouds, aerosols and stratospheric features are also mentioned in this quality statement. This discrimination has maturity level Beta, and some misclassifications can therefore occur. One problem that can occur is that dense aerosol layers may be wrongly classified as clouds. Another problem is that parts of the bases of some cirrus clouds can be wrongly labelled as aerosol. These problems must be taken into consideration when analysing the CALIPSO data.

4.1.3 2006 measurements with the ALOMAR tropospheric lidar

Figure 4.2(a) shows the number of measurements hours that were taken in each month during 2006. A significant number of measurements where made in only eight of the months in 2006. Cirrus clouds were detected in some of the profiles, and this is displayed

[1]accessed: 27.02.08

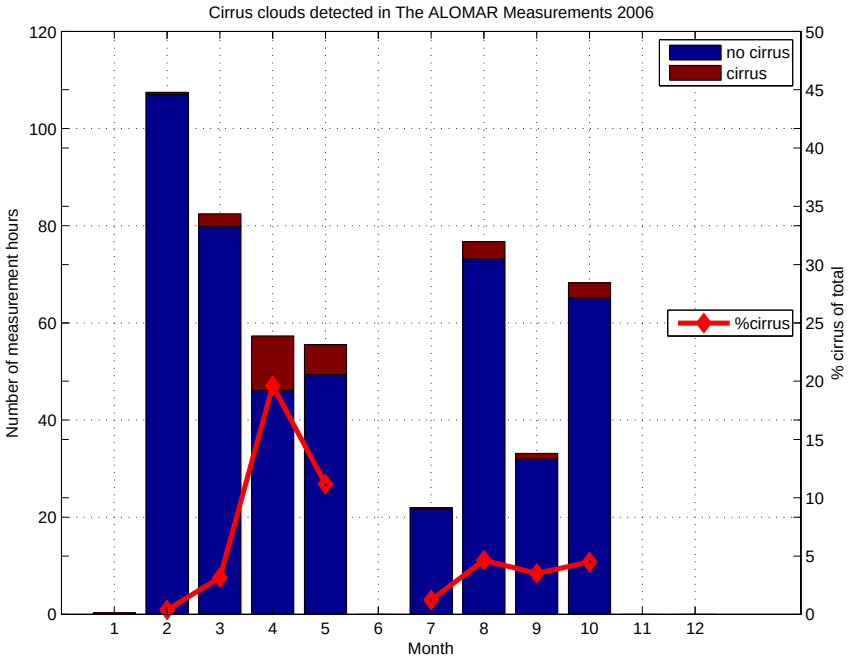

(a) The total hours of atmospheric measurements in each month during 2006. The column for each month is parted in two: the hours with detected cirrus and the hours without detected cirrus. The percentage of cirrus found in each month is marked with a red line.

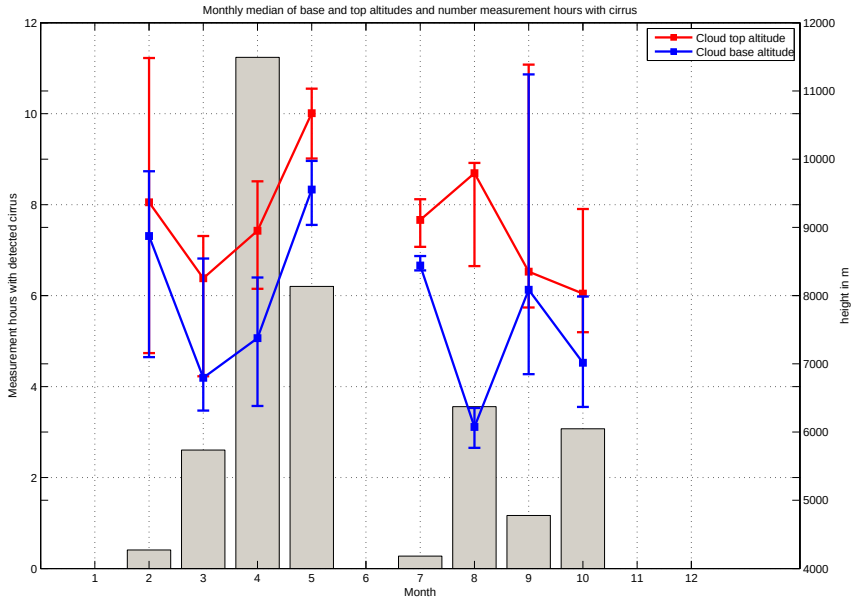

(b) Median cloud top and cloud base for each month. The spread of the top and base altitude is also shown. The top altitudes are given in red and the base altitudes are given in blue. The number of measurement hours with cirrus is also given as a grey bar plot.

Figure 4.2: Plots of the measurements during 2006

in the figure as a part of the total number of measurement hours and as a percentage of the total number of measurements. The highest number of measurement hours, more than 100 hours, was made in February. The number of measurement hours in a month usually lay between 40 and 80 hours of measurements in 2006. This can also be seen in figure 4.2(a). There is a difference between the first and the second half of the year when concerning the number of measurement hours. The former half of the year has generally a higher number of measurements in each month. The mean number of measurements in the four months with significant numbers of measurements in the first half of the year is more than 70 hours, but for the latter half of the year is this number less than 50 hours[2]. The percentage of cirrus clouds in each month was found as follows: $\frac{\text{measurements with cirrus}}{\text{total measurements}} \times 100$. The highest percentage of cirrus clouds was 19.6% in April. This is much higher than what was seen in most of the other months. The median value was around 4%, which is close to the percentage in more than half of the months.

Figure 4.2(b) show the cloud top and base altitudes for each month in addition to the measurement hours with cirrus. The cloud top and base altitudes are displayed as the median from each month, and the spread in the heights from each month are also shown. The spread is displayed as the 25th and 75th percentile of the data. The lines from the median to the 25th and the 75th percentiles show the closest 25% of the data below and above the median. The highest mean top and base altitudes are in May, the mean top is then at 10673 m and the mean base is at 9555 m. These numbers can be found in table 4.2 and table 4.3 at the end of this section. These tables show the minimum, the maximum, the median, the 25th and 75th percentiles and the standard deviation of the cloud top(table 4.2) and base(table 4.3) altitudes. The lowest top altitude is in October. The median top altitude is then only 8029 m. The lowest median base altitude is 6075 m and can be found in August. The lowest spread in both the top and base altitudes can be found in July. The grey columns in figure 4.2(b) show the number of measurement hours in each month and the column for July is the lowest of the eight months in which cirrus was detected. The low spread in July could be partially explained by the low number of measurement hours. Only two days in the July measurements had cirrus and these had very similar heights. However, the other month with a low number of cirrus measurement hours, February, has a large spread in the cloud altitudes. Cirrus was detected in 3 days from this month and the heights varied a lot during these days. May has a much higher number of measurement hours with cirrus in them, and still shows a fairly low spread in both the top and the base altitudes. The highest spread in both top and base can be found in September. This could mean that the clouds in this month are more variable in size and height than for example the clouds in May. The highest number of measurement hours with cirrus clouds detected was made in the late spring, during April and May 2006. The number of measurement hours with cirrus was more than twice as much in April and May than in the rest of the months in 2006. 11.2% of the measurement hours in May have cirrus in them, and in April was this number 19.6%. These two months with a high amount of cirrus were followed by a month with no measurements. There are several reasons for low amounts of measurement hours. The LIDAR is only operated during fair weather conditions to keep the telescopes damage free. There have also been some technical problems that have limited the number of measurement hours. How many hours of measurement that has been taken is also dependent on the work load of the staff at ALOMAR. The system will go

[2]these numbers exclude the months with no measurements(June, November and December), and the month with to few measurements(January)

unused even though the conditions are suitable for measurements if no staff is available to run the system.

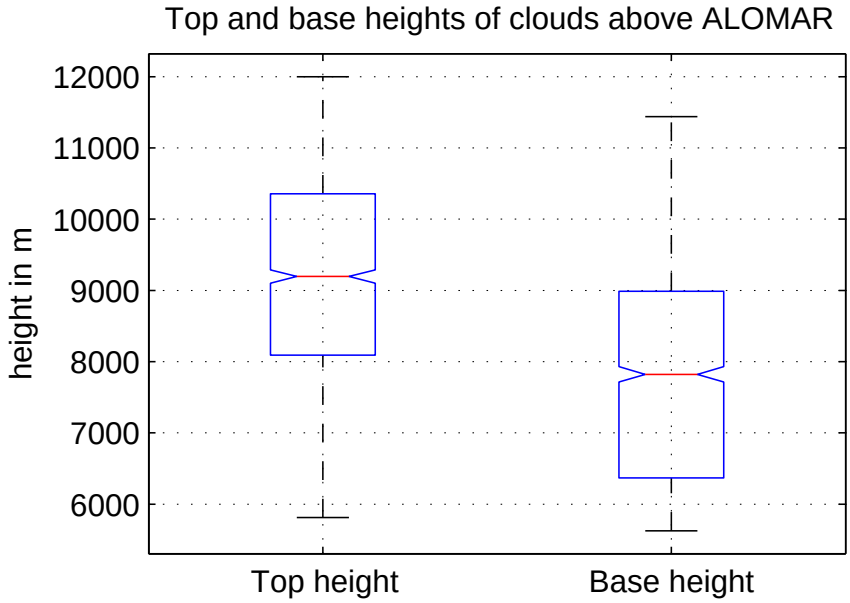

Figure 4.3: Mean top and base altitudes from 2006, the red line is the median, the top and bottom of the box is the 75th and 25th percentiles, and the black lines are extended out to the maximum and minimum values in the dataset.

The last figure in this section, figure 4.3, is a box plot of the top and base altitudes of the detected cirrus clouds above ALOMAR. This is the same data as in figure 4.2(b), but this is for the year as a total. This figure shows the median of the data, the interquartile range and the highest and lowest values. The median is given by the red line, and blue box spans the interquartile range. The top and bottom of the box are the 25th percentile and the 75th percentile. These values give an estimation of the spread of the data. The highest and lowest values are marked with the lines extended above and below the box. The median of the top altitudes are at 9 km, and the spread of the top altitude is between approximately 10 km and 8 km. The median for the base altitude is at around 7.5 km and the spread is a bit larger than for the top altitude, between 6 and 9 km. The maximum and minimum values for the top and base are 12 km and 6 km respectively. These values are the limit values set in the program that calculates the altitudes. The program uses 12 km as a higher limit for the clouds when calculating the height for the total year. The lower limit of the cirrus clouds are set to 6 km when calculating for the total year. This lower limit can be improved by replacing it with an altitude found from comparisons with temperature profiles. The altitude where the temperature sinks below $-25°C$ be found from such temperature profiles. More about extracting the cloud altitudes from the lidar data can be found in section 3.1.3. The proper cloud limits will not be found if the molecular profile can not be scaled to the lidar signal. Only one molecular profile has been used when calculating these values for the total year. This profile is from January 2006 and is probably just useful for the winter half of the year. The best improvement would be to have temperature profiles and molecular profiles for each measurement day to compare with. This is however difficult to obtain, but some sort of improvement should be made in

Month	min	Q_1	median	Q_3	max	std
Total	5813	8093	9195	10356	12000	1490
January	-	-	-	-	-	-
February	7005	7157	9368	11483	11573	1977
March	5820	6818	8254	8873	12000	1858
April	5963	8100	8951	9675	12000	1229
May	6968	10009	10673	11033	11610	855
June	-	-	-	-	-	-
July	8400	8715	9109	9413	10298	569
August	6345	8432	9795	9945	12000	1255
September	6758	7826	8351	11385	11588	1802
October	5813	7463	8029	9270	11618	1550
November	-	-	-	-	-	-
December	-	-	-	-	-	-

Table 4.2: Statistical variables for the cloud top altitudes during 2006. All altitudes are given in meter. Values given are the minimum, the maximum, the median, the standard deviation and the first and third quartiles. The quartiles give information about the spread of the data.

Month	min	Q_1	median	Q_3	max	std
Total	5625	6369	7823	8989	11438	1551
January	-	-	-	-	-	-
February	6960	7099	8873	9823	10920	1411
March	5625	6315	6795	8543	10905	1279
April	5633	6383	7376	8265	10440	1139
May	6668	9036	9555	9975	11430	942
June	-	-	-	-	-	-
July	8243	8370	8441	8580	10193	498
August	5625	5769	6075	6353	10763	1051
September	6240	6848	8085	11243	11438	1943
October	5640	6368	7016	7988	11040	1400
November	-	-	-	-	-	-
December	-	-	-	-	-	-

Table 4.3: Statistical variables for the cloud base altitudes during 2006. All altitudes are given in meter. Values given are the minimum, the maximum, the median, the standard deviation and the first and third quartiles. The quartiles give information about the spread of the data.

further studies.

4.2 Comments to the data presented

4.2.1 Presentation: plots and graphs

The figures in this section are made with two types of programs that get the range corrected signal from the measured data. The program that makes the Quickplot images as figure 4.9 and the similar part of figure 4.10 gives the best view of the data. The other program, which is used to find the heights plotted on the Quickplot in figure 4.10 and variables plotted in other figures, is a bit simpler and it gives a weaker RCS. This algorithm has also less noise correction than the Quickplot algorithm. The Quickplot algorithm has been used only for the Quickplot. This has been done to have Quickplots that are easy to understand, and to avoid having to rewrite multiple programs. The results might improve if this method is used in the rest of the calculations too. All results are found using the Analog 532(||) nm channel (except for the depolarization ratio which uses both the parallel and perpendicular 532 channel).

4.2.2 Validation: uncertainties and error sources

climatology

The figures in section 4.1.3 is not fully reliable because of the way the clouds are detected. Whether or not a cloud is detected by the program depends on many factors. The choice of the molecular profile might cause errors in the climatology because only one molecular profile, from January, is used to normalize the data. Clouds can go undetected if the molecular profile does not fit properly to the LIDAR data. This can happen since the molecular profile changes over the year. How well this molecular profile fits with the LIDAR profile also depends on the heights where the molecular profile is normalized to the LIDAR profile. This height has to be in a cloud free area below any clouds, but preferably close to such clouds. An additional area that is important for the cloud detection is a cloud free area above the cloud which is used to find the threshold for cloud detection. This area should be as close to the cloud as possible to have the least amount of noise in this area. If the noise is too high can it cause the threshold to become to large, and small clouds may go undetected. Both of these heights are used for the detection of the clouds in the cases, and individual molecular profiles are also used in each case. However, in the case of the climatology is the area between 12 and 14 km, which is usually above cirrus clouds, used as both the normalisation area and the threshold area. This was done because it is not possible to find an area in the lower part of the lidar signal that is cloud and aerosol free for all of the LIDAR profiles in a whole year. This means that the clouds may go undetected because the molecular signal is normalized to an area above the cloud and not below it. A normalization of the LIDAR profile to a molecular profile in the area above the cloud will also mean that the normalization is done mostly on noise and not on a real backscattered signal. Some clouds where also found to have top heights above 12 km and would therefore go undetected as areas with clouds where used to find the threshold for cloud detection. These problems lead to the conclusion that the clouds found in the climatology is less than the actual clouds in the LIDAR data. These figures have still been included in this thesis as they at least give information about some of the clouds. Measurement errors can also affect the results in this thesis. The tropospheric LIDAR at ALOMAR has experienced some difficulties, and the quality of the received signal has not been perfect for all of the

wavelengths. The depolarization ratio will suffer greatly if the quality of the signal in the parallel 532 nm channel is different from the quality of the perpendicular 532 nm channel since this variable depends on both of these channels. This could again lead to erroneous estimations of ice particle shapes.

Cases

There are many factors that may cause uncertainties and bias in Lidar data. The LIDAR system needs to be perfectly aligned to get the best data and noise sources needs to be held at a minimum. The quality of the signal is of most importance to get the best possible results. Proper normalisation heights must be found to get useful results because the programs, used in this thesis, uses a molecular fit to find the backscattered signal. This may pose a problem in some situations. The following subsection shows how well this fit have been made in the cases used in this thesis.

When calculating the height of the cloud boundaries, the threshold value is the largest error source. Noise in the data can cause problems with the threshold value. This can be improved by additional noise removal, smoothing of the profile and gluing of the Analog and photon counting profile. The latter method will improve the profiles because there are more noise in the upper ranges of the Analog mode and more noise in the lower part of the photon counting mode (more about this in section 2.4.2).

The optical depth is highly dependent of the heights calculated earlier when the Particular Integration method is used. Errors in the height calculation will therefore affect the optical depth. This can be improved by either improving the height calculation or use another method for the optical depth retrieval.

One assumption which may cause errors in the depolarization ratio is the assumption of an overall crosstalk factor of 3.2%. This value was made in the beginning of 2006 and the cases in this thesis are from the last part of 2006. The overall crosstalk factor could have changed during this time. A discussion of the overall crosstalk factor can be found in later section.

4.2.3 Validation and average plots of the cases

The plots in this section have been made by averaging the profiles with clouds used in each case. This has been done to validate how well the molecular profile fit with the data.

Case: August 15th. 2006

The upper left plot in figure 4.4(a) shows the fit between the molecular signal and the range corrected signal from the parallel, Analog 532 channel of the first cloud. The molecular signal have been normalised to the atmospheric signal between 9 and 5 km. As can be seen in this plot, there is a good fit in this area and above the cloud. However, in the lower 4 km are the fit much worse. This can also be seen in the Backscatter ratio plot. The lower denser layer should be removed by the molecular fitting, but can still be seen in the Backscatter ratio plot as a spike that reaches a Backscatter ratio value of 2. All the following plots show similar tendencies, and one possible explanation for this can be aerosols. The layer closest to the ground has the most aerosols and these will be detected by the lidar. This aerosol layer will however not be mistaken as a cloud by the program since the lower limit for cloud detection have been set above 6 km. The fit between the molecular signal and the lidar signal is best around the cloud with this normalization, and the cloud is the important part of the plot. The lower left plot is just a closer view at just the cloud. The average of the total cloud shows a Backscatter ratio value of around 2.5 at the maxima. The last plot shows the average of the depolarization ratio. At the edges of the detected cloud can the increasing noise problems be seen, but for most of the cloud is the depolarization ratio between 0.05 and 0.1. The same things can be seen for the second cloud from this day in figure 4.4(b). The lower aerosol layer is still an issue. Two spikes in the layer indicate that it is a denser aerosol layer and not just a bad fit with the molecular profile. The second cloud is much denser than the first. This can be seen from the two Backscatter ratio figures in 4.4(b). The BSR maximum reaches a value of 4 for this cloud. The depolarisation ratio, as an average, is a bit lower for this cloud. The value of the depolarization ratio is around 0.05 for the most of the cloud, except for the edges where noise becomes more pronounced.

Case: August 25th. 2006

The total cloud from the 25th of August has been averaged in figure 4.5(a). The fit with the molecular signal is not particularly good as can be seen from the RCS plot. The signal have been normalised between 5 and 3 km. A small spike in the signal under the cloud could explain a part of the bad fit. The normalisation region needs to be cloud and aerosol free to give the best possible fit, and in this case is a there possibly a small cloud or aerosol layer below the cloud. The cloud is in addition thick, approximately 5 km. This attenuates more of the lidar signal. This means that above the cloud will the difference between the detected signal and the molecular profile be quite large. The depolarization ratio is about the same as the earlier case.

Case: September 15th. 2006

The cloud in the profiles from the 15th of September case seems to be much denser in the first half than in the second half, so the two halves have here been investigated separately. The average of the first half can be seen in figure 4.6(a). The RCS plot in this figure shows

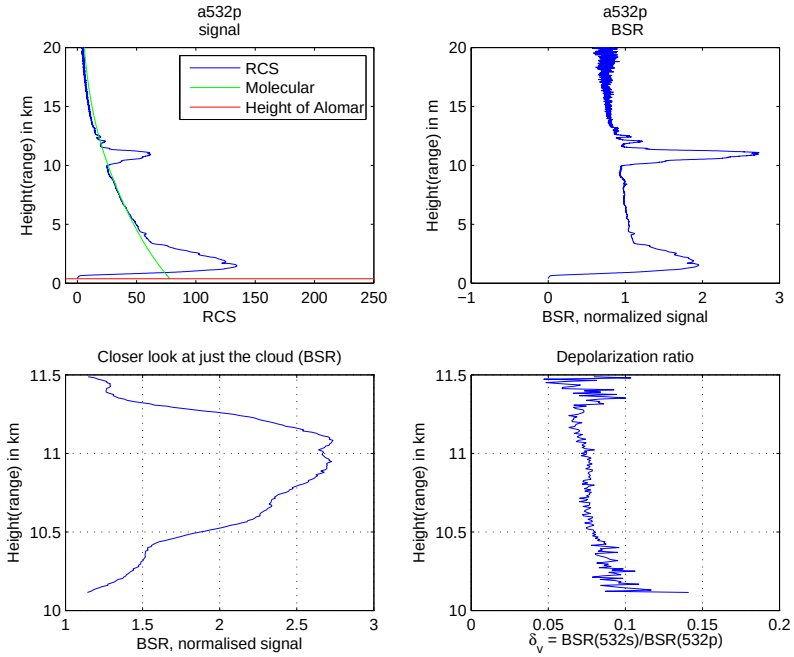

(a) Averages of all the profiles belonging to the first cloud at the 15th of August.

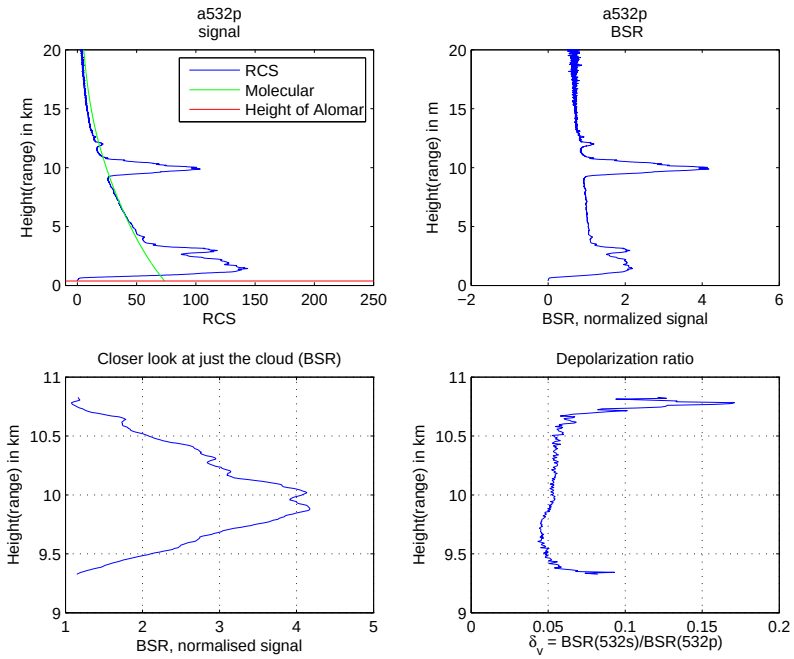

(b) Averages of all the profiles belonging to the last cloud at the 15th of August.

Figure 4.4: In both plots: The upper left figure is the averaged Range Corrected Signal(in blue) and the molecular signal(in green). The height of ALOMAR is marked with a red line. The upper left figure shows the Backscatter ratio, which is the signal normalized with the molecular profile. The lower left figure shows the same as the last figure, but is zoomed in on the cloud in the profile. The lower right figure shows the depolarization ratio.

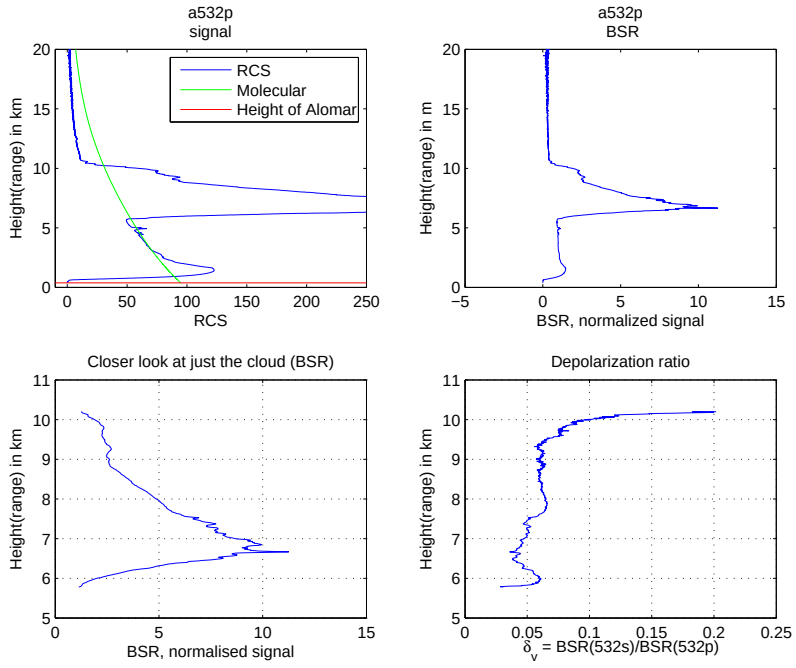

(a) Averages of all the profiles belonging to the cloud at the 25th of August.

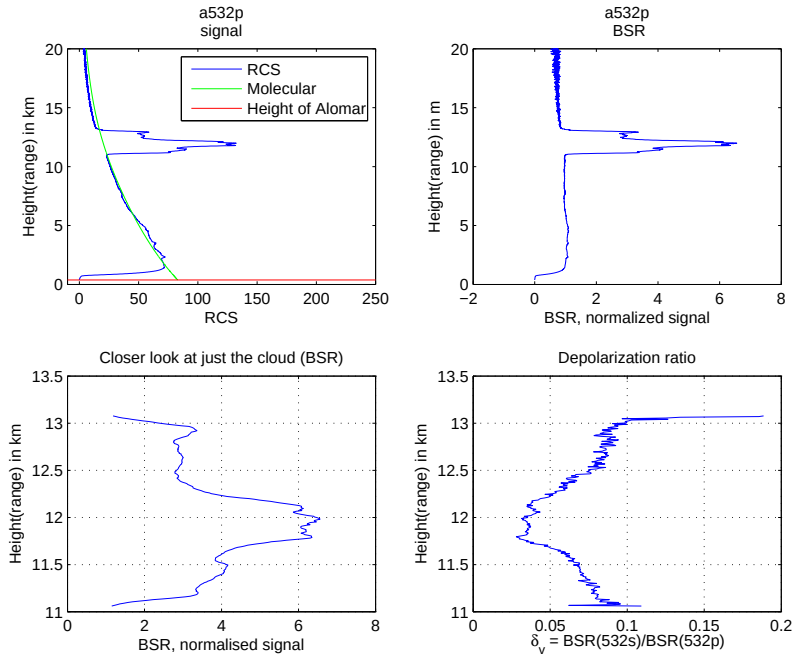

(b) Averages of all the profiles belonging to the 15th of September.

Figure 4.5: These figures show the same as figure 4.4 but for all the profiles from the 25th of August and the 15th of September. See caption of this figure on page 63 for more information.

a very good fit between the molecular profile and the lidar signal. The BSR plot has a maximum value of 10 that coincides with a minimum in the depolarization ratio. This part of the cloud would therefore consist of horizontally oriented particles.

The second, less dense part of the cloud in figure 4.6(b) also show a good molecular fit. The BSR maximum is half of the previous value and most of the cloud has a BSR value around 3. The depolarization ratio also shows that this part is less dense than the first half. The noise is more of an issue in this part as can be seen in depolarization ratio plot in figure 4.6(b). The rest of the cloud displays depolarisation ratio values close to the values of the previous part of the cloud.

The last average figure, figure 4.5(b) shows the total cloud. Shows much of the same as figure 4.6(a). The biggest difference between the two figures is that the total cloud has a lower maximum for the BSR, resulting from the lower values from the last half of the cloud. The area with low depolarization ratio and high BSR, resulting from horizontally oriented particles, is still a dominant feature in the two lower plots in figure 4.5(b)

4.2.4 The cases as a total

The three cases presented here are the three best cases from a set of six cases. These where chosen because they had the best fit between the molecular profile and the LIDAR signal of the six cases chosen at the beginning. A good fit between molecular profile and the LIDAR signal makes the detection of the cloud top and cloud base more reliable. The three other cases were excluded from this thesis because of noise issues and bad fit between the molecular profile and the LIDAR signal. The preliminary analysis of these other cases can be found in appendix C.

4.2.5 The effect of changing the overall crosstalk factor

The data from the 15th of September have been chosen to test the effects of changing the overall crosstalk factor k. The crosstalk factor can change over time, and two values was given for this factor in Alomar (2006b), $k \cong 3.2\%$ from February 2006 and $k \cong 4.7\%$ from October 2005. The former has been used throughout this thesis. This test been made to see how much a change in the value of k will affect the calculated depolarization ratio. The connection between this factor and the depolarization ratio can be found in section 2.3.2.

All the figures in this section are made as an average over the Lidar files from 11:50 to 13:16 from the 15th of September. The Analog, parallel 532 channel have been used, and the same normalisation heights[3] and cirrus limits[4] was used for all the plots.

Plots have been made for the two values of k given in Alomar (2006b). Plots have also been made for half ($k \cong 1.6\%$) and double ($k \cong 6.4\%$) of the February 2006 value. A last plot have been made for $k \cong 9.9\%$ just to see what happens when the value is increased even further.

It can be seen from comparing figure 4.7(a) and figure 4.7(b) that for the higher value of k, figure 4.7(b) is also the depolarization ratio slightly higher than for the lower value of k(figure4.7(a)). As an example is the depolarization ratio 0.08 for k=3.2% at 12.5 km. The depolarization ratio value is 0.12 in the same height in the k=4.7% figure. The shape of the depolarization ratio profile is almost the same in both figures. It is however not

[3]Normalization heights: 9000m/5000m
[4]Cirrus limits: 15000m/6000m

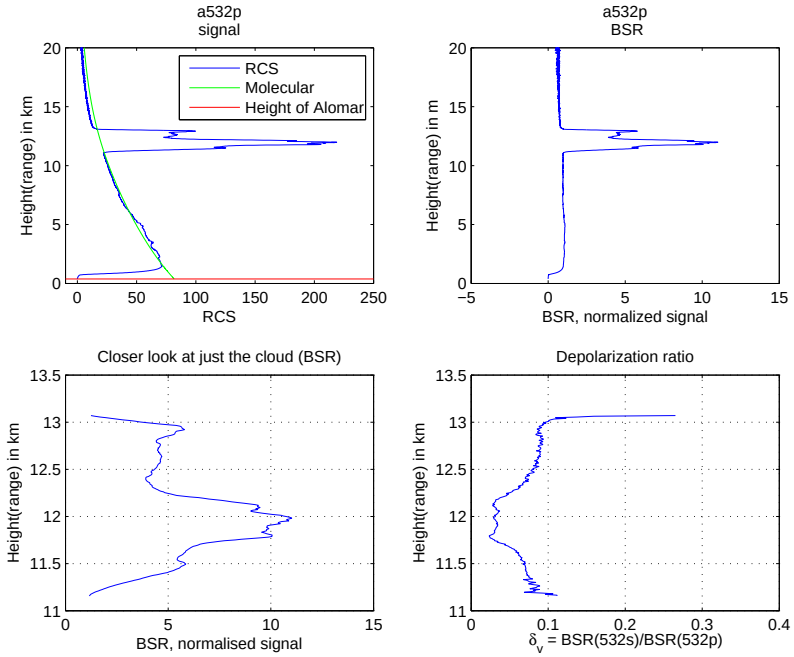

(a) Averages of all the profiles belonging to the first half of the 15th of September.

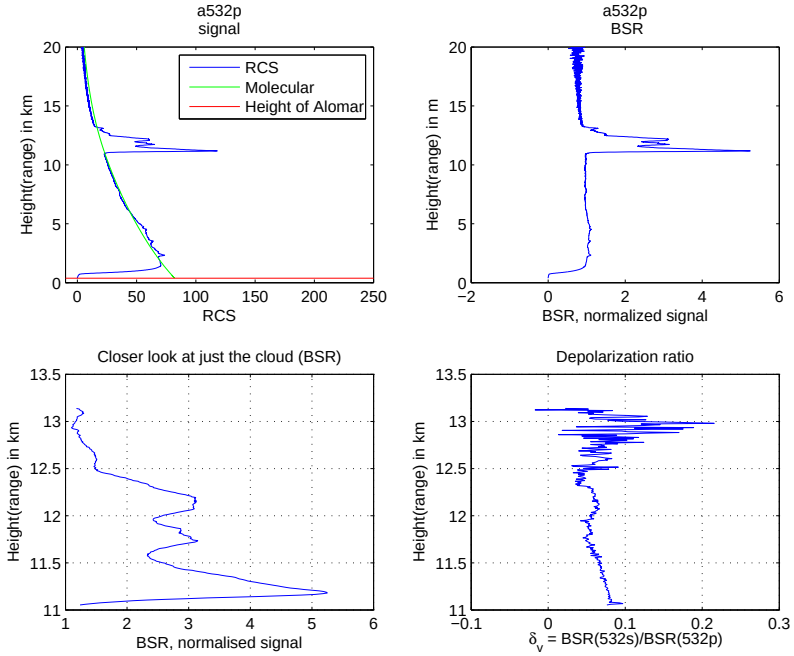

(b) Averages of all the profiles belonging to the second half of the 15th of September

Figure 4.6: These figures show the same as figure 4.4 but for the 15th of September. See caption of this figure on page 63 for more information.

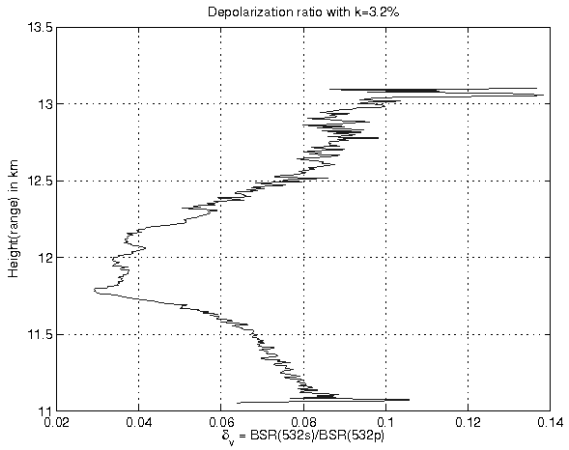

(a) k=3.2%

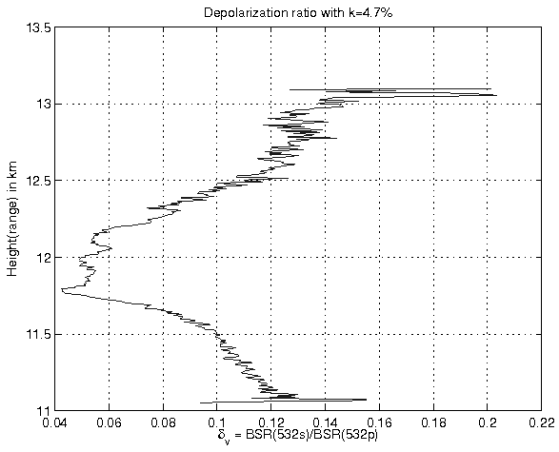

(b) k=4.7%

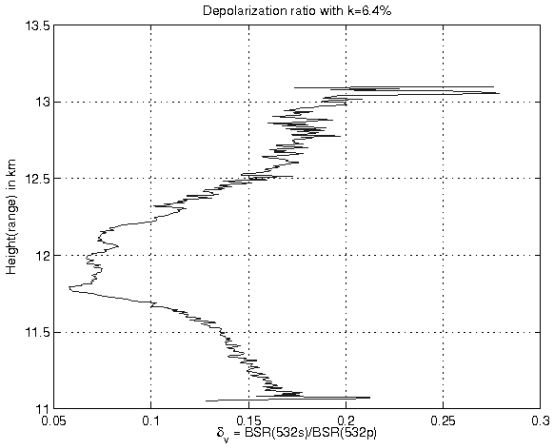

(c) k=6.4%

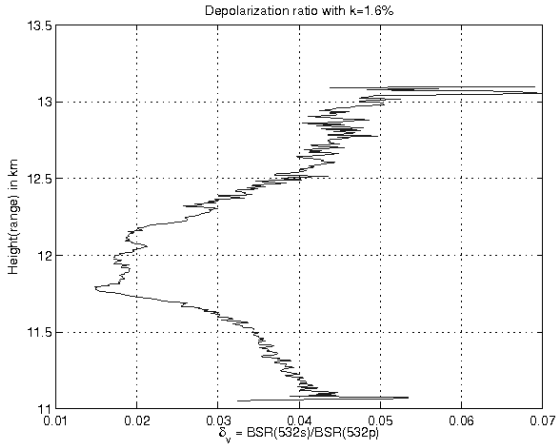

(d) k=1.6%

Figure 4.7: Depolarization ratios for the cloud with the k values from October 2005(a),February 2006(b),double of the k-value from February 2006(c) and half of the k value from February 2006(d)

exactly the same as the depolarization ratio does not change equally at all altitudes. One example is; at 12 km is the change in depolarization ratio only about 0.015, but at 12.5 km is the change almost 0.04. The changes are very small when the k value is changed from 3.2% to 4.7% and the conclusions about the shape of the ice crystals do not change in this case.

The next two figures shows what happens if the k value is half or double of the value from February 2006. In the first case, which is shown in figure 4.7(d), the value of the depolarization ratio will be lower than for the value of k that have been used. At 12.5 km is the depolarization value approximately 0.04, and at 12 km approximately 0.019. The k=6.4% case also show similar changes. The depolarization ratio values are a bit larger than for the earlier k-values (0.15 at 12.5 km and 0.06 at 12 km) but do not show any large variations.

The last question to answer is; what happens when the k-value is much higher than in the previous plots? Will this change the depolarization ratio enough to influence conclusion about the shape of the ice crystals? The last figure, figure 4.8, shows a depolarization ratio which is calculated with an overall crosstalk factor of 9.9%, which is much larger than in the earlier cases. The 12 km and 12.5 km values of the depolarization ratio are in this case approximately 0.1 and 0.25 respectively. Because the depolarization ratio reaches above 0.25 could a part of this cloud consist of irregular or intermediate crystals (from table 2.3).

This shows that value of the k factor can influence the conclusions about the shape of the ice crystals. However, the overall crosstalk factor must become quite large before the conclusions are altered. The k factor does not have that much of an influence on the shapes deducted from the depolarization ratio if the value of the overall crosstalk factor does not change much more than to the double of the February 2006 value, as in figure 4.7(c), or to the half, as in figure 4.7(d). Whether or not the ice crystals are horizontally oriented is also not influenced by the k-factor. The area with max BSR signal is connected with the area where the depolarization ratio is closest to zero in all the figures in this section.

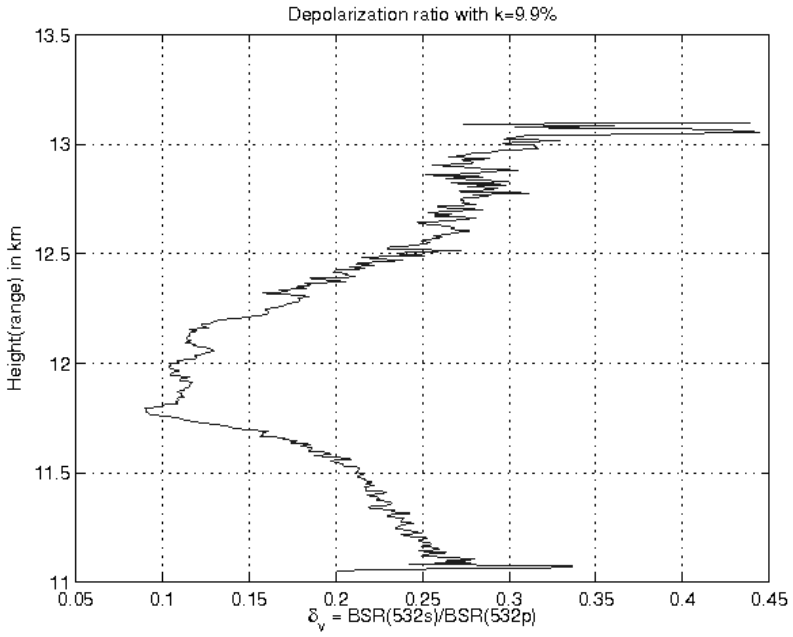

Figure 4.8: Calculated depolarization ratio when the k is increased to 9.9%

4.3 Case: 15 August 2006

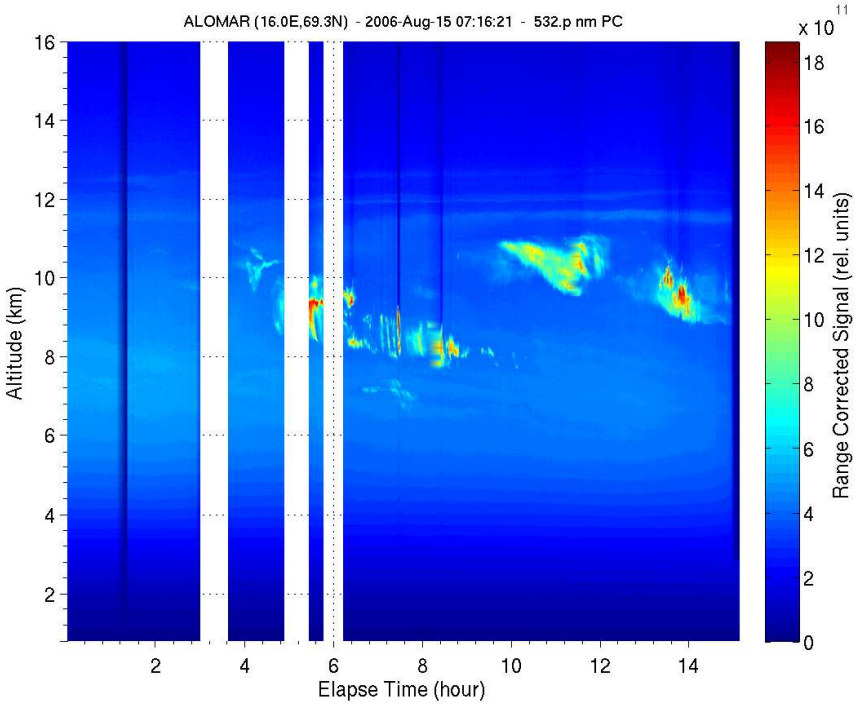

Figure 4.9: Quickplot of all measurements from the 15th of August.

The total measurements from the ALOMAR LIDAR at this day spans around 15 hours from 07:16 in the morning until 22:24 in the evening. A total number of six sets of atmospheric measurements were taken during this day. Noise measurements were made in between these atmospheric measurements. Figure 4.9 gives a plot for the range corrected signal for all of these measurements. The first sets of measurements display a relatively clear atmosphere, but clouds appear after approximately four hours. The first cloud patches that appear are relatively small and mostly obstructed the white bands during noise measurements. Two other clouds, that seem a bit denser than the first couple of clouds, appear after 10 hours. The measurements were made at daytime and in the summer, so there may be some issues with noise from sunlight in the data. The fit between the molecular signal and the LIDAR signal was found, in section 4.2.3, to be quite good around the cloud. The RCS values are between 0 and $5(*10^{11})$ for the clear sky and 6 to $16(*10^{11})$ for the clouds. The height of these clouds and the fact that the LIDAR can penetrate their thickness suggests that these are cirrus clouds. They are just small patches and do not seem to be part of any cloud layer structure as the cirrocumulus or cirrostratus. The two larger cloud patches that appeared during the last 4 to 5 hours will further on be investigated.

4.3.1 Cloud heights

Figure 4.10 is a plot from the tropospheric LIDAR of just the profiles with these two clouds, and the calculated cloud top and base are added on top of this. The quick plot is made with the 532 nm channel, but the heights are found from the 1064 nm channel because this

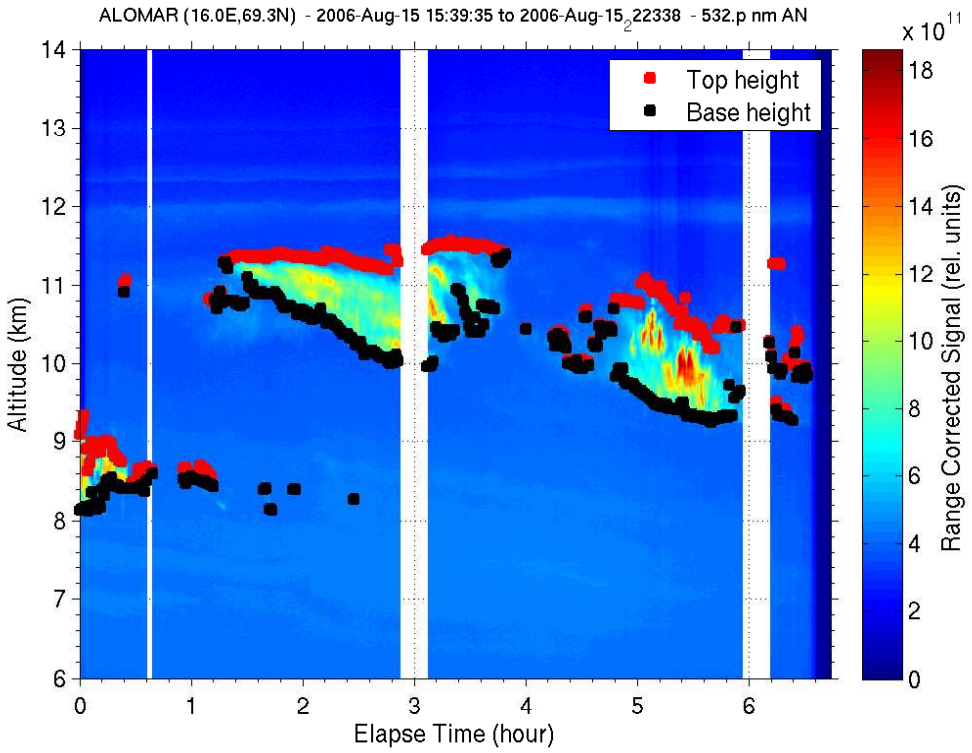

Figure 4.10: Detected cloud top and base altitudes on the 15th of August 2006. The upper cloud layer top is marked in red and the lower cloud base is marked in black. The heights are calculated in the Analog 1064 nm channel but the Quickplot is made with the Analog, parallel 532 nm channel.

channel gave better results with the height calculation program. A part of one of the lower earlier clouds can also be seen in the beginning of figure 4.10. The white stripes in the plots are short stops in the measurements that were made to make noise measurements. The bases calculated of these two clouds are just above 10 km, and the calculated base heights usually coincide well with the clouds seen in the Quickplot. The cloud base is set much lower than the main cloud in some of the profiles around 2 hours into the measurements. This is because the cloud base retrieved from the program will be the base of the lowest cloud layer. This is done because clouds often consist of several layers. However, the lowest base found in these profiles is the base heights of small remnants of the earlier cloud. The cloud tops are around 12 km for the main two clouds, and these seem to fit well except for some of the last profiles. It also looks like some of the cloud tops found is a little bit higher than the actual cloud tops. The cloud top and base of the second cloud do not seem to fit as well as the heights of the first cloud. The fit is however not particularly bad. Cloud detection can also be effected by the altitudes to which the molecular profiles are fitted(see section 4.2.2 for more information).

The temperature within the cloud is a first measure of whether or not this is an ice cloud. Figure 4.11 is a radiosonde profile form the Bodø radiosonde station that was made at 12:00 on the 15th August. This is not the exact temperature profile for the ALOMAR data since Bodø is some distance away from Andøya. It is however close enough to be used as an approximation. The black, thick line to the right in the figure is the

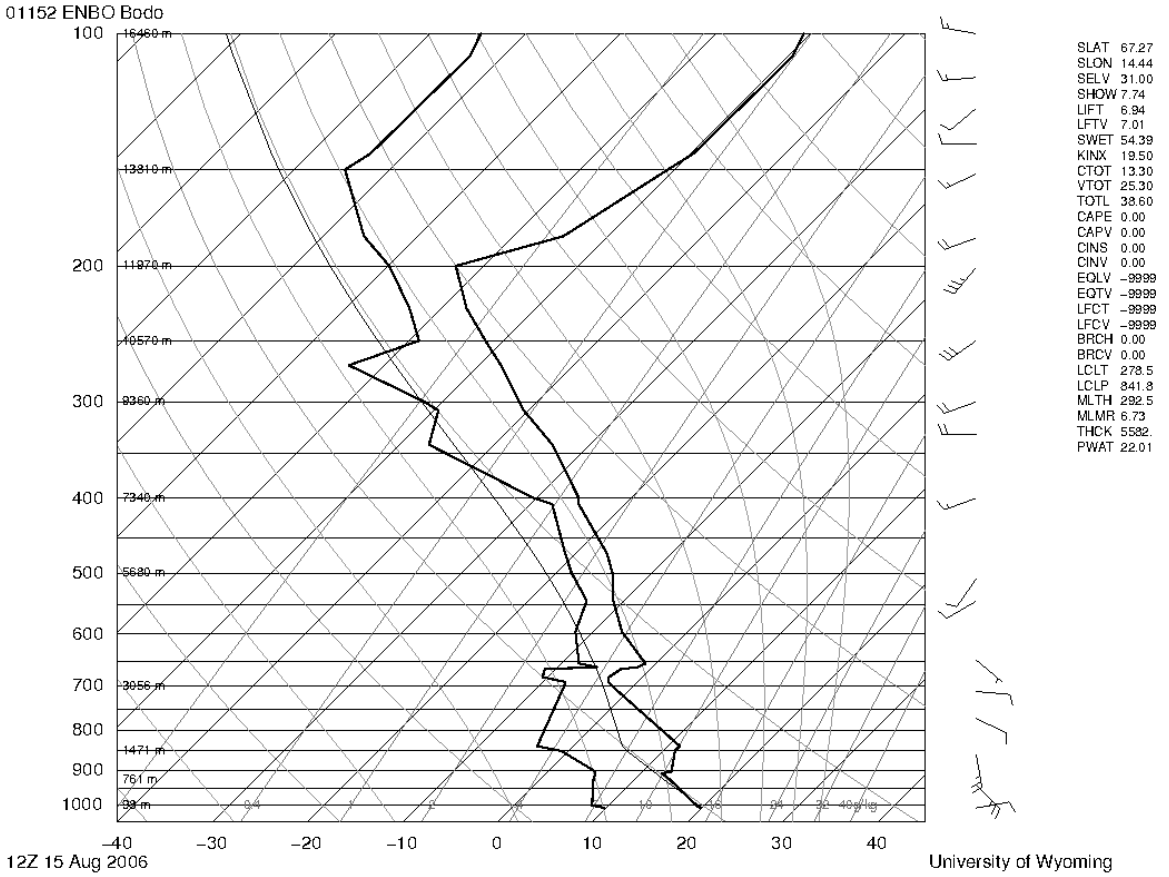

Figure 4.11: Skew-T diagram from the Bodø radiosonde. This profile is from the 15th of August at 1200. The diagram shows the temperature profile(right) and the dew point temperature(left). The diagram also shows the wind speed and direction, but this is not used in this thesis.

temperature line, and this line shows that the temperature decreases from around $0°C$ to approximately $-60°C$ between approximately 3.5 km(750 mb) and 12 km(200 mb). From the dew point temperature, the black, thick line to the left in the figure, can it be seen that in the troposphere is the area with the most moisture at 3-7 km. The driest area in the troposphere is between 8 and 10 km. However, it is not particularly dry in this area, the dew point and the temperature is still quite close, it is just dryer than the lower areas. The tropopause is located around 12 km as can be seen from the temperature profile. The clouds investigated in this case are located just below this height, at 9.5-11.5 km. The temperature in the height range of the clouds is between $-30°C$ and $-40°C$. The presence of supercooled water droplets is highly unlikely in this temperature range, and the clouds can be assumed to be pure ice clouds. Another way to check whether or not this is an ice cloud is to look at the depolarization ratio. A depolarization ratio above zero would indicate presence of ice.

CALIPSO data

The CALIPSO satellite made two close passes by ALOMAR during this day. One of these passes went by around 02:30 and the other passed by around 10:30. The closest position in both time and space was calculated and the result can be seen in table 4.4. There are a few problems with comparing the CALIPSO data with the ALOMAR data. First of all, the measurements will not be taken on the same place and time. The calculations with the CALIPSO data use the closest position in space, but this is not necessarily very close in time. The closest position in space has been used in most of the cases in this thesis, as the closest position in time often is to far away from ALOMAR to give a proper comparison.

File	CAL_LID_L2_01kmCLay-Prov-V2-01. 2006-08-15T09-53-02ZD.hdf	
	Closest in time	closest in space
time	10:45:08	10:33:50
latitude	65.45N	70.49N
longitude	-117.01V	23.46V
distance (km)	4646.18 km	332.43 km
time difference (s)	32994 s	33672 s
time difference (h)	9.17 h	9.35 h
File	CAL_LID_L2_01kmCLay-Prov-V2-01. 2006-08-15T01-38-36ZD.hdf	
	Closest in time	closest in space
time	02:30:56	02:29:24
latitude	64.65N	69.91N
longitude	5.88V	11.61V
distance (km)	655.79 km	194.54 km
time difference (s)	62646 s	62738 s
time difference (h)	17.40 h	17.42 h

Table 4.4: This table gives the time, latitude and longitude of the profile closest to the ALOMAR location, and the profile closest to the time of the ALOMAR data used in this case. The middle profile in the ALOMAR data is used for the last calculation. The calculated differences in time, both in seconds, hours, and distance are also given for both possible files.

From the results in table 4.4 can it be seen that the CALIPSO measurement from 02:30 is closest in space, but this measurement is made more than a day later than the ALOMAR measurement. The second (10:30) measurement was made closer in time, only 9 hours difference, but the distance between ALOMAR and the closest measurement is quite large. When viewing the data it was found that the 02:30 measurements do not display any cirrus, so the 10:30 measurements have been used for the following calculations and plots.

A close-up of the path the satellite followed during the chosen measurements used in this case is displayed in figure 4.12(a). This can be compared with the map in figure 3.1 in section 3.1 to see how close the satellite passed by ALOMAR. What was found in table 4.4 can then be seen in this figure. The satellite passes by the ALOMAR site within a reasonable distance. This distance is however far enough from the ALOMAR location to

possibly complicate the comparison, and results from such comparisons should be used with caution.

Figure 4.12(b) displays the clouds found in the 147 closest CALIPSO profiles. These profiles all lie within a 500 km range from ALOMAR. Two possible cirrus clouds, displayed in red, can be seen in the figure. The location of the first of these is close to ALOMAR at approximately $70°N$. A lower feature resides below 2 km, which also can be found in many of the other cases. This could be a dense aerosol layer that has been wrongly classified as cloud. The cloud layer product from CALIPSO, that is used to make this plot, should only include clouds. But the discrimination between clouds and aerosols by the CALIPSO algorithms still has some problems, as described in section 4.1.2, and some dense aerosol layers may be classified as clouds. However, the interesting clouds are not this layer, but the two clouds that could be cirrus clouds. They both reside at cirrus height, well above 6 km and below the tropopause. These heights also fit well with the heights of the clouds observed at ALOMAR. The next thing to investigate is therefore the temperature of these cloud layers. The temperature from these layers is also given in the CALIPSO data, and the question is now if these temperatures coincide with the radiosonde temperature or not. The temperatures for the two interesting clouds can be found in figure 4.12(c). The temperature of the cloud closest to ALOMAR is between $-30°C$ and $-40°C$, and its height is around 8 km. This fits with the temperature of the clouds in the ALOMAR data that was found from the radiosonde data in figure 4.11 . There is therefore a possibility that the cloud contain some supercooled water, however it is highly unlikely when the temperature is that low. The second cloud has temperatures well below the homogenous freezing threshold, between $-45°C$ and $-50°C$. This second cloud does reside a bit higher, at approximately 10 km, than the first one detected by the CALIPSO satellite in this area. This cloud is therefore closer to the height of the cloud layers detected by the ALOMAR LIDAR. The temperature difference between the two CALIPSO clouds could also be partially caused by the latitude difference between the two clouds, the second cloud is 3° further north than the first one.

4.3.2 Optical depth

The last figure, figure 4.13, from the ALOMAR data shows the optical depths of the clouds. The blue line in the plot is the optical depth, which is calculated with the data from the 1064 nm channel. The optical depth is calculated with the particular integration method with an effective LIDAR ratio of 20. The black line in the plot is the subvisible cirrus cloud limit, optical depth = 0.03. The first cloud that occurs during the two first hours of measurement is quite thin at the beginning, around 0.2 which would indicate thin cirrus(optical depth =0.03-0.3 from table 2.4). However, the optical depth of this cloud reaches 0.04(Opaque: optical depth=0.3-3.0) when three hours have passed. The second cloud is visible for a full hour of the measurements and the optical depth reaches as high as 0.9. A large part of this cloud has optical depths above 0.3, so this cloud is mostly an opaque cirrus cloud. This fits with the fact that this cloud seem to scatter more light in figure 4.10. The remnants of the earlier cloud that can be seen in the beginning of figure 4.10 are partly subvisible and only marginally above the subvisible threshold in comparison with the other clouds. The edges of the two main clouds are also subvisible.

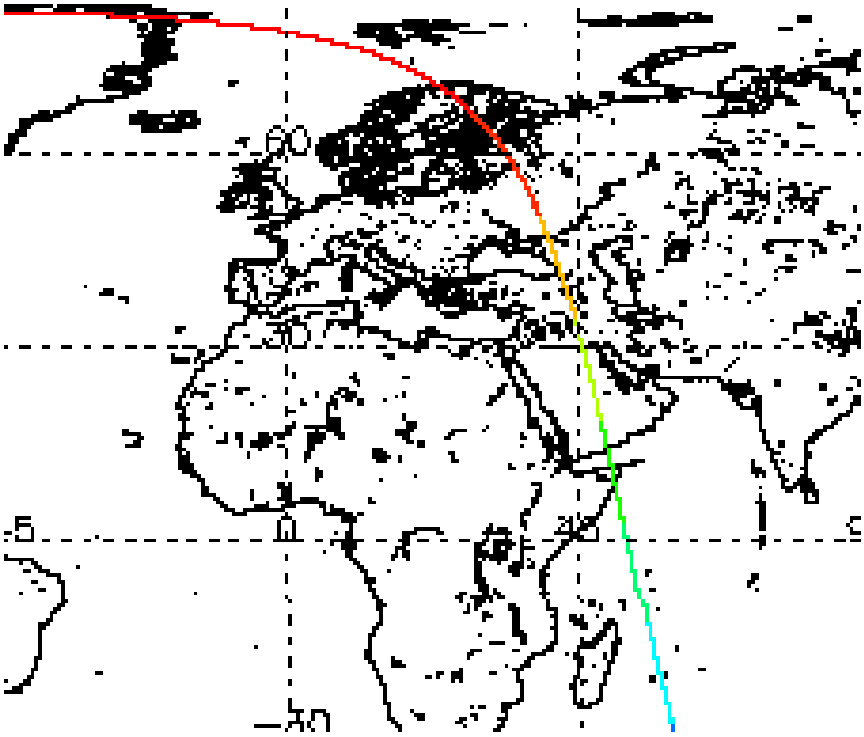

(a) Geolocated path of the CALIPSO satellite during the measurement used in this case

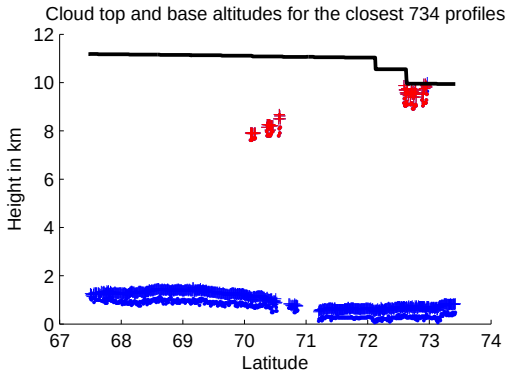

(b) Clouds found in the closest CALIPSO profiles. Red markers are the cloud boundaries of probable cirrus clouds(altitudes between 6000m and tropopause height) blue markers are other features. Black line indicates the tropopause height.

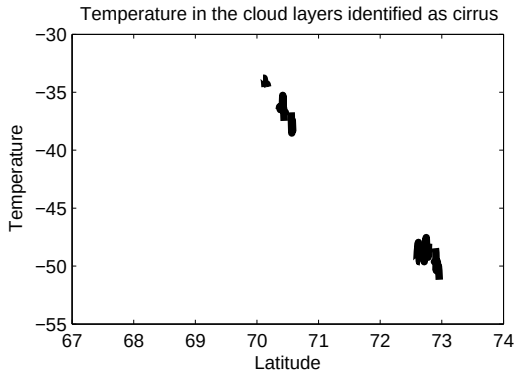

(c) Temperature for the clouds in The CALIPSO data

Figure 4.12: CALIPSO results of the 15 August case

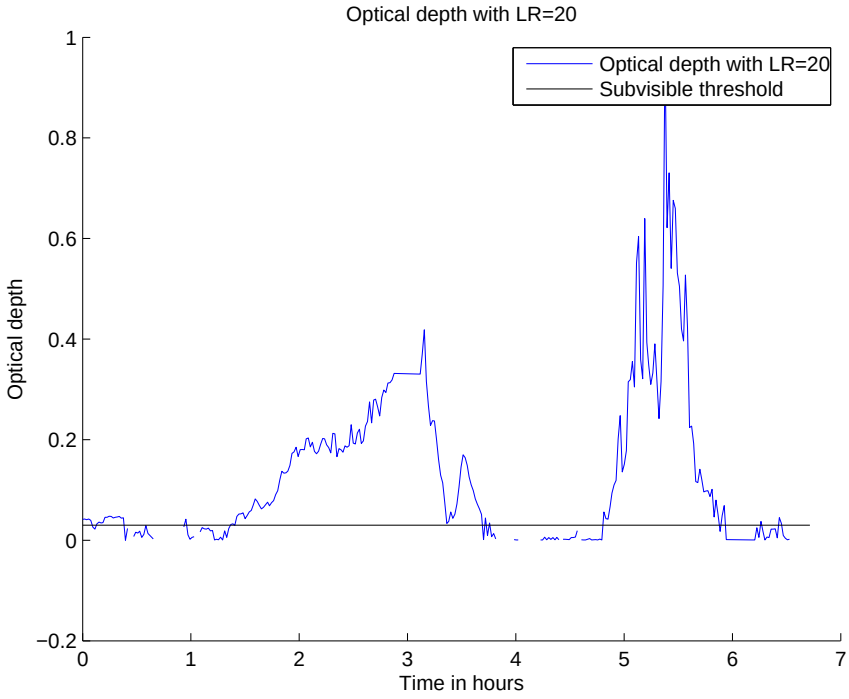

Figure 4.13: Optical depth of cloud detected on the 15th of August 2006. The blue line is the optical depth calculated with the 1064 nm channel and an effective lidar ratio of 20. The black line is the limit for the subvisible clouds; optical depth = 0.03. The Particular integration method has been used to find the optical depth.

4.3.3 Depolarization ratio

The depolarization ratio is displayed in the figure 4.14. Both clouds have depolarization ratio values below 0.2, so there are three possible conclusions. The clouds could consist of ice crystals formed as plates, super cooled water droplets or ice crystals that are horizontally aligned. These clouds have temperatures that indicate that they are ice clouds so supercooled water droplets should not occur in this case. The ice crystals will probably be plate formed when the depolarization ratio is below 0.25(see section: 2.3.2). This is the case for these two clouds, but the depolarization ratio is very close to zero. To decide whether one can positively identify this cloud as consisting of plates or possibly other types of ice crystals, one needs to look at the intensity of the backscattered signal in comparison to the depolarization ratio. The ice crystals will be horizontally aligned if there is a high intensity of the backscattered signal in addition to zero or close to zero depolarization ratios It not possible to discriminate between plates and columns when the crystals are horizontally oriented. Both of these shape types will lead to zero depolarization and high backscattering when horizontally oriented. Intermediate or irregular ice crystals, on the other hand, will not become horizontally oriented. There is no evidence of horizontally aligned ice crystals because the depolarization ratio is close to zero for all of the cloud and not just for the areas with high backscattering. The two clouds have several areas with a higher backscattering than the rest of the cloud as can be seen from the range corrected signal in figure4.10. These areas can not be found in figure 4.14 which shows the depolarization ratio. The calculated depolarization ratio is much less clear in this case than in the

other cases used, and it seems to be more influenced by noise. How much confidence the depolarization ratios from this thesis have is not easily said as there is nothing to compare with. There is therefore a possibility that figure 4.14 is not completely correct.

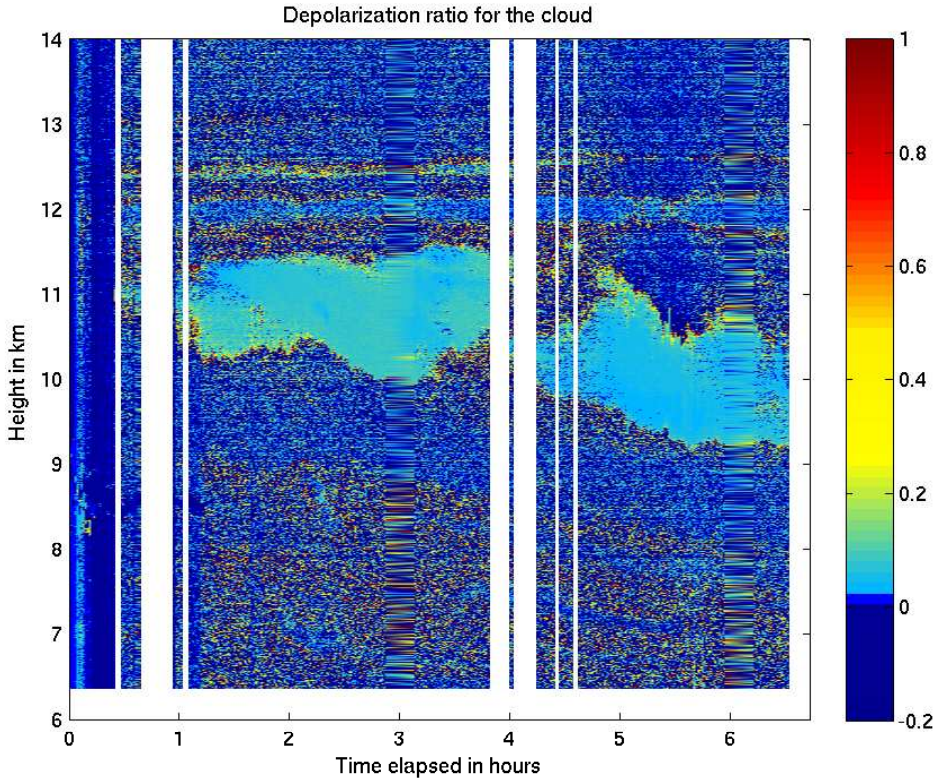

Figure 4.14: Depolarization ratio for the clouds detected on the 15th of August 2006. Dark blue indicates depolarization ratio of 0 or less. Noise is visible in the clear atmosphere around the cloud.

4.3.4 The weather situation on the 15th of August 2006

The following section shows the weather situation around the time the measurements from this case was made. Figure 4.15(a) shows a DNMI weather analysis chart from 18:00 at this date. From this chart can it be seen that the weather situation during this day is dominated by a system of two lows over the southern part of Scandinavia. Several fronts are connected with these lows, both occluded fronts that lie south and west of the lows, and cold fronts that lie north and east of these lows. Parts of the north Atlantic occluded front from the 18:00-analysis has changed into a warm front at the latest analysis, and a few troughts have been drawn in connection with the cold front.

The second DNMI chart, 4.15(b) from the 15th of August include observations. The observed clouds at Andøya at 18:00 during this day can be seen in figure 4.15(b), they where hook shaped, and maybe thickening, cirrus clouds. These are probably connected with the cold front system further south. Observations closer to the fronts display mostly altocumulus type clouds and more cloud cover than above Andøya.

Figure 4.16 shows a satellite image taken with the 11.5-12.5 μm channel of the AVHRR instrument onboard the NOAA satellite. This satellite image was taken at 20:19 which is

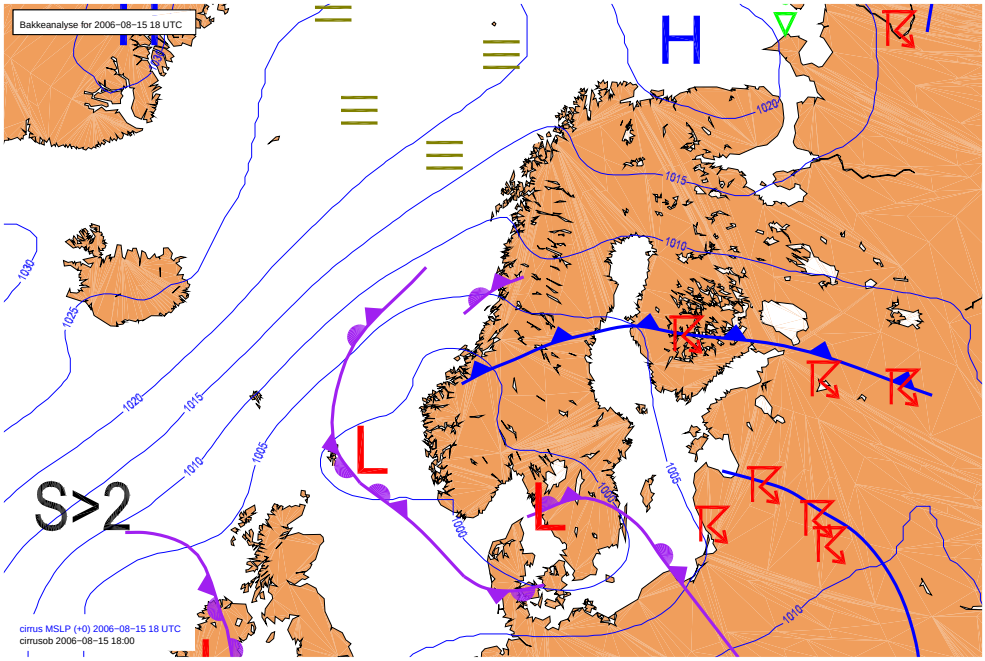

(a) Weather analysis from DNMI on the 15th. of August (18:00)

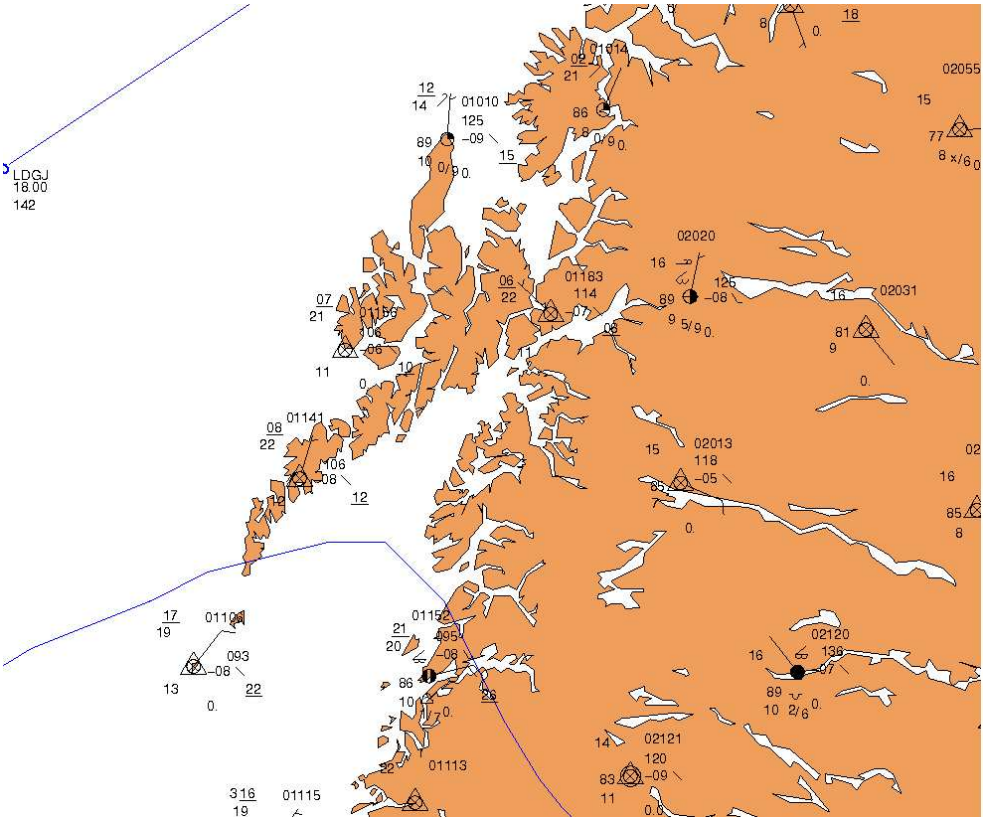

(b) Weather analysis with synop observations from DNMI on the 15th. of August (18:00)

Figure 4.15: Weather charts from DNMI from the 15th of August 2006 (18:00)

between the times of the two analyses from DNMI. Cloud features connected to the two lows that can be seen in the weather chart in figure 4.15(a) are also seen clearly in the satellite image. The low above the southern part of Sweden and its accompanied occluded front can be seen in the satellite image as very white hook shaped cloud feature with its center just above southern Sweden. The other low, which in figure 4.15(a) is situated off the south-west coast of Norway, is even more distinct in the satellite image. The warm front in connection to this low is followed by a massive cloud cover off the west coast of Norway. From the satellite image in figure 4.16 can it be seen that this cloud cover stretches from the northern parts of Great Britain up to the sea outside the northern parts of Norway. This low is also connected to a cold front that stretches across Scandinavia and Finland into Russia. The cloud cover associated with this front is also very large. The clouds seen in the ALOMAR LIDAR data is connected to the clouds associated with these two fronts. There is an extensive cloud layer connected to the cold front at the main land of Norway closest to ALOMAR. This can also be seen from the observations in figure 4.15(b), as several of the observations in the main land show that most of the sky is covered with clouds and that these are mostly altocumulus type clouds. From the satellite image can it be seen that at Andøya and the sea around this island is there less clouds as this is in the cloud 'gap' between the cloud features associated with the warm front, and the cloud features associated with the cold front. The small cloud patches that can be seen seem to be consistent with the small patches found in the ALOMAR LIDAR data. The clouds found in the CALIPSO data are also from this area, only a bit further north than the ALOMAR clouds.

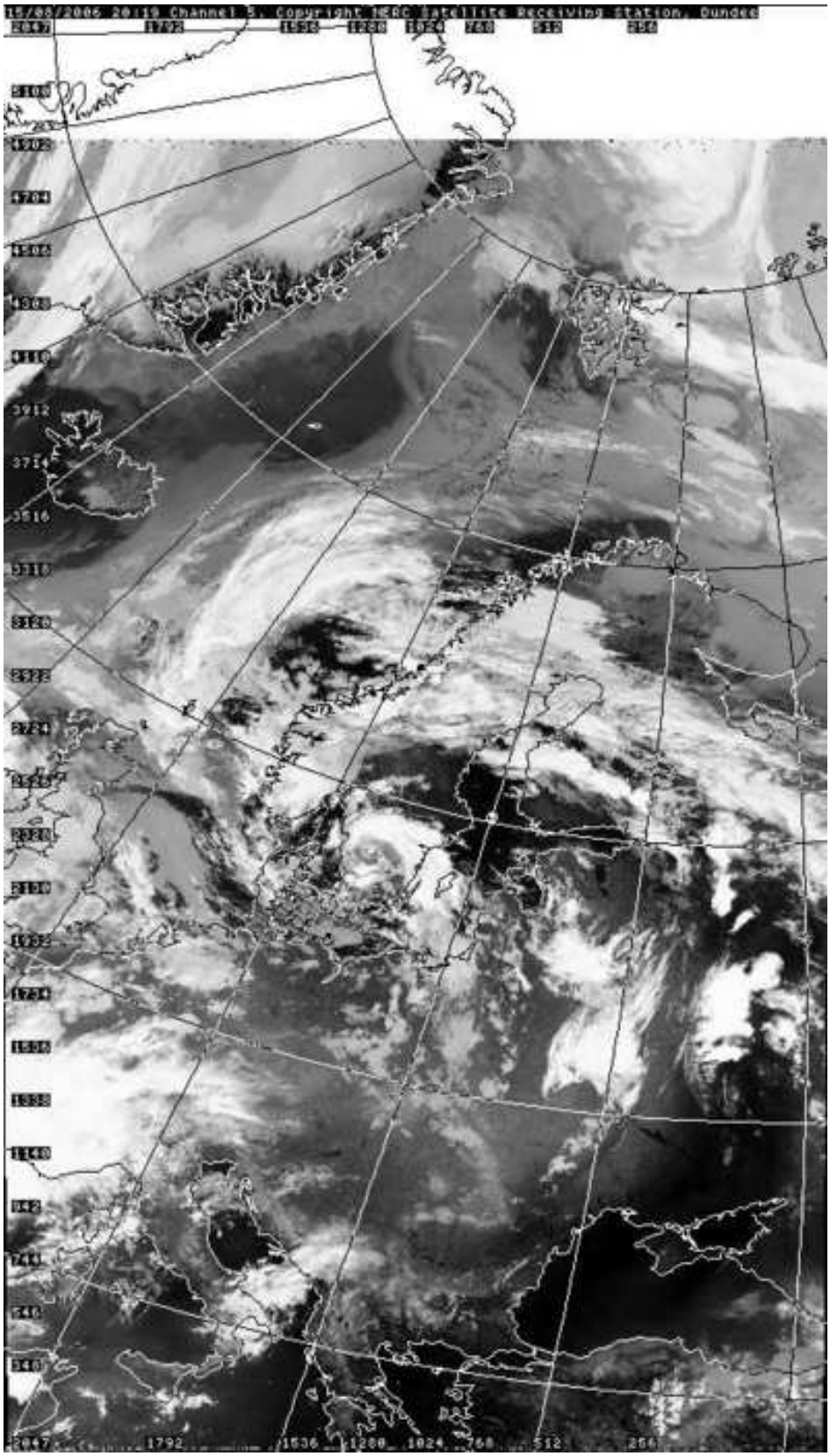

Figure 4.16: Satellite image from NOAA AVHRR at 20:19 on the 15th of August 2006. This image is from the thermal infrared channel at 11.5-12.5 μm.

4.4 25 August 2006

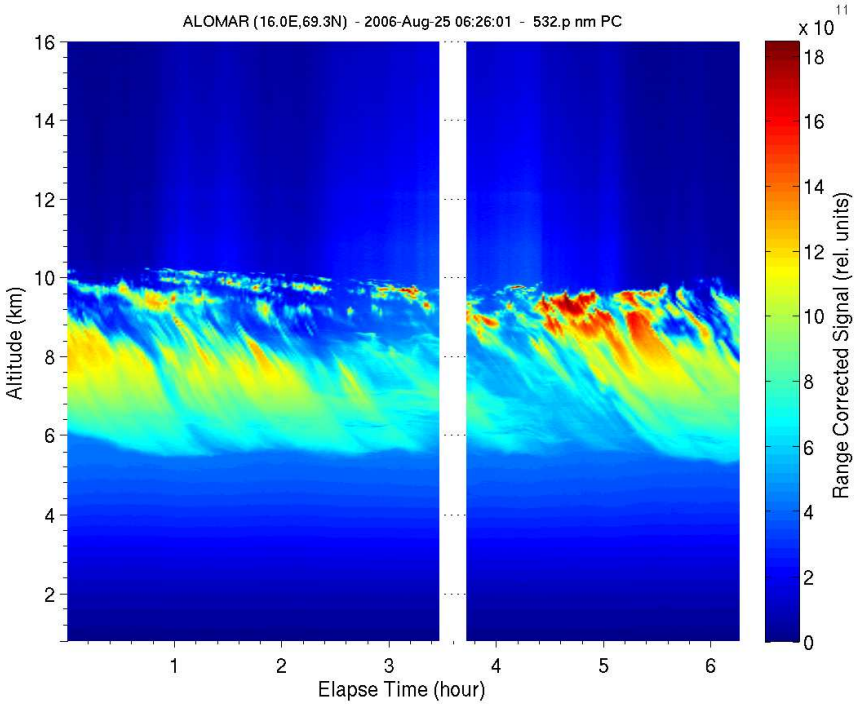

Figure 4.17: Quickplot of all measurements made on the 25th of August 2006

Two sets of measurements were made at the 25th of August 2006 and both of these show a cloud layer that extends from approximately 6 km up to about 10 km. This thick cloud can be seen in figure 4.17 which show approximately 6 hours of measurements. The number of measurement hours found in August seen in figure 4.2(b) is only around 4 hours because of the difficulties with detecting cirrus clouds automatically for a whole year that was pointed out in section 4.2.2. However, the large height difference between the median top and base cloud height found in figure 4.2(b) can be explained by the large cloud in this case. More of the cloud from the 25th of August was found by the climatology program, than any other cloud from August. This cloud has therefore a large influence on the August part of the climatology. The cloud seems to consist of small patches at the top and further down the cloud layer is more uniform and the cloud seems more tail-like. It almost looks as the cloud has fall streaks. The RCS is quite strong in the beginning of these fall streaks, approximately around 8 km, but decrease when moving towards the base of the cloud. The RCS values are from 0 to $4(*10^{11})$ for the clear atmosphere and from 6 to $17(*10^{11})$ for the clouds.

These measurements are daytime measurements in the summer, as for the first case, which may cause some extra noise problems because of sunlight. The measurements span approximately six hours and it is during the last three hours that the densest clouds with the highest RCS appear. A possible explanation of these clouds are that they are virga type cirrus moving slowly over the ALOMAR observatory, and that the uniform part of the cloud contains large ice particles that fall below the cloud and are dragged towards the left in figure 4.17 by lower winds. The RCS is weakened toward the cloud base because the

ice particles are sublimated as they fall into the lower, and warmer air. One can say that the cloud seen here consists of two parts. The first is the main cloud which is the top part in the figure, the cloud particles are formed in this part of the cloud. The second part is the fall streaks. These are ice particles that have grown big enough to fall as precipitation from the main part and sublimate before they reach the ground. The next figures consider the full set of measurements.

4.4.1 Cloud heights

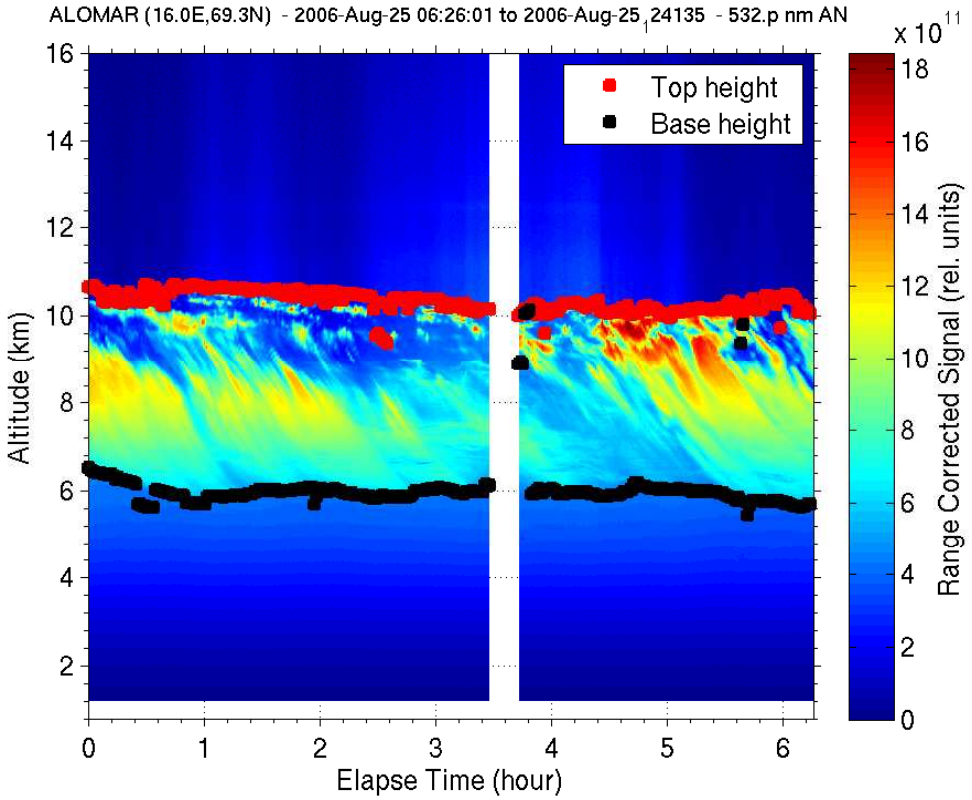

Figure 4.18: Detected cloud top and base altitudes 25 August 2006. The heights were found from the 1064 nm channel, the Quickplot is made from the parallel 532 nm channel. The upper cloud top found is marked with red and the lower cloud base found is marked in black.

Figure 4.18 displays the calculated top and base heights for this cloud on top of the Quickplot of the cloud. As seen by the figure, the calculation of the cloud top is fairly good. There are only a few profiles around 2.5 hours into measurements that seem too be a bit low. The top height is not necessarily wrongly calculated for these profiles. This could be caused by patches of clean air between cloud features at the height of the main clouds, and ice particles blowing into the view of the LIDAR beneath this height. The base height also shows a good fit with the bottom of the fall streaks. There are only a few profiles where the base is a little bit low, and a couple of profiles in the last set of measurements that are much higher than the rest. It seems that the in the case of the base heights that was found higher than in the rest of the profiles, is the base height found the base of the

main cloud and not the fall streaks as in the other profiles. An explanation for this could be that for these profiles were the fall streaks considered as noise by the program. This can happen if the cloud is thin enough. This will not pose a problem in the later discussion as there are only a few profiles where the base height is too height.

The temperature profile from the Bodø radiosonde measurement from this day can be seen in figure 4.19. It can be seen in this figure that the temperature, the thick, black line to the right, is gradually decreasing from $0°C$ at approximately 3 km (750 mb) down to approximately $-55°C$ at 11 km (350 mb). The tropopause height can also be found at approximately 11 km. The dew point and the temperature lines are closest between approximately 4 and 10 km, which indicate that this area is moist. The cloud investigated in this case can also be found in this height area. The temperature at the cloud top height, at 10.5 km, is cold enough to have only ice present. It is as cold as $-55°C$. But the temperature is as high as $-15°C$ at the base height at 5.5 km, and at this temperature could supercooled water droplets be present. For this cloud it is only necessary that the main part of the cloud has temperatures that would give only ice crystals when the cloud. The ice particles are formed in the higher, colder regions of the cloud and fall downward to form the fall streaks. The ice particles in the fall streaks are therefore already ice and supercooled water poses no problem in this area. Since the main cloud is ice will the rest of the cloud be ice too.

CALIPSO data

The CALIPSO satellite made two close passes during this day. Both were daylight measurements. The first of these two passes was around 03:00, while the other passing was around 11:00. Table 4.5 displays the calculations regarding the closest position of the CALIPSO satellite from these two sets of measurement. The closest positions in time and space are very similar in the 03:00 measurement. They both are made only six and a half hour from when the ALOMAR measurements where made. But both the closest position in time and the closest position in space are above the 500 km limit that has been set, even though the closest position in space only is around 1 km above this limit. The second passing is more promising. Both the closest profile in time and in space where made less than 2 hours before the middle ALOMAR profile from this day. This means that some of the measurements where made at the same time. The closest position in space was in addition less than 9 km from the ALOMAR site. This makes the 11:00 measurement a good candidate for comparison with the ALOMAR data. The following figures are made from this set of data.

The figure 4.20(a) shows the path that the CALIPSO satellite used when making the measurement used in this case. As can seen from table 4.5, the distance between the passing satellite and the ALOMAR location is much closer for this case than the previous and the comparison can be made with higher confidence. The cloud data from CALIPSO shows a large cloud just below the tropopause between $66°N$ and $70°N$, which is the closest profiles to ALOMAR. This can be seen from figure 4.20(b). There are two features of this cloud that would indicate that this cloud is not cirrus cloud. Some parts of the cloud have base altitudes below the 6 km limit set for cirrus cloud. The thickness of this cloud is also quite large, around 4 km at its thickest. But the closeness in both time and location to the ALOMAR measurements makes it very probable that this cloud is connected to the cloud in the ALOMAR measurement. The cloud from the ALOMAR data also shows quite large vertical extent. There are also some other features found in the cloud height

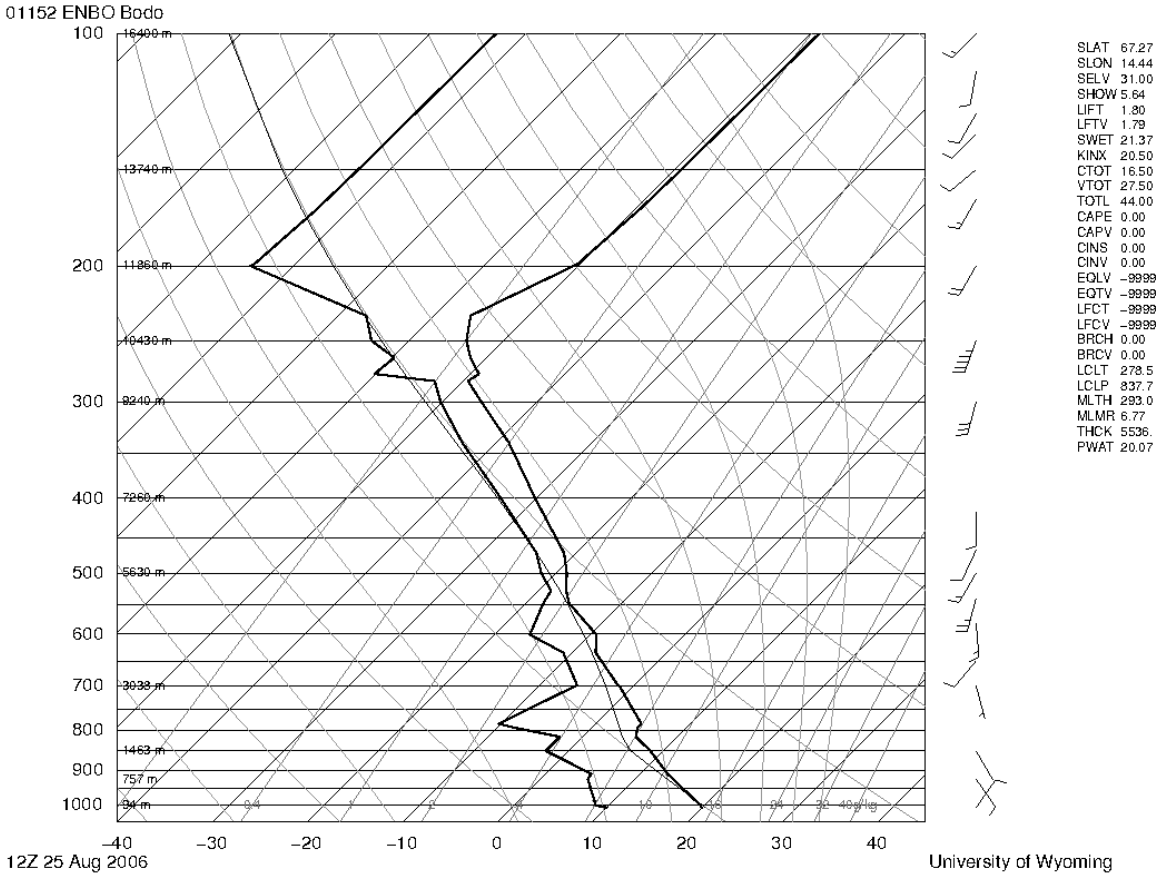

Figure 4.19: Skew-T temperature profile from the Bodø radiosonde at 1200 on the 25th of August 2006. The black line to the right is the temperature profile and the black line to the left is the dew point temperature profile. The diagram also shows the wind speed and direction, but this is not used in this thesis.

plot. A very low cloud can be seen above $66°N$, and some sort of feature is located just above the ground at $73°N$. Neither of these are cirrus clouds. The feature situated at $66°N$ is a lower cloud feature. The ground aerosol layer that often is misinterpreted as clouds in these data is not very prominent in this plot, but could explain the other low feature. Figure 4.20(c) shows the temperature found by the CALIPSO satellite within the cloud layers. These temperatures range from between $-25°C$ to $-55°C$, with the lowest temperatures belonging to the highest cloud layers. These temperatures fit well with the temperatures that were found from the radiosonde measurements earlier.

The ALOMAR measurement time that is compared with the CALIPSO data is always the time of the middle profile in the set of measurements. Since the CALIPSO measurements are only just above 1 hour from this measurement is this the only case where some of the measurements from the two instruments actually are made at almost the same time. The location of the CALIPSO satellite is also very close to the ALOMAR location during these measurements. The cloud seen in the ALOMAR profiles and the cloud seen in the CALIPSO profiles is therefore very likely the same cloud or at least a part of the same cloud system. The temperatures for the two clouds are also very similar. This seems to

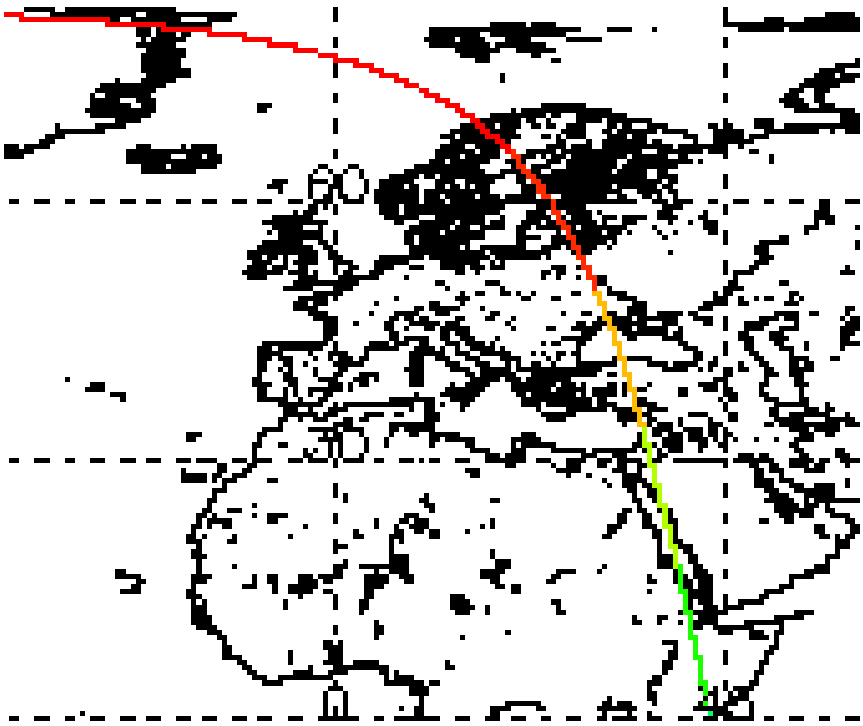

(a) Geolocated path of the CALIPSO satellite during the measurement used in this case

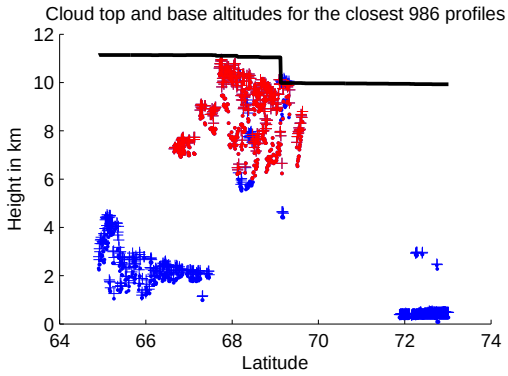

(b) Clouds found in the closest CALIPSO profiles. Crosses are cloud top heights and dots are cloud base heights. Red crosses and dots are probable cirrus clouds(altitudes between 6000m and tropopause height) blue crosses and dots are other features, presumably clouds. Black line indicates the tropopause height.

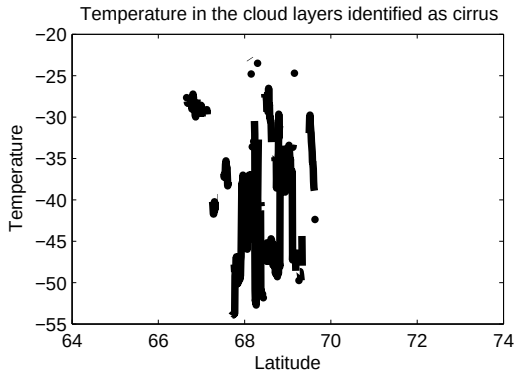

(c) Temperature for the clouds in The CALIPSO data

Figure 4.20: CALIPSO results of the 25th of August case

File	CAL_LID_L2_01kmCLay-Prov-V2-01.2006-08-25T02-14-57ZD.hdf	
	Closest in time	closest in space
time	03:07:15	03:06:07
latitude	67.75N	71.47N
longitude	-0.25V	4.86V
distance (km)	680.70 km	501.43 km
time difference (s)	22672s	22740s
time difference (h)	6.30 h	6.31 h
File	CAL_LID_L2_01kmCLay-Prov-V2-01.2006-08-25T10-29-18ZD.hdf	
	Closest in time	closest in space
time	10:29:16	11:10:37
latitude	-77.14N	69.03N
longitude	87.75V	16.20V
distance (km)	16909.40 km	8.79 km
time difference (s)	-3849 s	-6330 s
time difference (h)	-1.07 h	-1.76 h

Table 4.5: This table gives the time, latitude and longitude of the profile closest to the ALOMAR location, and the profile closest to the time of the ALOMAR data used in this case. For the last calculation is the middle profile in the ALOMAR data used. In addition are the calculated differences in time, both in seconds and hours, and distance given for both possible files.

be an extensive cloud layer that may display some fall streak precipitation. Because the cloud found in the CALIPSO measurement is so thick it could also mean that the cloud layer is a large cirrus cloud that is deepening to an altostratus.

4.4.2 Optical depth

The optical depth of the cloud can be seen in figure 4.21. This value is quite high for this cloud. The optical depth is between 2 and 4 during the first 3 hours of the measurements that is in the first set of measurement in figure 4.17. The optical is approximately 2 in the first half of the next measurement set, but reaches values between 5 and six in the last half of this measurement. The low first part of this set are connected to the lower backscattering that can be seen in this area from figure 4.18. This lower backscattering is connected to less ice crystals in this part of the cloud. There are two large dips in the optical depth, one just before four hours have passed and one just before 6 hours have passed. These dips coincide with the profiles where the base height is found too high, as can be seen when comparing with figure 4.18 The drop from a depolarization ratio of 0.5 to zero between 3 and 4 hours is due to the stop between the two measurement sets and the straight diagonal line here is not actual optical depth measurements. This cloud was therefore clearly visible throughout the measurement. From table 2.4 can it be seen that clouds with optical depths above 3 should be classified as altostratus clouds and not cirrus clouds. Some parts of this cloud are above this limit, but not all of the cloud is. This cloud

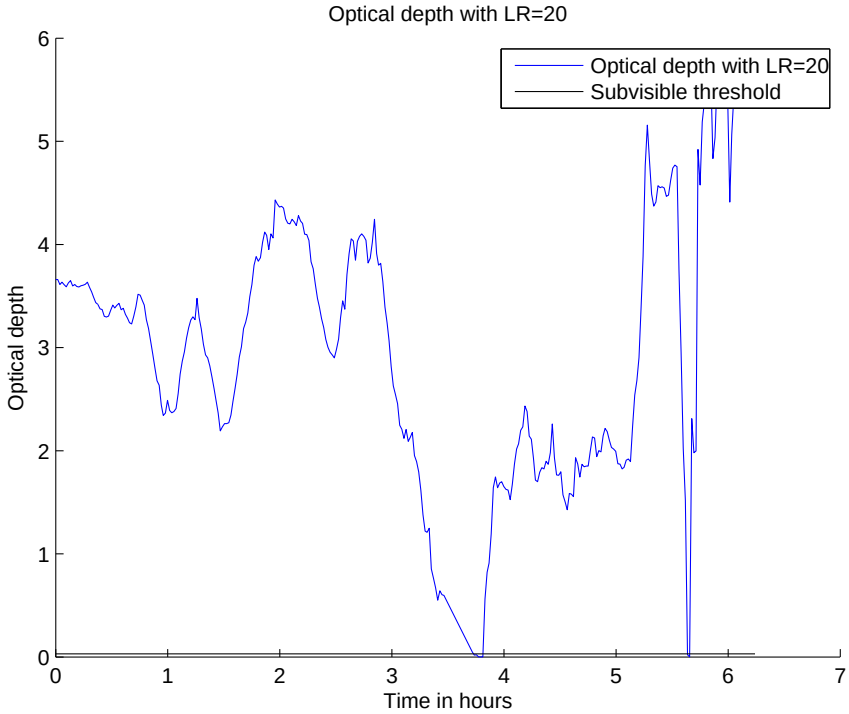

Figure 4.21: Optical depth of cloud detected on the 25th of August 2006. Blue line indicates optical depth calculated with the Particular Integration method with effective Lidar ratio= 20. Black line indicates the limit for the subvisible clouds; optical depth = 0.03

is therefore on the edge between a thin altostratus cloud and a thick cirrus cloud.

4.4.3 Depolarization ratio

Figure 4.22 shows the depolarization ratio of the cloud. The dark blue areas at the top of the cloud in the depolarization plot coincides with the areas in figure 4.17 that looks as partially clean air between the fall streaks and the main parts of the cloud. This approximately clean air should therefore have a depolarization ratio close to zero. The rest of the cloud is mostly light blue corresponding to a depolarization ratio below 0.2. Some small areas at the top of the cloud are yellow and even close to red. This corresponds to depolarization ratios close to and above 0.4. Since this cloud is assumed to be an ice cloud would this value indicate that the ice crystals are predominately plate shaped, because most of the cloud has depolarization ratios below 0.2. Plate shaped ice crystals will have depolarization ratios below 0.25 as previously mentioned. The areas that are yellow or red are possibly irregular or intermediate crystals since these have depolarization ratio values from 0.25 to 0.5. An increasing number of irregular ice crystals could indicate that the ice cloud is getting older. The longer the ice crystals reside within the cloud the more complex will the ice crystal shapes be because of effects as riming and collisions that change and complicates the structure of ice crystals. However, the edges of the clouds have often showed higher depolarization ratios throughout this thesis. Some of these high depolarization ratios can come from increased noise at the cloud edges, as can be seen in the single profile depolarization ratios of section 4.2.3. The cloud in figure 4.22 also have some

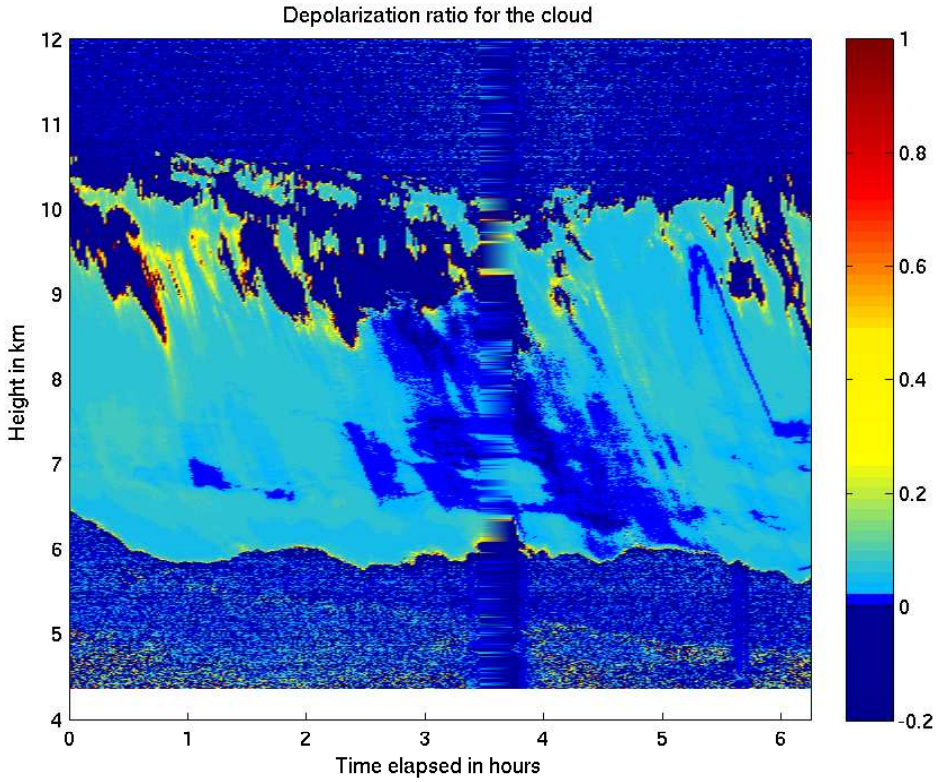

Figure 4.22: Depolarization ratio for the cloud detected on the 25th of August 2006. Dark blue indicates depolarisation ratio of 0 or less.

areas within the lower part of the cloud which show depolarization ratios of close to zero (dark blue). These areas are not as dark as the upper parts that were previously explained as clean air. When closely comparing figure 4.22 with figure 4.18 can it be seen that these areas coincide with areas within the cloud with areas with a bit lower backscattering than the rest of the cloud. These areas are probably areas with less ice crystals than the rest of the fall streaks. Less ice crystals will lead to less backscattering. The clean air around the ice crystal will have a larger influence on the depolarization ratio in the areas with less ice crystals. The backscattering in the fall streak region is higher around the middle of the fall streak region. This could come from that when the ice crystals grow larger will their backscattering increase. The ice crystals will grow some distance before they begin to sublimate as they fall into warmer regions of the atmosphere. The backscattering will then begin to decrease. The backscattering will also be less if the number of particles decreases. It is very clear that this cloud is an ice cloud because of the high altitude of the upper part of the cloud where the ice crystals are formed. The ice crystals will have to reach altitudes with temperatures above $0°C$ before they will begin to melt. This is not the case for this cloud as was shown from figure 4.19 earlier. This cloud does not experience temperatures below $-15°C$. The ice crystals will therefore not melt because of increasing temperature when they fall into lower layers of the atmosphere, but rather sublimate as the lower layers are dryer.

4.4.4 The weather situation on the 25th of August 2006

A weather chart from 09:00 on this day has been used to show the weather situation from this day. The 09:00 charts can be seen in figure 4.23(a) and in figure 4.23(b). The former show that the weather in northern Europe is dominated by one low east of the Baltic sea with an occluded front, and a low pressure system off the eastern coast of Greenland. This figure also shows some fog in the northern part of Scandinavia. A closer look at northern Norway with synoptic observations can be found in figure 4.23(b). The observations at Andøya show that both cirrostratus and double layered altocumulus was observed at this point. Fog has been observed by several of the other stations in northern Scandinavia. This seems to fit with what is found in both the CALIPSO and LIDAR data. The cloud found there is quite thick and can at leas partially be classified as an altostratus cloud from its optical dept. The LIDAR cloud also seems to be deepening.

Figure 4.24 shows the 11.5-12.5 μm image from the AVHRR instrument onboard the NOAA satellite from 09:59 on the 25th of August. Two cloud features dominate this image. One is connected to the occluded low above the Baltic sea. This cloud shape still have some remnants of a spiralling shape, but the cloud cover is more dispersed as the low seams to be weakening. The second cloud feature is situated above northern Germany and seems to be stronger because the hook shape is much clearer for this feature. The low that these cloud are connected to can not be seen in the weather charts because it is too far south. A cloud sheet can be seen off the coast of northern Norway which also includes the area around Andøya. This cloud sheet seems to be very thin around the Andøya location. Since parts of this sheet is very white can it be assumed that these parts are high and cold clouds, probably cirrus clouds. Below these parts are there areas that are greyer in colour, which means that these clouds are lower and warmer than the white parts of the sheet. Both the lower warmer clouds and the higher colder was found in the CALIPSO data, and the ALOMAR cloud is also clearly a part of this cloud sheet. The clouds found in the data seem to be connected to the ageing occluded low above the Baltic sea.

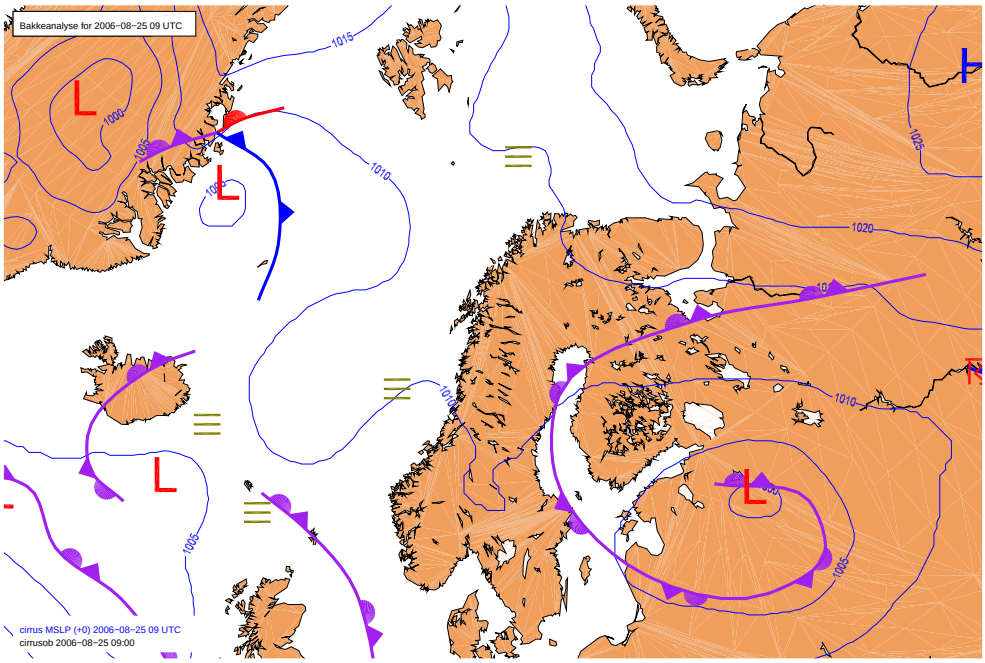

(a) Weather analysis from DNMI on the 25th. of August (09:00)

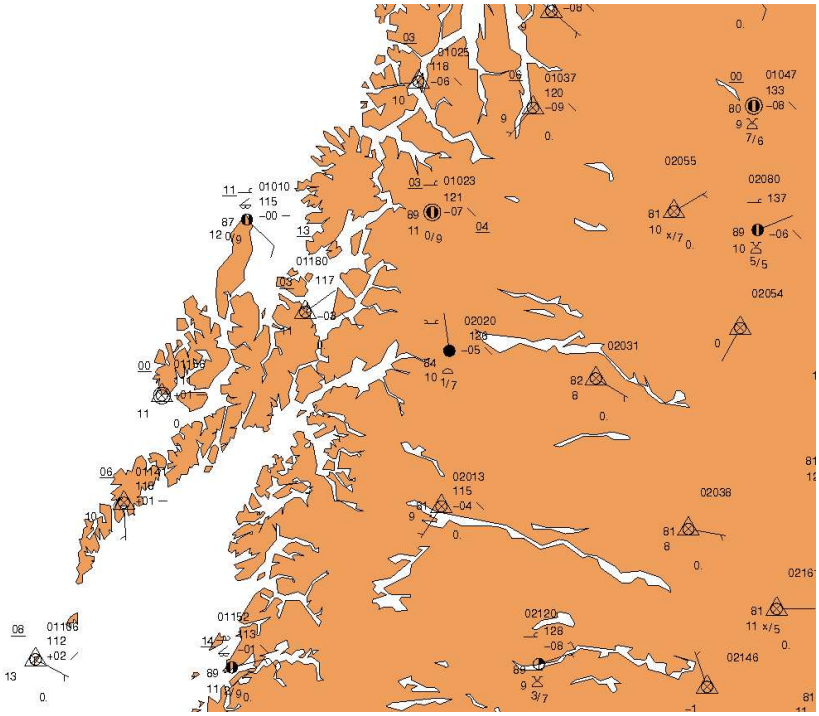

(b) Weather analysis with synop observations from DNMI on the 25th. of August (09:00)

Figure 4.23: Weather charts from DNMI from the 25th of August 2006 (09:00)

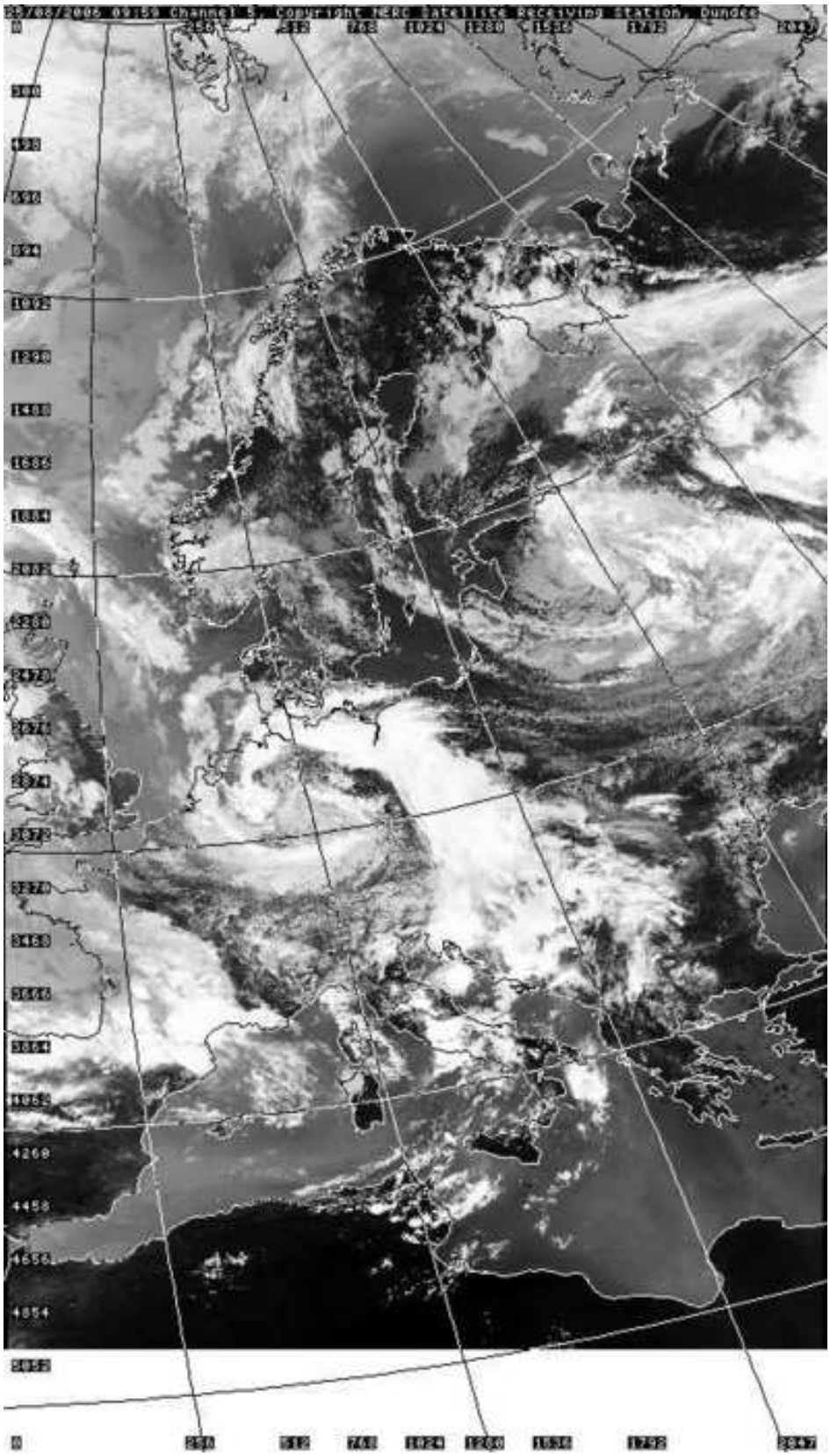

Figure 4.24: Satellite image from NOAA AVHRR at 09:59 on the 25th of August. This image is from the thermal infrared channel at 11.5-12.5 μm. Source: www.sat.dundee.ac.uk

4.5 14-15 September 2006

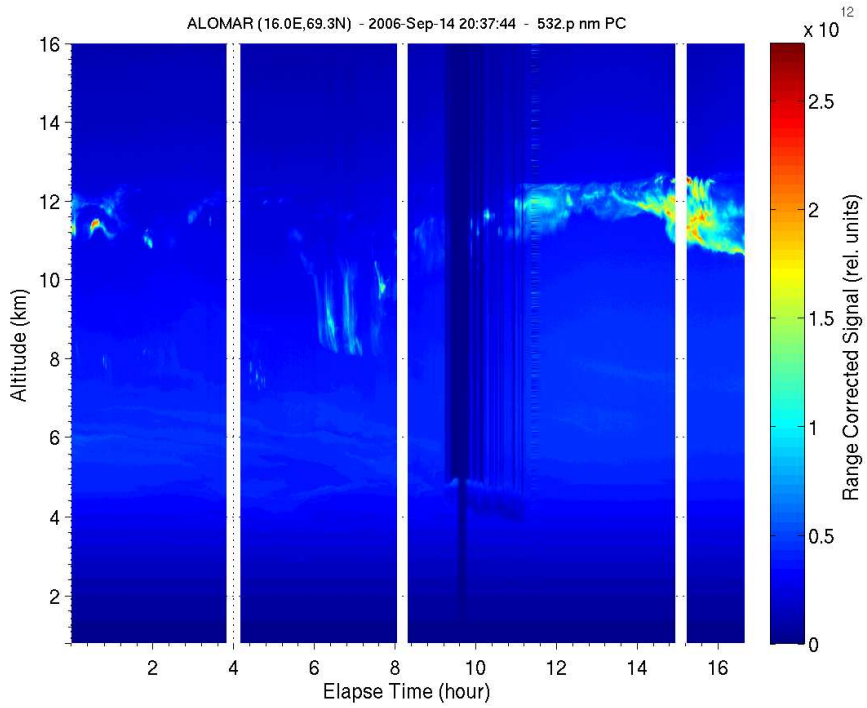

Figure 4.25: Quickplot of all measurements from 14-15 September 2006

Four sets of atmospheric measurements were taken during these two days, as can be seen in figure 4.25. Around 16 hours of measurements were taken during two days, from 20:30 on the 14th, to approximately 13:00 on the 15th. Since most of the measurements were taken during night time, one can assume that atmospheric noise was at a minimum. Sunlight may give an increase in the noise during the last hours. Some small cloud patches can be seen approximately in the 10.5 - 12 km range in the first set of measurements . In the second set of measurements the cloud is still consisting of small fragments but the height has changed to around 8-10.5 km. During the two last sets of measurement a larger more substantial cloud is coming into view. The height of this cloud is approximately between 10 and 12.5 km and the signal strength reaches a maximum in the middle of the cloud. The rest of the small cloud parts detected during these measurements seem quite thin and has a low range corrected signal strength. The RCS is in this case between 0 and $6(*10^{12})$ for the clear atmosphere and between 9 and $20(*10^{12})$ for the cloud. It is likely that these clouds are cirrus clouds because of their height and thin appearance. The focus will further on be on the last set of measurements where the densest cloud can be found.

4.5.1 Cloud heights

Figure 4.26 is a closer view of the last set of measurements. The calculated height of the cloud top and base is also added to the plot. It can be seen that the heights remain relatively constant throughout this set of measurements the only change is a small expansion in both directions. This expansion can be explained by the diffusion of the cloud particles out of

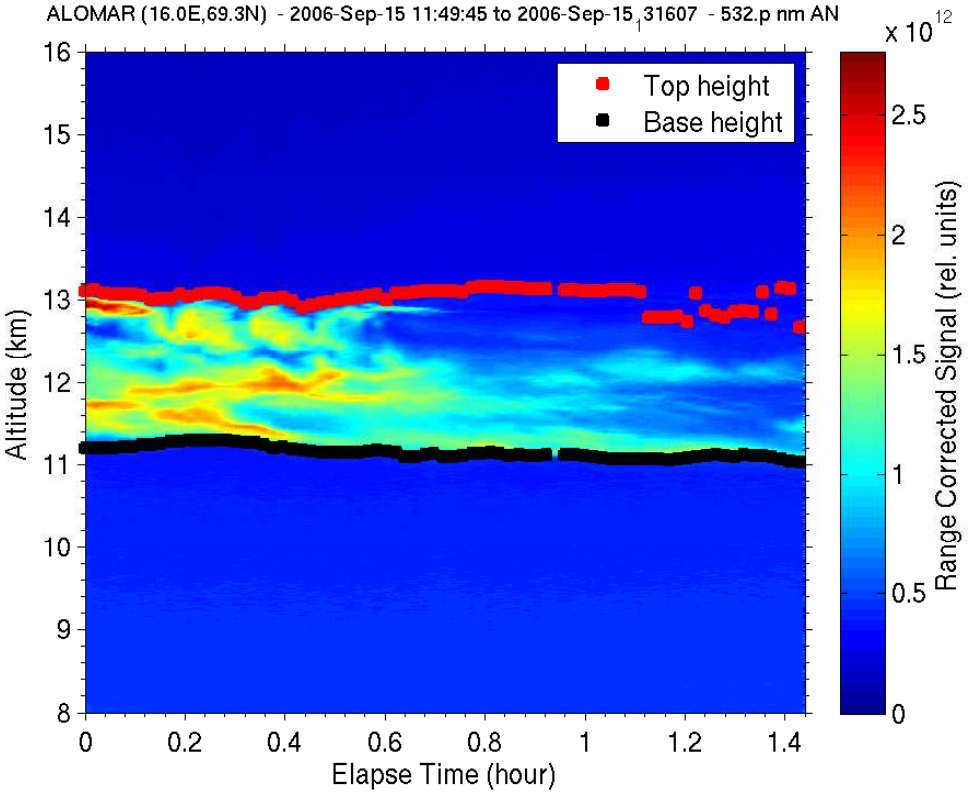

Figure 4.26: Plotted measurements from 14th September 2006 with calculated cloud boundaries. The upper cloud layer top detected is marked in red. The lower cloud layer base is marked in black.

the cloud boundaries as the cloud ages. The cloud keeps its boundary heights through this set of measurements but the signal strength weakens substantially during the last hour. The cloud seems to become less dense and even break up into several thinner layers. The program that calculates the top and base heights finds the top and base altitudes for several cloud layers in each cloud, but only the upper top and the lower base is plotted in this figure. The layers of each cloud have not been investigated in this thesis. There is a strong backscattering in the lower middle part of the cloud which seems to rise up to the middle of the cloud during the first half hour of the set before it disappears. This can either indicate a denser part of the cloud or a layer of horizontally oriented particles. To investigate this further one needs to look at other variables.

Figure 4.27 shows a radiosonde measurement from the Bodø radiosonde station made at 12:00 on the 14th of September 2006. The 14th of September measurement was chosen because there were no measurements from the 15th of September in the measurement database at the webpage of the University of Wyoming[5]. It can be seen from the temperature profile that the temperature(the thick, black line to the right) decreases from $0°C$ to $-65°C$ between 3 km(850 mb) and 12 km(200 mb). The tropopause level is at approximately 12 km. The cloud is located between 11.5 km and 13.5 km, and would therefore be located at the tropopause. The temperature of the cloud is therefore $-65°C$ at the base of the cloud and $-55°C$ at the top of the cloud. The temperature and dew point profiles indicate

[5]http://weather.uwyo.edu/upperair/sounding.html

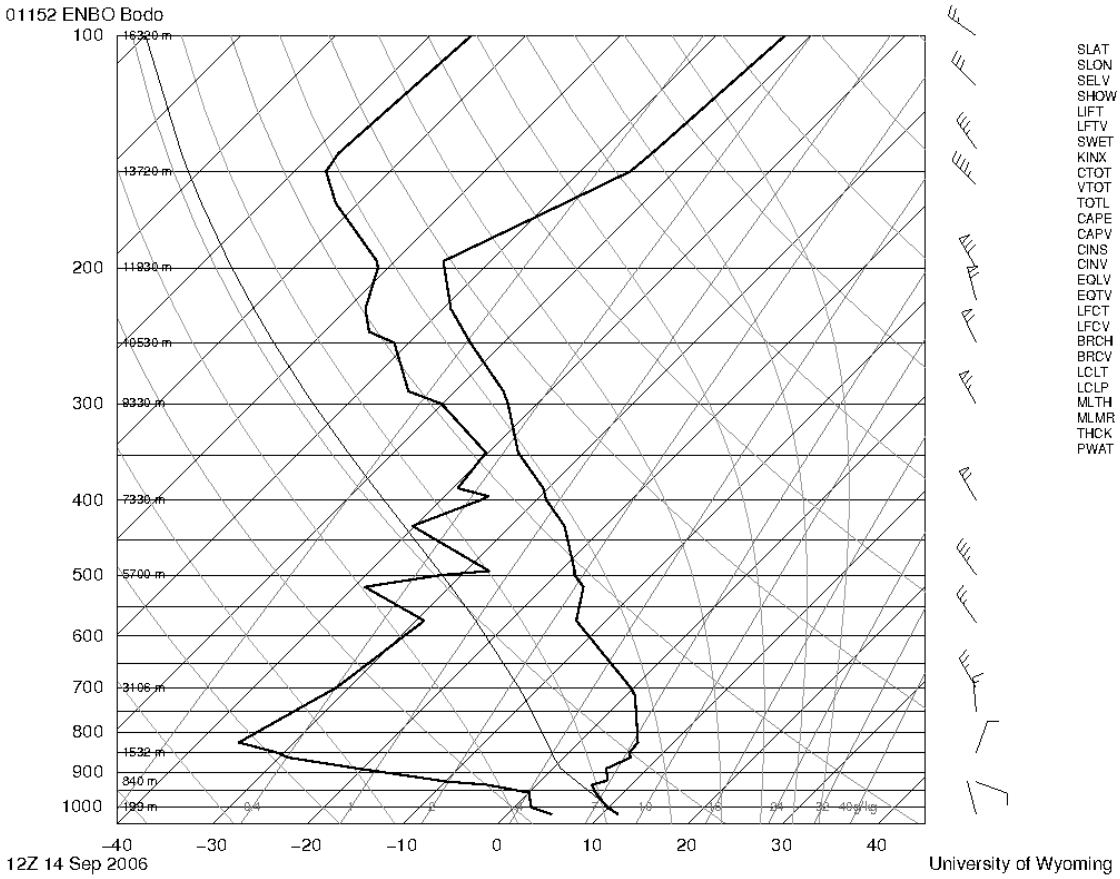

Figure 4.27: Skew-T diagram from the Bodø radiosonde. This profile is from the 14th of September at 12:00. The diagram shows the temperature profile(right) and the dew point temperature(left). This diagram also shows the wind speed and direction, but this is not used in this thesis.

that the atmosphere is a bit dry at the altitude where the cloud is located. There is more moisture between 450 mb and 200 mb where the two profiles are closer. The heights and temperatures found from figure 4.27 could be erroneous because they were taken a day before the cloud was measured. there is a possibility that the tropopause and the moist area were higher at the 15th, than what the profile from the 14th show. The measurements that were taken on the 14th with the tropospheric LIDAR also show some small cloud patches, and some of these clouds are lower than the cloud investigated from the 15th.

CALIPSO data

There was one close overpass of the CALIPSO satellite for this case. This set of profiles was made during the 14th. and the interesting feature was found in the ALOMAR profiles from the 15th. The fit between these data is therefore not ideal. The measurements from the CALIPSO satellite were made over 25 hour before the ALOMAR measurements. The closest position in space was in addition over 200 km from the ALOMAR location. This should have been accounted for in some way since the measurements were made far away

both in time and space. An interpolation of the data involving atmospheric dynamics could possibly have been used to connect the ALOMAR data more closely to the CALIPSO data. This section is a bit more unreliable than the other CALIPSO comparisons because of this. Table 4.6 shows the information about time and location for the closest profiles in both time and space from the available overpass.

File	CAL_LID_L2_01kmCLay-Prov-V2-01. 2006-09-14T10-02-42ZD.hdf	
	Closest in time	closest in space
time	10:55:00	10:46:22
latitude	74.73N	69.98N
longitude	-106.07V	21.17V
distance (km)	3542.72 km	229.69 km
time difference (s)	92162s	92680 s
time difference (h)	25.60 h	25.74 h

Table 4.6: This table gives the time, latitude and longitude of the profile closest to the ALOMAR location, and the profile closest to the time of the ALOMAR data used in this case. For the last calculation is the middle profile in the ALOMAR data used. The calculated differences in time, both in seconds and hours, and distance given are also given for both possible files.

Figure 4.28(a) shows the path of this overpass, and as mentioned earlier this passing is not particularly close to the ALOMAR site. The next two figures show the cloud information from the profiles that were closest to ALOMAR. One cirrus cloud can be found in figure 4.28(b). This cloud is located at approximately $73°N$ around the tropopause height, which is approximately at 11 km. The program that makes this plot does not consider the parts of the cloud with altitudes above the tropopause as cirrus clouds. However, some cirrus reach above the tropopause, so this cloud is still considered a cirrus cloud and not a stratospheric feature, since most of the cloud is below the tropopause height given by CALIPSO. The other feature in the height plot is the ground aerosol layer. Why this have been interpretated as an aerosol layer have been explained in earlier cases. The temperature of the cloud layers identified as cirrus can be found in figure 4.28(c). The temperatures are between $-53°C$ and $-54°C$ for the cirrus cloud found in figure 4.28(b). These temperatures are close to the temperatures found for the ALOMAR cloud in the radiosonde measurement($-55°C$-$-65^{circ}C$). The high altitude and low temperature of this cloud easily identify it as a cirrus cloud. Comparing it to the cirrus cloud in the ALOMAR case on the other hand, is a difficult task because of the differences in time and location. The cloud found in the CALIPSO data is a very small cloud patch at approximately the same height as the ALOMAR clouds, and the ALOMAR data from this day seems to include a lot of smaller cloud patches.

4.5.2 Optical depth

Another interesting parameter is the optical depth of the cloud and how it changes during the set of measurements. The optical depth can be seen in figure 4.29. The optical depth of this cloud begins at 1 and it varies between 1 and 1.4 during the first half hour. The

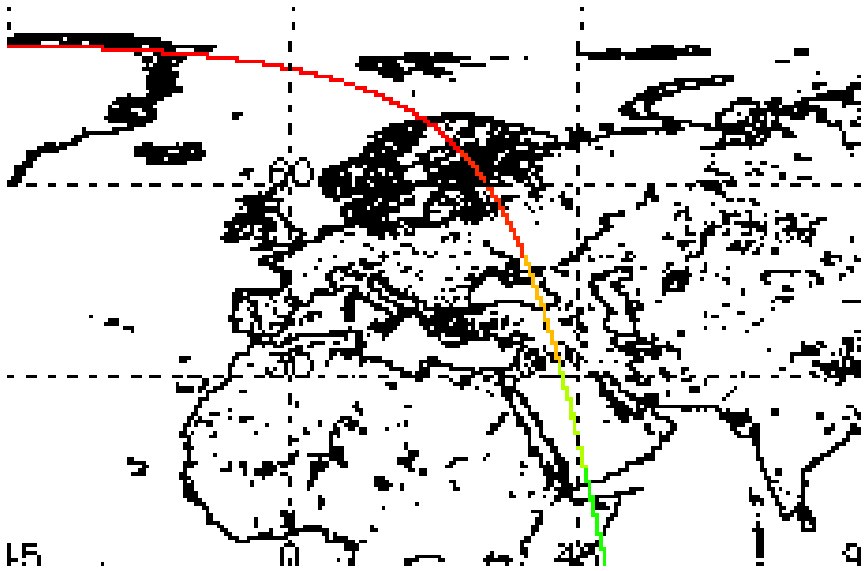

(a) Geolocated path of the CALIPSO satellite during the measurement used in this case

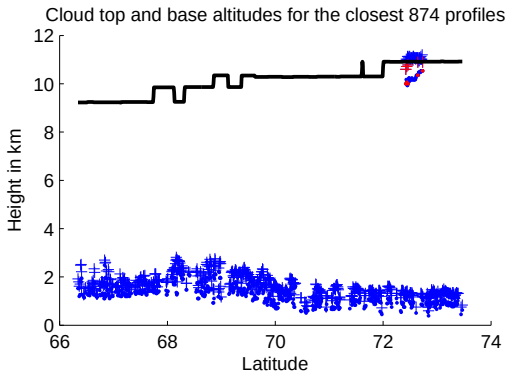

(b) Clouds found in the closest CALIPSO profiles. Red markers are probable cirrus clouds(altitudes between 6000m and tropopause height) and blue markers are other features, presumably clouds. Black line indicates the tropopause height.

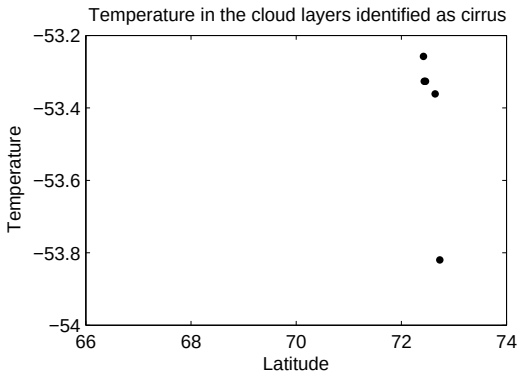

(c) Temperature for the clouds in The CALIPSO data

Figure 4.28: CALIPSO results of the 15 September case

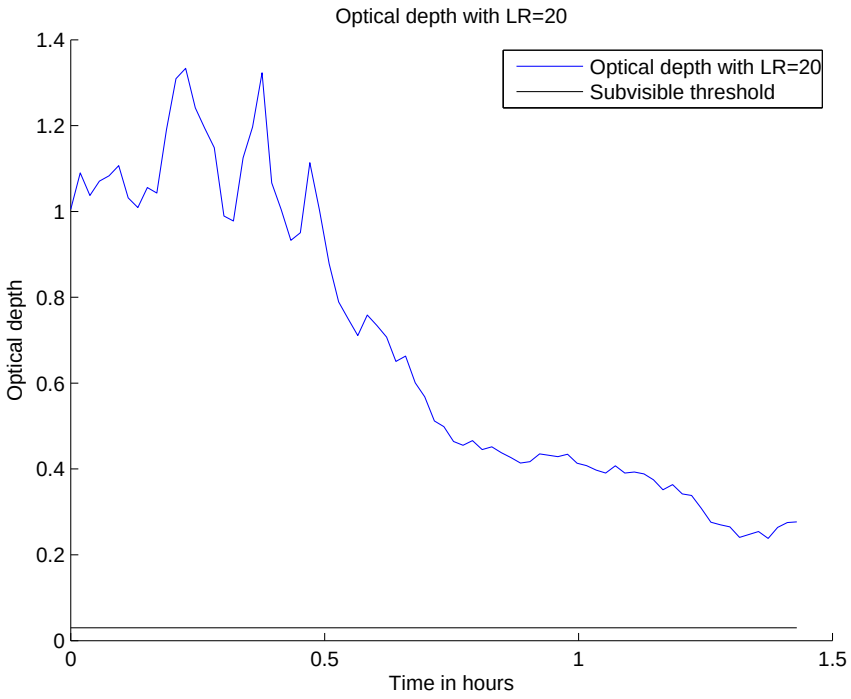

Figure 4.29: Optical depth from the 1064 nm channel. The optical depth for the cloud is given in blue, the black line is the limit value for subvisible clouds; optical depth = 0.03

optical depth begins to sink after this, and has sunk to approximately 0.4 during the last hour of measurements. The type of cirrus cloud can now be determined from the limits in table 2.4. An optical depth of between 0.4 and 1.4 means that the cloud can be classified as an opaque (τ=0.3-3.0) cloud throughout the measurement set, but the value is close to the thin (τ=0.03-0.3) cloud limit. This change in the depolarization ratio fits with the fact that the cloud is becoming less dense in the latter part of the measurement.

4.5.3 Depolarization ratio

Figure 4.30 shows the depolarization ratio of the cloud. This cloud shows a fairly consistent low value for the depolarization ratio witch rarely exceeds 0.2. There are however some very small areas in the highest part of the cloud during the last hour that looks like they could be above 0.2. The most striking feature, which has a value of approximately 0, in this plot can be seen during the first half hour. This feature coincides with the area in figure 4.26 with the strongest backscattering. A strong backscattering and close to zero depolarization is an indication of horizontally oriented ice crystals. This layer with the high backscattering and the close to zero depolarization is located between 11.5 and 12 km. The layer temperature is therefore well within the limit needed for pure ice clouds. The layer will not have any supercooled cloud droplets because of the low temperature, it has to consist of horizontally oriented ice crystals. When the cloud is getting thinner during the last hour of the set of measurements are there numerous patches with depolarization ratio at 0 or lower. This is in the same area as the highest number of cloud layers and can be explained by small areas of cloud free air where the noise exceeds the backscattering signal and dominates in the data. Since the layer with horizontally oriented ice crystals

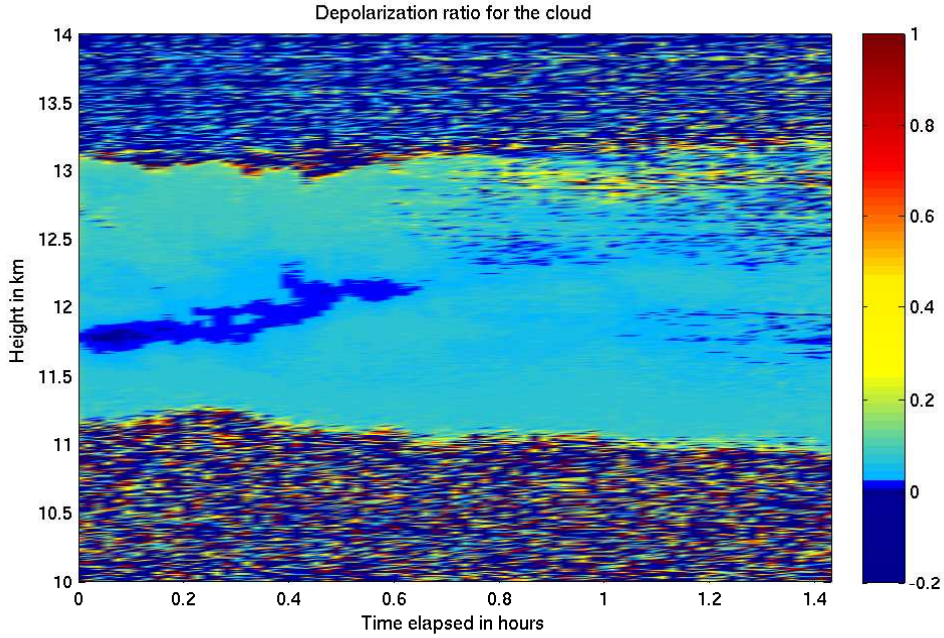

Figure 4.30: Depolarization ratio of the cloud. Dark blue indicates a depolarization ratio of 0 or less. The clear atmosphere around the cloud is filled with speckled noise.

is surrounded with such plates, is it likely to conclude that the layer also consist of plate shaped ice crystals since plate shaped ice crystals will easily orient themselves horizontally. This was explained in section 2.3.2. Only a few small areas in the upper part of the last hour show a tendency toward irregular/intermediate crystals. An aging cloud will often consist of more complex and irregular crystals due to processes as riming, collisions and aggregation. This could indicate that the cloud is getting older. But the presence of complex ice crystals as the bullet rosette could also mean that the conditions for ice crystal formation, that is temperature or perhaps CCN type, is changing for some parts of the cloud.

4.5.4 The weather situation on the 15th of September 2006

As for the earlier cases, the clouds seen in this case are connected with synoptic scale weather systems. Figures 4.31(a) and 4.31(b) show the weather analysis from DNMI at 12:00 from this day. The dominating features are a frontal system in the Nordic ocean and a high pressure above the gulf of Bothnia. The synoptic observation at Andøya shows, as for some of the previous cases, thin altocumulus clouds and some cirrostratus. By the other stations close to Andøya are also mostly thin altocumulus type clouds and cirrus type clouds reported. Some stations on the main land towards Sweden have observed denser and lower clouds such as cumulus and stratocumulus. The much smaller cloud found in the CALIPSO data can also be connected with this frontal system. Since the CALIPSO measurement was made more than a day before the ALOMAR measurement is it likely that the frontal system was further away from the measurement site, which would indicate more of the high cirrus type clouds and less altostratus and altocumulus clouds. From figure 4.25 can it be seen that in the beginning of the ALOMAR measurement, which

was on the 14th, was there many smaller patches of clouds, which can fit with the cloud observed in the CALIPSO measurement.

The dominant cloud features in the satellite image in figure 4.32 is the clouds connected to the frontal system that dominates above the Atlantic ocean. A large cloud feature follows the cold front from the shore of Greenland down to Great Britain. The clouds found in the ALOMAR data, on the other hand, is connected to the clouds that follow the warm front in the northern part of the Atlantic ocean. Some thin parts of this large cloud sheet reach the northern part of Norway and is detected by the tropospheric LIDAR at ALOMAR. Some lower cloud sheets can also be seen over northern parts of Sweden and southern Norway. These sheets are much greyer than the clouds connected to the frontal system in the Arctic ocean, and are therefore much lower and warmer than the bright white clouds. These are probably the cumulus type clouds that where reported on the mainland stations in figure 4.31(b).

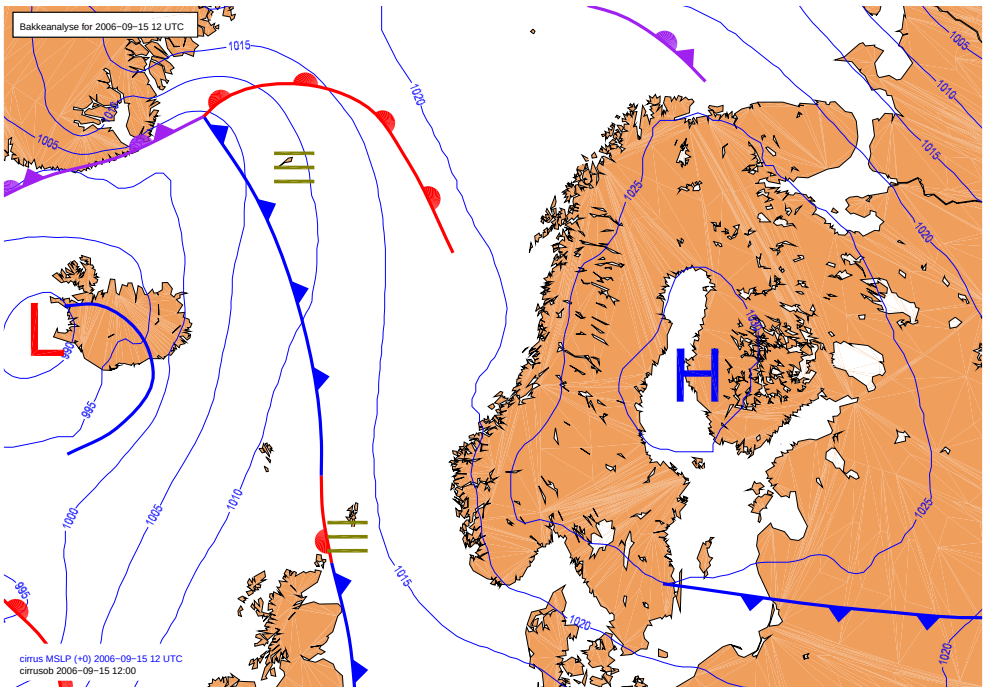

(a) Weather analysis from DNMI on the 15th. of September (12:00)

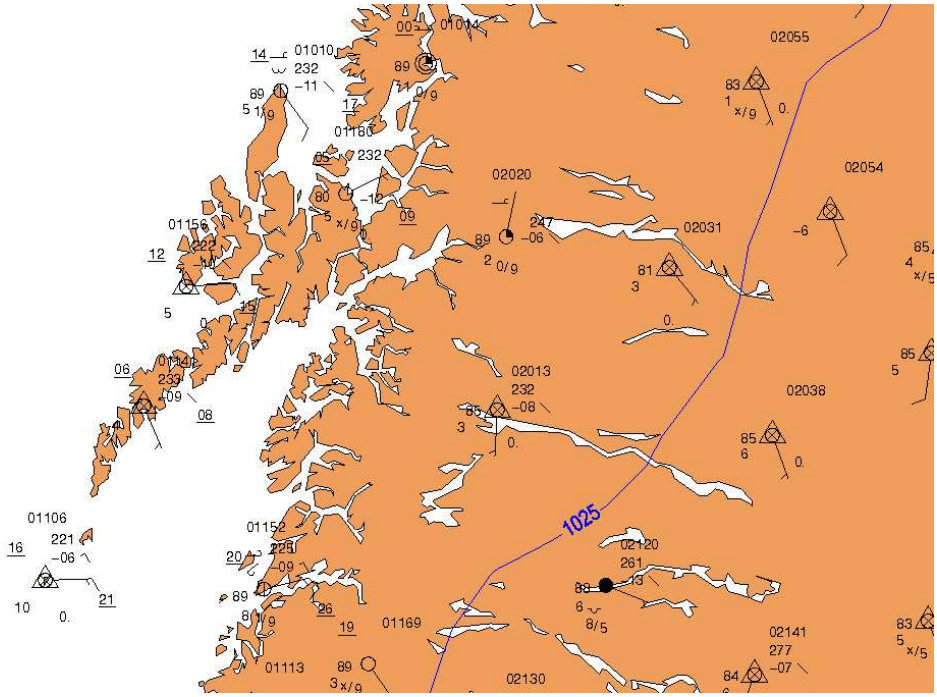

(b) Weather analysis with synop observations from DNMI on the 15th. of September (12:00)

Figure 4.31: Weather charts from DNMI from the 15th of September 2006

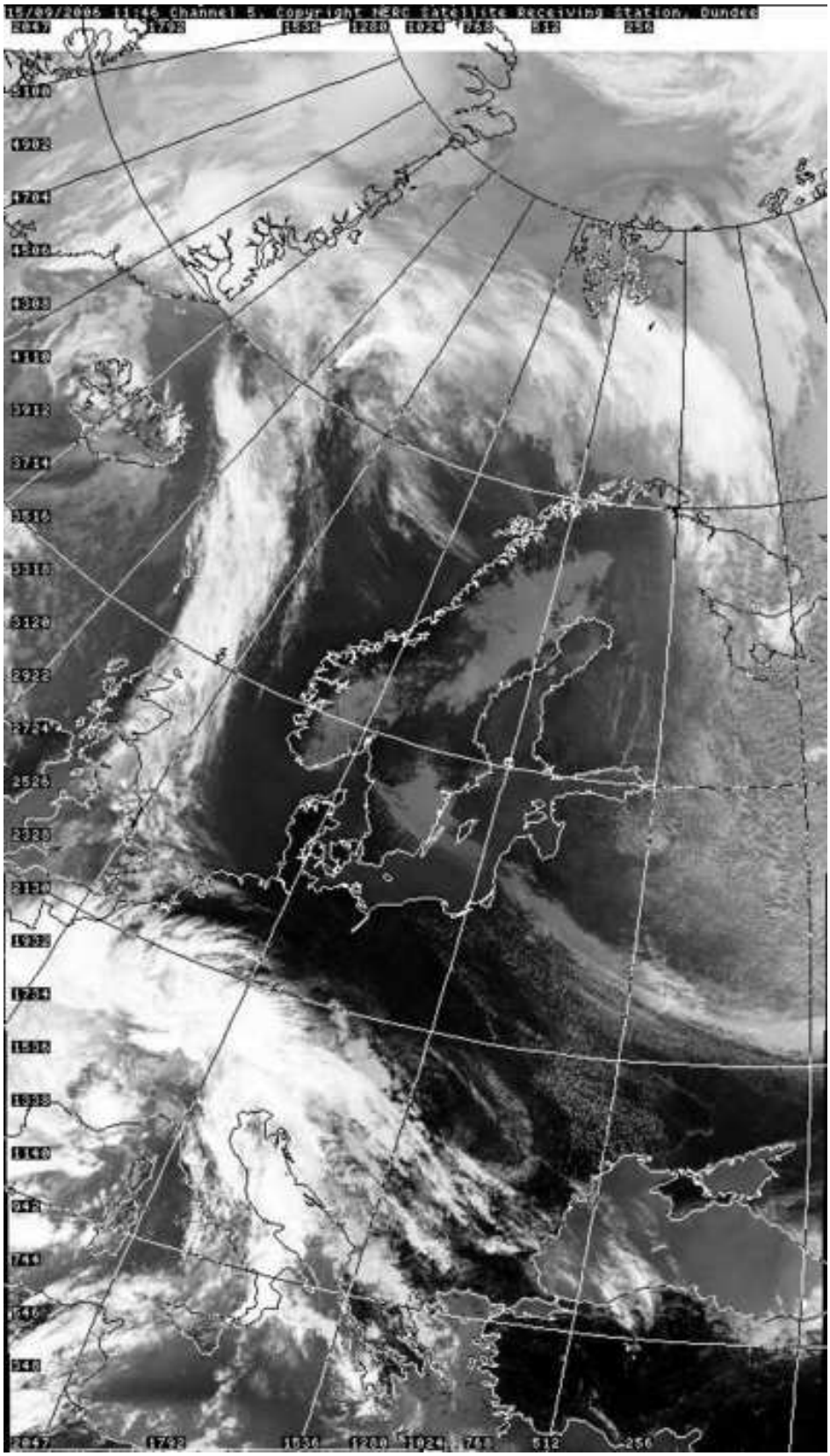

Figure 4.32: Satellite image from NOAA AVHRR at 11:46 on the 25th of August. This image is from the thermal infrared channel at 11.5-12.5 μm. Source: www.sat.dundee.ac.uk

Chapter 5

Summary and conclusion

The main objective of this thesis was to give an overview of some of the microphysical properties of cirrus clouds above ALOMAR. The main focus has been on the height of the clouds, the optical depth and the depolarization ratio. These properties of cirrus clouds have been investigated with the use of the Tropospheric Lidar system at the ALOMAR observatory at Andøya($69°N$,$16°E$). The wavelengths that have been used in this thesis are the 532 nm and the 1064 nm wavelength. The former is used to find the depolarization ratio and the latter is used for the height and optical depth retrieval. Three case studies have been made in this thesis; the 15th of August, the 25th of August and the 15th of September. A short climatology has also been included. This has been done because more information about cirrus cloud coverage and properties are needed to extract information about the radiative effects of these clouds. This information is one of the most uncertain factors in the modelling of the earth's climate. The radiative properties of cirrus clouds depend on both their microphysical properties and their location in the atmosphere. The cloud height found from the LIDAR data and the cloud temperature found from radiosonde measurements has been compared to cloud height and temperature data from the CALIPSO satellite. The clouds found in the LIDAR data have also been related to the weather situation in each case trough weather charts and satellite images.

A full statistical analysis of the ALOMAR data would have been very useful for extracting cloud information. But the Tropospheric Lidar at ALOMAR has only been in operation for three years which is a bit short for a proper statistical analysis. There are also some factors that limit the number of measurement hours made. The system is only operated during fair weather conditions and the measurements depend on the staff that is available at ALOMAR at all times, since the system is not fully automatic. Technical problems have also limited the number of measurements taken. The year 2006 was chosen for investigation since the CALIPSO data were compared with the ALOMAR data, and this satellite was launched during 2006. Cases were chosen from the latter part of this year, and a one year climatology was made for the total year. This one year climatology included a presentation of the measurements made during this year, and the number of cirrus clouds found in these measurements. The heights of these clouds were also presented for each month of 2006. This climatology showed that during 2006 the mean cirrus cloud heights were approximately 9 km for the top of the cloud and approximately 8 km for the base of the cloud. Figures 4.2(a) and 4.2(b) on page 56 also show that the number of measurement hours with detected cirrus vary throughout the year, but the percentage of cirrus clouds in the measurement seems to be almost the same in many of the months.

The exception is April and May, which have a much higher percentage of cirrus clouds. April and May are months that often have a high amount of high pressure systems and fair, warm weather. High cirrus clouds are often present under such conditions. It has not been investigated if this is the case in these data. A longer climatology over several years will reveal if April and May always have a higher amount of cirrus clouds.

There are however one major problem with this climatology. The program that made these plots does not find all of the clouds because it has not been possible to make the cloud detection automatically, as it has been done in this thesis, for a whole year. The cloud detection used in this thesis depends on two aerosol free regions, one above and one below any cloud in the LIDAR profile. It is not possible to do the detections automatically in the lower region, which is used to normalise the molecular profile to the LIDAR profile, because clouds and aerosols are often present in the lower parts of the atmosphere. No particular region in the lower 12 km can therefore be assumed to be cloud and aerosol free throughout the year. The upper cloud and aerosol free region was therefore used for both the normalisation and to find the cloud threshold, this makes the normalisation much less accurate because of a higher amount of noise in this area. The climatology has still been included as a first approximation, but should be improved to give a more accurate description of the cirrus cloud coverage above ALOMAR.

Three case studies, the 15th of August, the 25th of August and the 15th of September, were further investigated. The first and last case showed relatively thin(1-2 km), high and cold cirrus clouds. The 25th of August case showed a cloud that was close to altostratus cloud in thickness. These days were chosen as cases because the profiles from tropospheric LIDAR included clouds on these days, and the CALIPSO satellite made a pass that were close to ALOMAR on these dates. Whether or not these cases are representative for the whole year or just this part of the year is difficult to say. This could have been investigated further if the one year climatology was more accurate. The 25th of August case has for example too much influence on the August data in the climatology, because more of the profiles with clouds where found for this date than the other dates in August.

The results of the cloud height and temperature were compared with the cloud height and temperature data from the CALIPSO satellite during the same day, at the closest location. These comparisons were rarely ideal as the satellite often passed some distance away from ALOMAR, and rarely at the same time as the ALOMAR measurement. The CALIPSO data were yet useful as one could see the cirrus detected by the ALOMAR tropospheric LIDAR in connection with other clouds in the same area. The data showed that the cirrus clouds detected by the CALIPSO satellite often showed similar heights and temperatures as the clouds found in the ALOMAR data. The CALIPSO data has still some processing remaining, and some minor problems are connected to this. The problem that has been seen in the data used in this thesis is aerosol layers that have been wrongly classified as clouds. The ground aerosol layer has been found in the CALIPSO data from all the cases used in this thesis. It is unlikely that the high clouds identified as cirrus clouds in the CALIPSO data are aerosol layers that are wrongly classified as clouds. These clouds fit to well with the ALOMAR cloud heights and temperatures. The two ALOMAR cases that clearly were cirrus clouds, were located quite high, around 12 km and displayed temperatures down to approximately $-60°C$. The other case which was close to an altostratus cloud, was much thicker than the other clouds, close to 4 km, and the temperature range within the cloud was therefore also very large. The lowest temperatures, at the top, was as low as $-55°C$, but at the base the temperature was

$-15°C$. This temperature is high enough for supercooled water droplets to exist. However, the depolarization ratio in the fall streak structure of this cloud indicates that it is an ice cloud even though the temperatures are high enough for supercooled water at the base of the cloud. This cloud will therefore still be an ice cloud if the depolarization ratio is correct.

The optical depth was found with the 1064 nm channel. The limits between the different thicknesses of cirrus clouds from table 2.4 were used to describe the clouds. These limits are valid for the 649 nm wavelengths and are therefore not exact for 1064 nm, but have still been used as estimation. The cases with regular cirrus clouds, the 15th of August and 15th of September showed optical depths between the limit for subvisible clouds, $\tau = 0.03$, and $\tau = 1$. The cloud at the 25th of August was much thicker up to approximately $\tau = 6$ at the highest which would classify this cloud as an altostratus type cloud. Multiple scattering effects will not cause any major problems in the results from the 15th of August and the 15th of September because the optical depth was not particularly large. The 25th of August case, on the other hand, is quite thick and multiple scattering may begin to pose a problem in this case.

All the clouds in the cases displayed depolarization ratio values mostly below 0.25 and should therefore consist of plate like ice crystals. The clouds in the cases also show a tendency to have areas with horizontally oriented particles. One uncertain part of the depolarization ratio calculation was the value of the overall crosstalk factor, which could have changed since the last value. A short study about how the depolarization ratio changed when this factor changed was made, and showed that as long as the overall crosstalk factor did not change with more than the double of what it was in February 2006, it would have very little effect on the conclusions about the shape of the ice crystals. Some sort of validation of the depolarization ratio results should have been made, since they are very different from what other studies have shown. Earlier studies as the one described in Noel et al. (2002) found mostly intermediate and irregular ice crystals, but the ice crystals were almost exclusively plateshaped in this thesis. One possible explanation for this difference from other studies is measurement errors in the data used in this thesis. The tropospheric LIDAR system has experienced some technical difficulties, and this can have caused errors in the LIDAR signal recorded. The different channels are not equally strong, the 1064 nm channel is usually stronger than the other channels. The 1064 channel has therefore been used for the height calculation in this thesis. A system induced difference in strength for the recorded signal in the two 532 nm channels will be an error source for the depolarization ratio since the two 532 nm channels are used to calculate this variable. It also has to be noted that the shape classification has some limitations as it consist only of three shape categories. There exists numerous different ice crystal shapes and if the value of the depolarization ratio puts a part of the cloud in the platelike category, it does not mean that all the ice crystals in this area are hexagonal plates.

It became clear from viewing the clouds in connection with the weather situation for each case that the cirrus clouds in the ALOMAR data were mostly connected with large scale synoptic features, often some sort of occluded front. The cirrus clouds were as expected located some distance from the frontal system and clouds that are closer to the front are denser and lower.

5.1 Perspectives

A couple of methods should be changed or implemented to make further investigations. First of all the extraction of the backscattering ratio (BSR) should be improved to remove the need for the normalisation to a molecular profile. This will especially improve the automatic cloud detection which is needed for the climatology. The best way to do this is to implement either the Klett or Fernald solution of the LIDAR equation instead of just normalising the LIDAR signal to a molecular profile. This would improve the climatology greatly, because the problematic lower normalisation region is no longer needed, and the cloud detection will be done automatically more easily. The need for a molecular profile is also removed. It would also be interesting to compare the cloud detection with normalisation to a molecular profile to the cloud detection with one of the other backscatter ratio(BSR) retrieval methods. The molecular profile should then probably come from an actual measurement and not from the model profiles used in this thesis.

Another improvement would be to implement a better retrieval of optical depth or use several methods and compare them. Some method that takes a varying LIDAR ratio into consideration should be used, instead of using a constant LIDAR ratio of 20 as used in this thesis. This is a much more realistic approach as the LIDAR ratio can change within a cloud as it is strongly on the microphysics of the cloud(Cadet et al., 2005). The Molecular integration method described in Cadet et al. (2005) will be less dependent on the cloud height estimation. A comparison of this method and the Particular integration method used in this thesis could have been interesting to make with the ALOMAR data. It would also be better to use the 532 nm channel instead of the 1064 nm channel when retrieving the optical depth. The optical depth retrieved in this channel will probably be closer to the optical depth limits from the 694 nm wavelength that have been used to classify the clouds in this thesis (table 2.4 on page 21). The 1064 nm channel was still used in this thesis, because problems occurred when using the 532 nm channel. These problems were mostly linked to erroneous cloud height retrievals in the 532 nm channel.

A better comparison with the CALIPSO data should also be made, but this could possibly wait until more of the planned work has been done with the CALIPSO data. NASA has plans to extract both optical depth and depolarization ratio from the CALIPSO data along with many other parameters. This work may take some time, as the data amount from CALIPSO is very large.

Other factors that could be interesting to investigate in connection with the ice crystals in the cirrus clouds are humidity and wind speeds. Aerosol effects of the ice crystals, especially regarding the ice nuclei, would also be interesting. It would also be interesting to extract the effect of the ice crystal shape on the radiative effect of the cirrus cloud. This connection is an important factor for the improvement of cirrus cloud effects in climate models. The retrieval of the depolarization ratio should be investigated further before this is done to be certain that the correct shapes have been found.

Appendix A

Cloud classification table

The following three tables; table A.1, table A.2 and table A.3 display the cloud classification. The three étages have each their own table which give the species, varieties and other possible features for each genus. The étage of the cloud is the altitude level where it normally can be found(Dunlop, 2001)(cloud classification)[1]. The cloud can be classified as either high, medium or low. The altitude range of this level can differ with season and geographic location, but a general presentation of the étages can be found in table 2.2 in section 2.1 on page 8. A cloud can belong to one of ten basic cloud forms, and the genus describes which of the forms the cloud belongs to. The three genus that belongs to the high clouds are; cirrus, cirrocumulus and cirrostratus. A cloud can only have one genus. The next classification step is to find the species of the cloud. The species is a subcategory of the genus and is a description of the structure or shape(Dunlop, 2001)(cloud species). The cloud has only one species, as for the genus. An example of a species is the cirrus unicus, which is an easily distinguished comma shaped cirrus cloud. Another subdivision of the genus is the variety. The variety describes the clouds transparency and the arrangement of the cloud elements(Dunlop, 2001)(cloud variety). An example of a variety is Cirrus duplicatus where the cirrus cloud occur as several layers at different heights(Dunlop, 2001)(duplicatus). A cloud can have more than one variety. Additional features of the clouds can also be described, as for example precipitation. The additional features can be found in the tables under ”Accessory clouds and supplementary features”.

[1]Reference: Dictionary of Weather Dunlop (2001),specific entry in parentheses

Genus	**Species** (can only be one)	**Varieties** (can be more than one)	**Accessory clouds and supplementary features**
Cirrus	fibratus unicus spissatus castellanus floccus	intortus radiatus vertebratus duplicatus	mamma
Cirrocumulus	stratiformis lenticularis castellanus floccus	undulatus lacunosus	virga mamma
Cirrostratus	fibratus nebulosus	duplicatus undulatus	(none)

Table A.1: Classification table for high clouds

Genus	**Species** (can only be one)	**Varieties** (can be more than one)	**Accessory clouds and supplementary features**
Altocumulus	stratiformis lenticularis castellanus floccus	tranclucidus perlucidus opacus duplicatus undulatus radiatus lacunosus	virga mamma
Altostratus	(none)	translucidus opacus duplicatus undulatus radiatus	virga praecipitatio pannus mamma
Nimbostratus	(none)	(none)	praecipitatio virga pannus

Table A.2: Classification table for middle clouds

Genus	**Species** (can only be one)	**Varieties** (can be more than one)	**Accessory clouds and supplementary features**	
Cumulus	humilis mediocris congestus fractus	radiatus	plieus velum virga praecipitatio	arcus pannus tuba
Cumulonimbus	calvus capillatus	(none)	praecipitatio virga pannus incus mamma	pileus velum arcus tuba
Stratus	nebulosus fractus	opacus translucidus undulatus	praecipitatio	
Stratocumulus	stratiformis lenticularis castellanus	tranclucidus perlucidus opacus duplicatus undulatus radiatus lacunosus	mamma virga praecipitatio	

Table A.3: Classification table for low clouds

Appendix B

Scattering by particles in the atmosphere

Light from the sun enters our atmosphere constantly. This light interacts with the atmosphere and surface and it is the driving force of the dynamics of our atmosphere. How the light is scattered and absorbed influence the radiative balance and temperature of the earth. This appendix describes some aspects of the scattering of light(radiation) by the different components in the atmosphere.

When light is scattered by an obstacle in its path, there may be an exchange of energy between the light and the scattering object. The scattering is inelastic if energy is exchanged and some part of the light has undergone a shift of frequency. The scattering is elastic if there is no exchange of energy. With this can a parallel be drawn between the scattering processes and inelastic and elastic collisions in basic mechanics. The inelastic scattering is also called Raman scattering after the Indian physicist[1] who received the 1930 Nobel price in physics for the discovery of this radiational effect. Light is usually scattered elastically (Rayleigh scattering), but if the energy in the light is high enough a frequency shift and energy exchange may occur. This exchange usually results in a loss of energy in the light and an increase of internal energy in the object. This type of Raman scattering is called stokes scattering, as opposed to anti-stokes scattering where the light gains energy in the scattering process. For the purpose of the LIDAR, scattering with water molecules or N_2 may cause Raman scattering and a shift in wavelength from one of the main channels to either 387 nm/607 nm for N_2 or 408 nm/660 nm for H_2O. These are the Raman channels that can be seen in figure 3.2 at page 34.

The rest of this appendix concerns elastic forms of scattering and consider how different particles in the atmosphere scatter the light and how this can be calculated. This is however only a very short introduction to the differences between scattering of radiation by the different particles. The reader should turn to other sources, for example Liou (2002), for a longer introduction to this subject.

B.1 Scattering by molecules

Which of the scattering regimes that can be used on an atmospheric particle that is molecule, water droplet etc, depends on the size parameter. This parameter is defined in Liou

[1] Chandrasekhara Venkata Raman (1888-1970)

(2002) as $x = \frac{2\pi a}{\lambda}$, where a is the radius of the particle in question and λ is the incident wavelength. The sizes of air molecules are smaller than or equal to the wavelengths of sunlight, so the size parameter will be $x << 1$. This means that the concepts of Rayleigh scattering can be used on them. These concepts were the results of a long debate amongst 19th. century scientist about why the sky was blue(Young, 1982). Lord Rayleigh[2] was the first to connect the scattering of sunlight by molecules with the colour of the sky. He derived the following formula for the total scattered intensity of unpolarised sunlight due to a molecule(Liou, 2002):

$$I = \frac{I_0}{r^2}\alpha^2 \left(\frac{2\pi}{\lambda}\right)^4 \frac{1 + cos^2\Theta}{2} \tag{B.1}$$

Thus, the scattered intensity of the light depends inversely on the wavelength in the fourth power. When sunlight is scattered by the air molecules will therefore the light with the shortest wavelength be scattered more than the rest of the light spectrum(Liou, 2002). The blue end of the spectrum has the shortest wavelengths and this causes the blue colour of the sky. At sunsets will the light pass by more molecules to reach our eyes. This causes the shorter wavelengths to scatter away from us, and more of the light from the red part of the light spectrum reaches our eyes(Liou, 2002).

B.2 Scattering by water droplets

Water droplets are usually of sizes bigger than the wavelength of the incident light. Water droplets are also usually spherical, with the exception of falling water droplets that get deformed by the air resistance. Lorentz-Mie scattering will apply to the spherical water droplets because the size parameter will be $x \gtrsim 1$. The Lorentz-Mie theory can be used to find the exact solution to the scattering by spherical water droplets and at the base of this theory is Maxwell's equations(Liou, 2002). For a full derivation of this theory refer to chapter 5 of Liou (2002). The following equation for the scattered intensity by a particle is given in Liou (2002):

$$I(\Theta) = I_0\Omega_{eff}\frac{P(\theta)}{4\pi} = I_0\left(\frac{\sigma_s}{r^2}\right)\frac{P(\Theta)}{4\pi} \tag{B.2}$$

$$I_0\text{: incident intensity} \tag{B.3}$$

$$\text{P: Phase function} \tag{B.4}$$

$$\Omega_{eff} = \frac{\sigma_s}{r^2}\text{: effective solid angle} \tag{B.5}$$

$$\text{r: distance between scatterer and observer} \tag{B.6}$$

By the Lorenz-Mie theory can the scattering cross section be derived, and the exact scattered intensity can be found.[3] But the scattering can be approximated by easier equations when the water droplets have reached a certain size. The size of the particle is much bigger than the incident wavelength if the size parameter is $x >> 1$. The light beams can then be considered as a bundle of separate rays that each can undergo reflection and refraction within the droplet, and the principles of geometric optics can be used to find the scattering properties of the water droplets(Liou, 2002).

[2] John William Strutt,1842-1919(Young, 1982)

[3] more about this can be found in section 3.3.2 in Liou (2002)

B.3 Scattering by ice crystals

An exact solution for the scattering of light by all sizes and shapes of ice crystals does not exist. At least not for practical purposes(Liou, 2002). Some approaches do however exist to this problem. Geometric optics can be used, as for the water droplets, when the ice crystals are large enough. Optical principles, as Snell's law, can then be used on the rays that enter the ice crystal to find the refractions and reflections caused by the ice crystal(Liou, 2002). Several studies have used ray-tracing to find the radiative properties of non-spherical hydrometeors. Ray-tracing has also been used numerous times to identify the and calculate optical displays as halos or arcs(Lynch et al., 2002). The internal reflections within an ice crystal will according to ray tracing theory rotate the polarization plane and lead to depolarization(Sassen, 1991). There are several things that need to be accounted for when using ray-tracing theory to find the scattering properties of non-spherical particles. Internal absorption and polarization in the ice crystal affects how the light is scattered. The orientation and size distribution of the ice crystals will also affect this(Lynch et al., 2002). Monte Carlo method has been used as a way to trace the light within the ice crystals(Lynch et al., 2002).

The largest disadvantage with the geometric optics method is that it can only be used on ice crystals with size parameters larger than 50. The ice crystal needs to be this large before the light can be considered as bundles of individual rays(Lynch et al., 2002). Other approaches are used to find the scattering by smaller particles. One of the most widely used methods is the finite-difference time domain method. This is a numerical technique that uses appropriate absorbing boundary conditions to solve the Maxwell equations. More information about this method can be found in chapter 13 of Lynch et al. (2002) and chapter 5 of Liou (2002). As for the geometric optics approach, this method is not exact. Lynch et al. (2002) states that this method can used with reasonable accuracy for size parameters that is smaller than 20.

The theoretical foundation for scattering by non-spherical ice crystals is a work in progress, but it is unlikely that any single method that is reliable for all sizes and shapes can be found(Lynch et al., 2002). The best approach has been to use a combination of methods. A widely used approach is to combine the geometric optics and finite-difference time domain methods to the so called unified theory of light scattering. The unified theory of light scattering makes it possible to calculate the scattering and absorption from ice crystals of all sizes and shapes with an acceptable accuracy. More about the unified theory of light scattering can be found in Liou (2002) chapter 5.4.

Appendix C

Additional case analyses

This appendix includes three other case analyses that were not included in the main results. These cases were excluded because they were not as interesting as the three first cases and because additional problems were found in this cases. There are some differences in the presentation of these cases, because some parts of the analysis were changed after these cases had been excluded. These cases were made with temperature profiles from the MSIS-model and not from radiosondes. The plots in these cases were also made with an earlier version of some of the programs, and with the 532 nm channel instead of the 1064 nm channel for the height detection. The plots of the optical depth and the depolarization ratio are especially affected by this, because of the less accurate detection of height in the 532 nm channel. The optical depth is affected because the Particular integration method depends on the cloud boundary heights, and if these heights are not correct will the optical depth not be calculated correctly. The depolarization ratio was affected because the earlier version of the program that found the depolarization ratio, found just the depolarization ratio between the calculated cloud boundaries.

The reason for excluding the 28th of September case was problems with the fitting to the molecular profile. The fit between the molecular profile and the LIDAR signal was worse for the 28th of September case than for the other cases. This could lead to errors in the boundary height detection.

The 5th of October case was a very small cloud, and it was also the only cloud from this day. The molecular fit was also not perfect in the lower part of the profiles.

The 9th of October case was very noisy, and there where also some minor problems with the molecular fit in this case. The cloud was also very thin. This along with the noise problem made this case a less interesting case.

C.1 Validation and average plots of the cases

Case: September 28th. 2006

The fit for the average of the total profiles from the 28th of September is not particularly well. It is normalised between 5 and 2 km because of the thick cloud. The atmospheric profile seems to have a sharp peak in the lower dense region, which could result from aerosols, and this sharp peak can also be seen in the following next two cases. Figure C.1 shows the average plots from this day. There could be some difficulties with extracting the correct cloud heights because of the bad fit with the molecular profile . This can

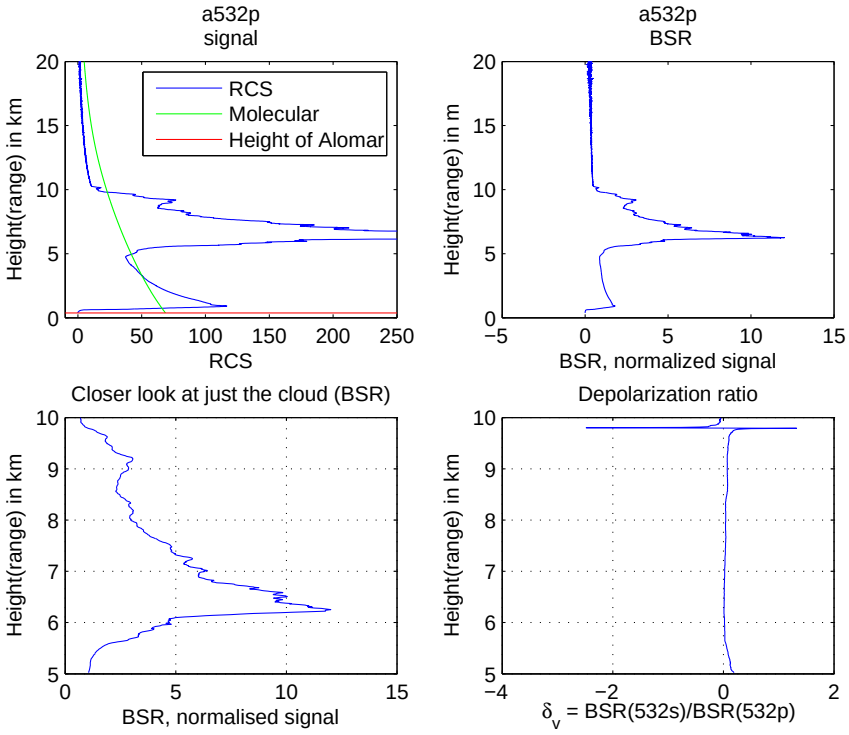

Figure C.1: Average of the files belonging to the 28th. of September case

influence the calculation of both the optical depth and the depolarization ratio. The latter is in this case influenced of a strong noise peak at approximately 10 km. The rest of the depolarization ratio is approximately zero for the rest of the cloud.

Case: October 5th. 2006

The molecular profile was in this case fitted to the lidar profiles between 9km and 4 km, but the fit in the lower 5 km is not particularly good. This could result from more aerosols in the lower km during this day. The BSR is also quite high. Its maximum value reaches almost 15 and most of the cloud has values above 5. The depolarisation ratio displays values between 0.05 and 0.1 as for the previous cases, but in this case is there a bit more variation than in the previous ones. A clear connection between the highest BSR values and the lowest depolarization ratio can not be found in the average plots. This could indicate that in this case will the ice crystals not be horizontally oriented.

Case: October 9th. 2006

The lidar signal was normalised to the molecular signal between 8 and 4 km in this case. As can be seen from both the RCS and the BSR plots in figure C.2(b), the fit in the lower 5 km is very bad. This could come from aerosols as for the other cases, but it could also result form the problems with the lidar that where discovered later in October. The fit around the cloud is ok for this case. The BSR maximum is quite low, only 1.5 and this also shows in the depolarization ratio which is mostly noise. Overall is the 9th of October not a particularly good case.

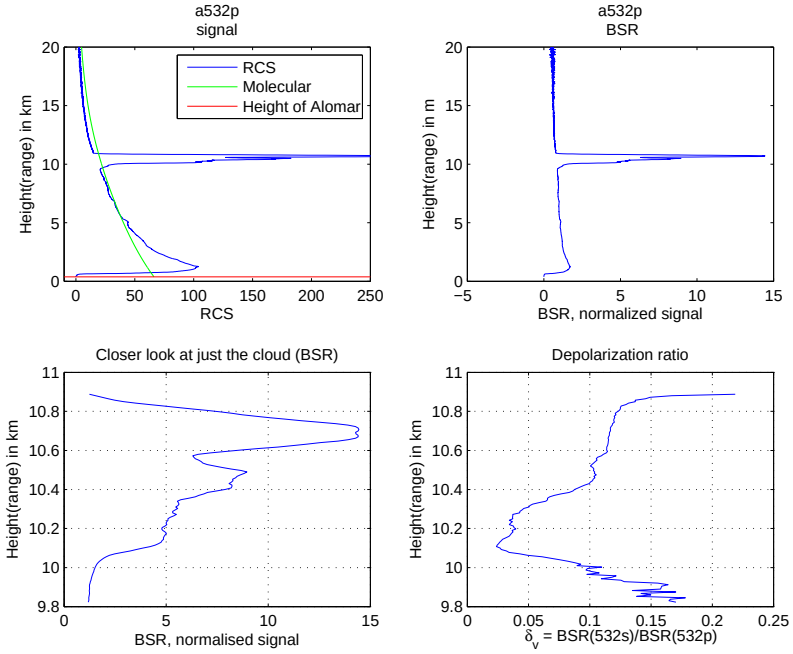

(a) Average of the files belonging to the 5th. of October case

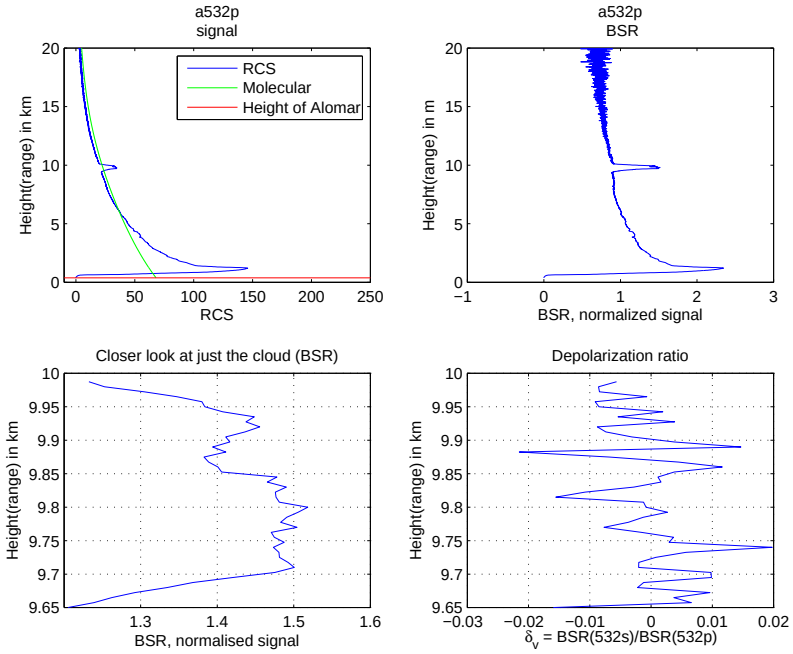

(b) Average of the files belonging to the 9th. of October case

Figure C.2: Averages

C.2 28 September 2006

C.2.1 ALOMAR data

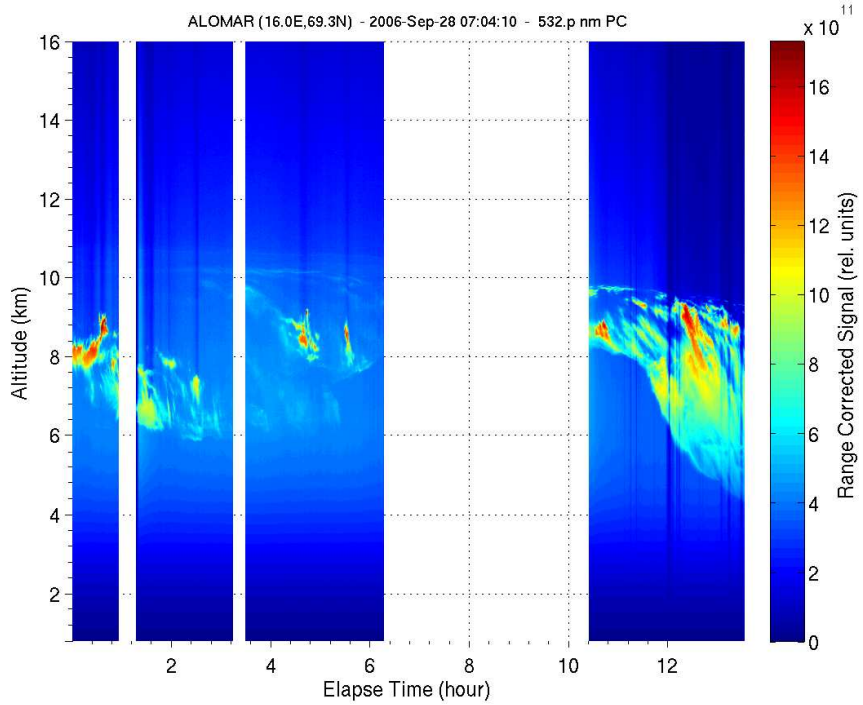

Figure C.3: Quickplot made of all measurements from 28 September 2006

The four sets of measurements from the 28th of September can be seen in figure C.3. The figure shows first some small cloud patches in the first three measurement sets. A larger cloud can be seen in the last set of measurements. This cloud is quite high and thin in the beginning of this measurement, but thickens substantially towards the end of the measurement. The focus in this case has been on this last thickening cloud. It is located between 8 and 10 km, and it seems to consist of two separate layers. After an hour the cloud begins to deepen and the final cloud base height is approximately 4 km. Some of the high and middle parts of the cloud show a strong Range Corrected Signal value, mostly between $9 * 10^{11}$ and $13 * 10^{11}$. Lower parts of the cloud have RCS values down to approximately $6(*10^{11})$. These values are the same as for the rest of the clouds at this day. The clear atmosphere has RCS values from between 0 to $5(*10^{11})$ like the other cases. The measurements were taken during the late afternoon/early evening from 17:30 to around 20:30. The problems with noise from sunlight are less than in some of the earlier cases, because the measurements are made at the afternoon and in the early fall. This cloud is deepening and the measurement was probably stopped after three hours because of this. The height at the beginning of the measurement indicates that this is a cirrus cloud, but as the cloud deepens it goes beyond the cirrus lower limit. This could indicate that the cloud begins as a cirrus cloud but it is followed by the beginning of another cloud that is too thick for the lidar to penetrate. This could therefore possibly be a cirrus cloud that is deepening to an altocumulus or altostratus cloud. A cirrus clouds that is deepening toward

an altostratus may indicate that a frontal system is moving closer to the measurement site. A frontal system that is moving closer will also bring lower, denser clouds and precipitation.

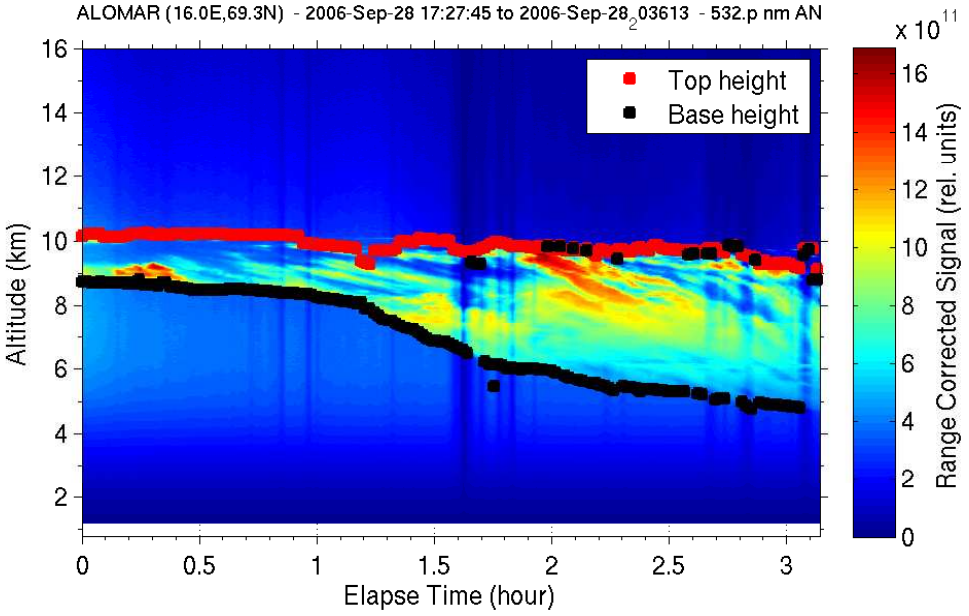

Figure C.4: Detected cloud top and base altitudes 28 September 2006

The calculated cloud heights can be seen in figure C.4. The top and the base altitudes seem to fit for most of the cloud. There are only some calculated base altitudes that are too high. The base altitudes are almost identical to the cloud top altitudes in the profiles where the base height is miscalculated. The cloud is quite high end thin during the first half hour. It is composed of two very thin layers, and the top of the upper layer is located at approximately 10 km, while the base of the lower layer is located just below 9 km. The cloud begins to deepen and becomes denser during the last two hours. The base of the cloud is at 5 km in the last profile. The top of the cloud is at approximately 9 km in the same profile, so the thickness of the cloud has reached 4 km. This very thick for a cirrus cloud and the base altitude is also very low for a cirrus cloud.

Figure C.5 displays the temperature profile from the MSIS-model. The temperature is around $-50°C$ at 10 km, which is the approximated top height of the cloud. This is a normal temperature for high cirrus clouds. The base altitude is around 8 km for the first profiles of the cloud. The temperature at this level is just above $-40°C$. The cloud base altitude sinks down to approximately 5 km for the last part of the cloud. This is below the limits originally set for cirrus clouds in the program[1], but these limits are not absolute. Clouds are dynamic and one type of cloud can often change into another of the conditions are suitable. The temperature is higher than $-30°C$ at the cloud base altitude. This could result in some supercooled water droplets within the cloud if the cloud particles are formed in this part of the cloud. However, since the temperature still is above $-20°C$ is it more likely that the cloud particles are ice crystals. The cloud particles could also have been formed in the higher, colder regions of the cloud and fall to the lower region. The ice crystals will then remain ice crystals until they reach a cloud boundary and sublimate, or altitudes with temperatures above $0°C$ where they will melt.

[1] 12km at top and 6 km at bottom

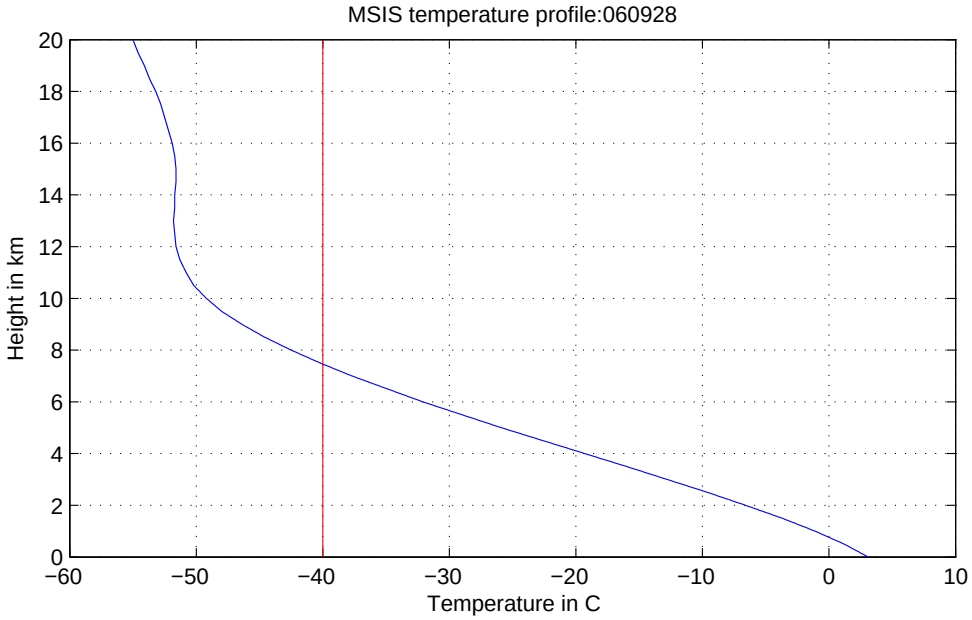

Figure C.5: Temperature profile (MSIS) 28 September 2006

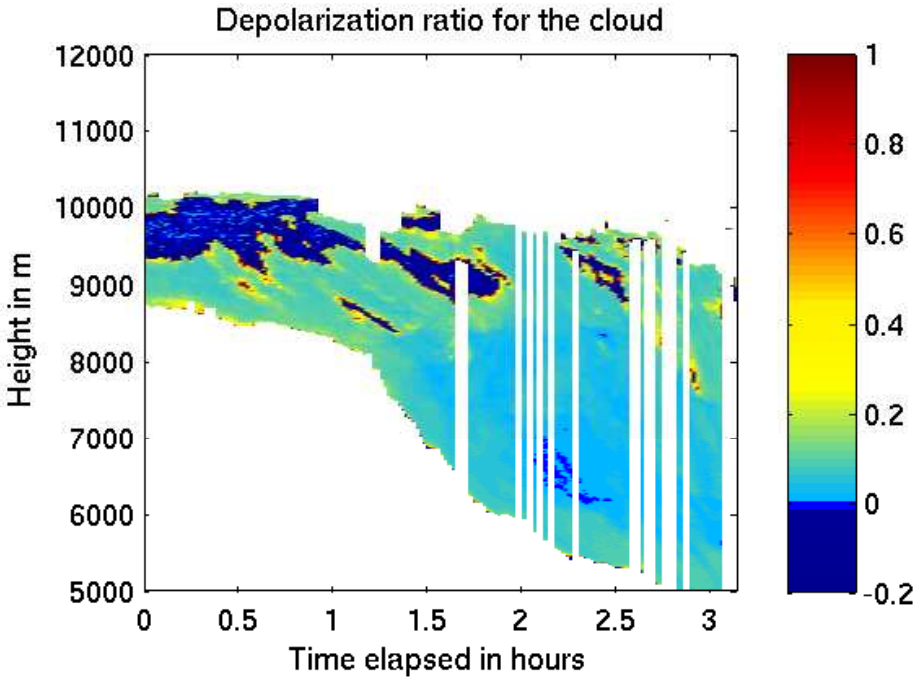

Figure C.6: Depolarization ratio for the detected cloud 28 September 2006

Figure C.6 shows the depolarization ratio of this cloud. The profiles where the height calculated is wrong are clearly visible as white stripes in the figure. Figure C.6 shows more clearly than the first figure that the cloud consists of two cloud layers in the beginning of the measurement. The top layer is only a few hundred meters thick and the bottom layer almost $\frac{1}{2}$ km thick. The clear air between these two layers can be seen as an irregular dark

blue layer when comparing figure C.6 with figure C.3. Any other colours within this layer are probably only noise. The rest of the cloud is mostly light blue or light green. These colours indicate that the value of the depolarization ratio is less than, or around 0.2. A depolarization ratio below 0.25 will indicate that the ice crystals within the cloud are plates or plate like crystals. An area(between 6 and 7 km in height) that displays depolarization ratio values at around 0 can be found between 2 and 2.5 hours into the measurement. This area does not coincide with any of the clear air areas in figure C.3. This could have been areas with horizontally oriented plates if they had coincided with areas within the cloud with a strong backscattering, or a high RCS. This however is not the case. The RCS in this area are not that high, and since the temperature in this altitude are around $-30°C$ could supercooled water droplets a better explanation of this feature. The presence of areas with super cooled water droplet may be more evidence of this cloud being a cirrus cloud that deepens to an altostratus. The middle height altostratus clouds are more likely to have water in them than the cirrus clouds.

The last figure from the ALOMAR data, figure C.7, shows the optical depth of the cloud. The profiles were the height is wrongly calculated is clearly visible as for the depolarization ratio. It is however still possible to say something about how the optical depth is changing for the cloud as it passes over ALOMAR. The optical depth of the cloud clearly below the subvisible threshold during the first hour. This is the part of the cloud which was positively classified as cirrus. The optical depth of the cloud increases during the last two hours. A maximum occurs approximately 2.5 hours into the measurement. The optical depth of the cloud is then above 0.8. Table 2.4 in section 2.3.2 displays the different types of cirrus clouds according to the optical depth. This table classifies this cirrus cloud as an opaque cirrus cloud, but not yet an altostratus. The table states that the optical depth must be above 3.0 for the cloud to be classified as an altostratus. This means that this cloud can not be classified as an altostratus yet. This cloud may have deepened to an altostratus later during this day, since the measurements were stopped after this measurement because the cloud became too thick for the Lidar to penetrate.

C.2.2 CALIPSO data

The CALIPSO satellite made two close passes during this day, the first was a night measurement and the other was a daytime measurement. The first set of profiles was made at around 03:00 and the other set were made around 11:00. There is only half an hour that separates the closest position in time and the closest position in space for the 03:00 measurement. However, the difference in the distance between the satellite measuring location and the ALOMAR location quite large because of the high velocity of the CALIPSO satellite. The closest position in space is also above 400 km. The time difference between the ALOMAR measurements and the CALIPSO measurements are much lower for the second set of measurements, around 11:00. The closest position in time is also much closer, only 120 km, and this set of profiles have been used to make the following plots.

The first plot in figure C.8 is a plot of path the satellite made during this case. As for many of the cases in this thesis would it have been more ideal if the passing was closer. A comparison between some of the measurements from the two instruments has still been made.

Figure C.8(b) displays the cloud heights from the CALIPSO data in addition to the tropopause height. The aerosol layer by the ground is less dominant in this figure than for

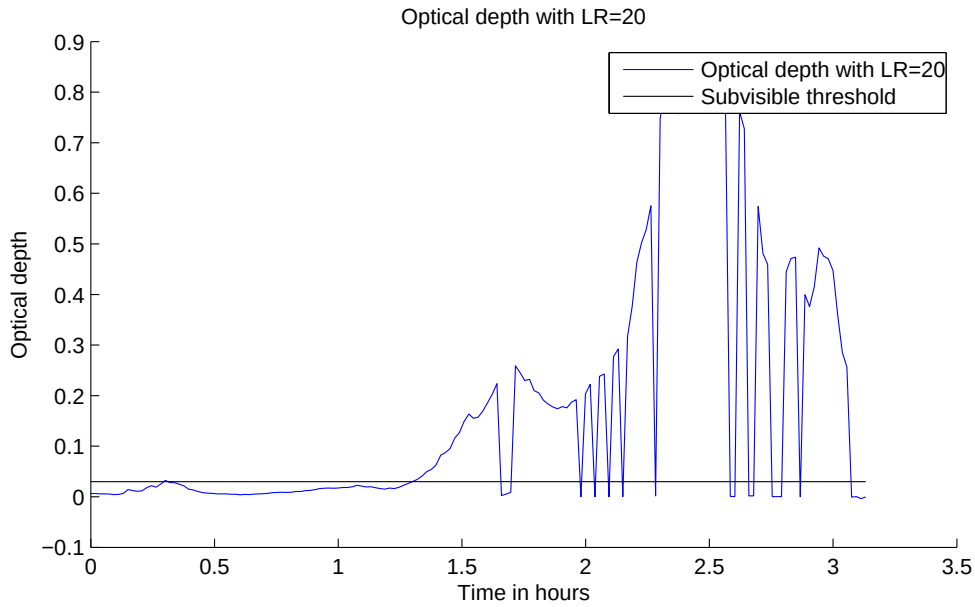

Figure C.7: Optical depth of detected cloud 28 September 2006

the other cases, especially in the areas with the most clouds. This could be because less of the laser light is reflected off the aerosol layer because of attenuation of the beam by the overlying clouds. There are quite a lot of clouds in this plot and some of them are too low to be classified as cirrus clouds. The most interesting cloud is located around 69°N and is therefore the closest in space to the ALOMAR measurement.

This cloud is located close to the tropopause and stretches from around 9 km down to approximately 7 km. The temperature for this and all the other clouds identified as cirrus clouds can be found in figure C.8(c). The cloud closest to ALOMAR displays temperatures from around $-37°C$ to almost $-50°C$. This cloud is therefore clearly an ice cloud.

It can be seen, when comparing with the ALOMAR data, that these two clouds exhibit approximately the same top altitude. However, the ALOMAR cloud deepens much more than the CALIPSO one. The temperatures for the two clouds are also very similar. The deepening cloud in the ALOMAR data can also be seen in connection with the other clouds that can be seen in figure C.8(c). The rest of the clouds are quite large but still as high as most cirrus. They also exhibit quite low temperatures. These clouds could be cirrus clouds that are deepening to altostratus clouds as was the previous hypothesis for the ALOMAR cloud.

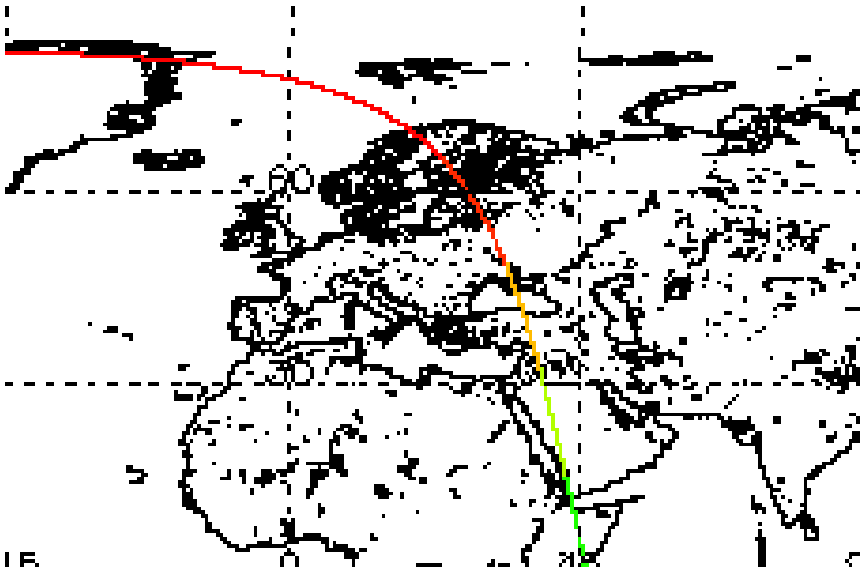

(a) Geolocated path of the CALIPSO satellite during the measurement used in this case

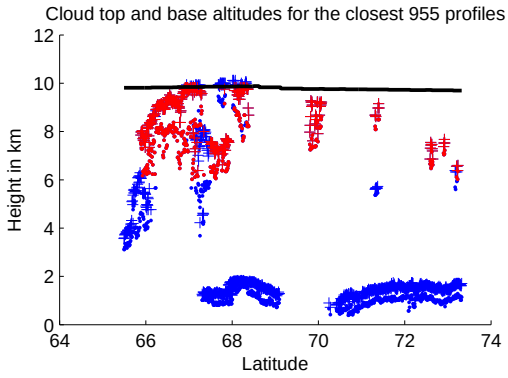

(b) Clouds found in the closest CALIPSO profiles. Crosses are cloud top heights and dots are cloud base heights. Red crosses and dots are probable cirrus clouds(altitudes between 6000m and tropopause height) blue crosses and dots are other features, presumably clouds. Black line indicates the tropopause height.

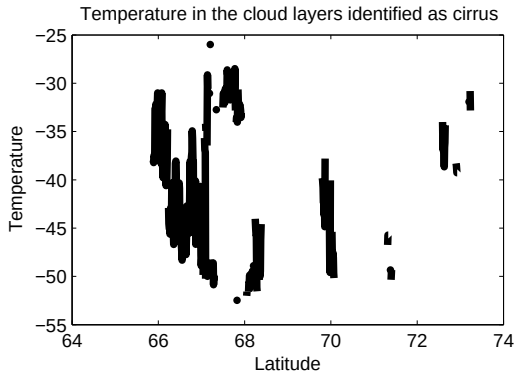

(c) Temperature for the clouds in The CALIPSO data

Figure C.8: CALIPSO results of the 28 September case

File	CAL_LID_L2_01kmCLay-Prov-V2-01.2006-09-28T02-51-40ZN.hdf	
	Closest in time	closest in space
time	03:37:49	02:54:11
latitude	-81.01N	70.89N
longitude	-93.61.V	6.90V
distance (km)	17794.54 km	406.65 km
time difference (s)	55399s	58017 s
time difference (h)	15.39 h	16.12 h
File	CAL_LID_L2_01kmCLay-Prov-V2-01.2006-09-28T10-13-26ZD.hdf	
	Closest in time	closest in space
time	11:01:48	10:58:38
latitude	79.20N	69.49N
longitude	-91.70V	18.73V
distance (km)	2934.64 km	121.21 km
time difference (s)	28520s	28950 s
time difference (h)	7.92 h	8.04 h

Table C.1: This table gives the time, latitude and longitude of the profile closest to the ALOMAR location, and the profile closest to the time of the ALOMAR data used in this case. The middle profile in the ALOMAR data is used for the last calculation. In addition are the calculated differences in time, both in seconds and hours, and distance given for both possible files.

C.3 05 October 2006

C.3.1 ALOMAR data

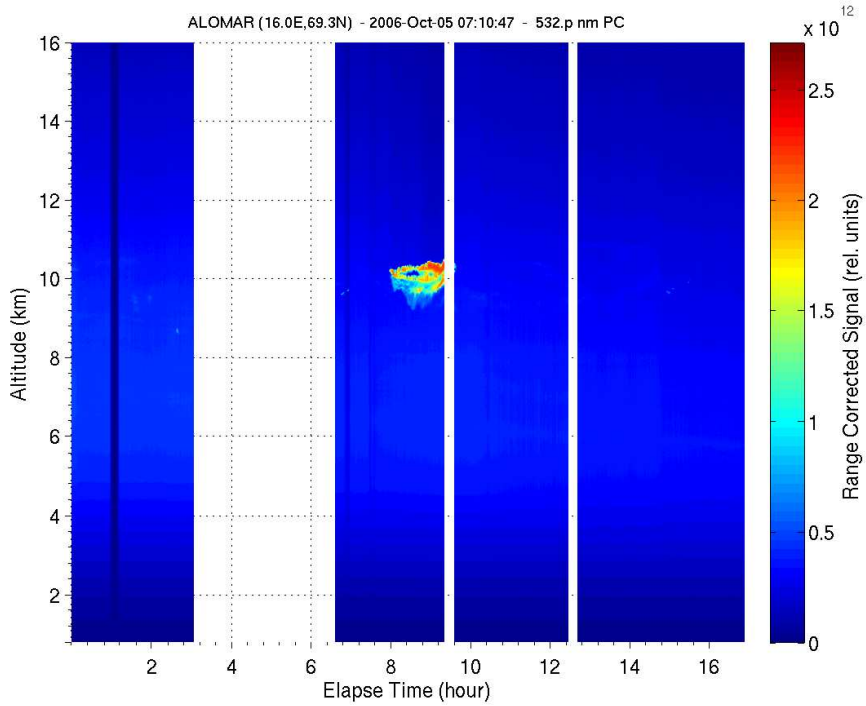

Figure C.9: Quickplot of all measurements from 05 October 2006

Four sets of measurements were taken at the 5th of October. The sky was mostly clear, but in the second set of measurements, around 13:30 a small cloud appears around 10 km. This cloud has a maximal RCS return at above $2(*10^{12})$, and the clear air has a RCS below $0.5(*10^{12})$. Noise could be an issue since this is daytime measurements. The following figures and discussion considers the cloud in the second set of measurement. This cloud is very small and only covers the lidar for approximately 2 hours. This cloud is high enough to be classified as a cirrus cloud and it is also thin enough to be penetrated by the LIDAR laser beam.

The calculated heights of the cloud can be seen in figure C.10. The fit of the heights to the cloud seen in the Quickplot is fairly good except for one profile in the first small cloud patch and for the base altitude in the last profiles. These miscalculations probably came from noise issues. It could also result from when the profile where fitted to the molecular signal. The heights can be found too high or too low when this normalisation is not good enough.

The height of the main part of the cloud is between 10 and 11 km. An approximate temperature of cloud can be found when comparing this to the temperature profile in figure C.11. This temperature is just around $-50°C$ and the cloud clearly classifies as an ice cloud. The cloud seems to be quite dense even though it is quite thin, it is only around 1 km at its thickest as for many of the other cases. The optical depth could therefore exceed subvisible values for some parts of the cloud.

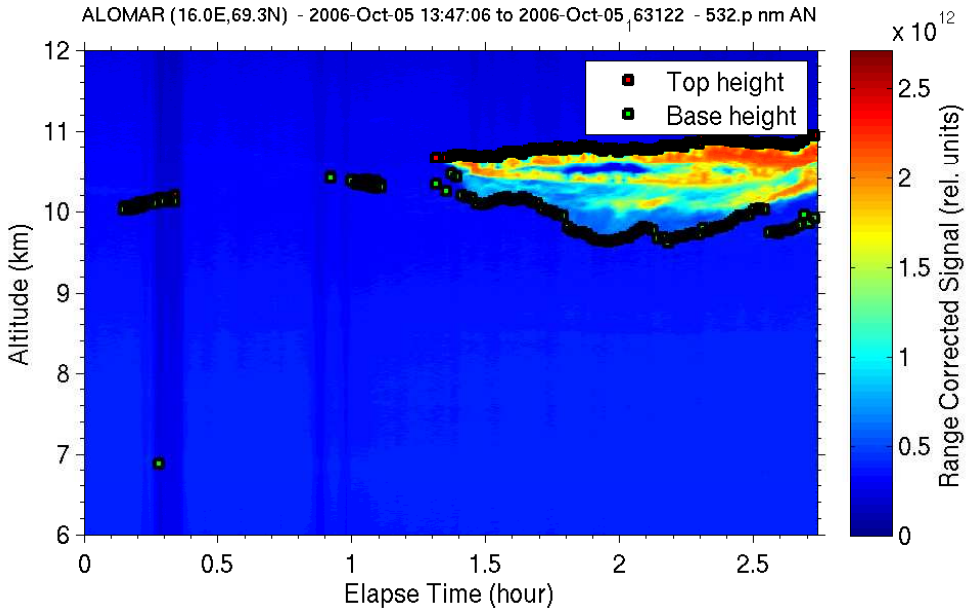

Figure C.10: Detected cloud top and base altitudes 05 October 2006

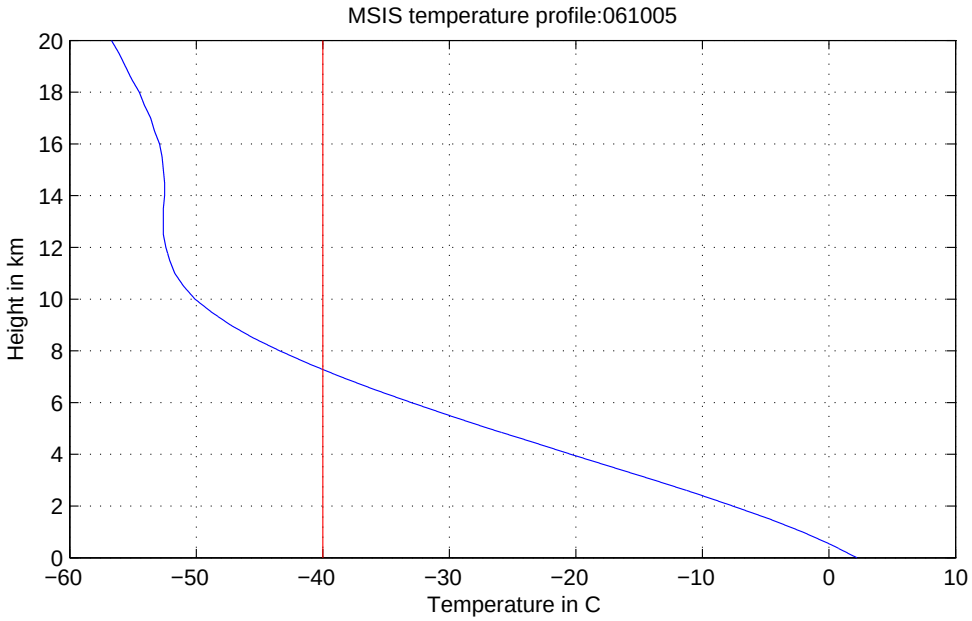

Figure C.11: Temperature profile (MSIS) 05 October 2006

The crystal shapes of this cloud can be found from the depolarization ratio in figure C.12. The depolarization ratio is mostly around 0.1 in the main cloud. There is however some areas with depolarization ratio close to 0. The area closest to the top of the cloud coincides with the clear atmosphere area that can be seen in figure C.9. The calculated bottom altitude of the cloud is a bit lower than the actual altitude for the last profiles as mentioned for figure C.10. This explains the depolarization ratio of approximately zero in this area which arises because of clean air. These two areas should have been dark blue

if there was no noise. But the noise is more visible in the clean air, as small patches of other colours, because the noise is a bigger part of the clear air data than for the cloudy part of the data. The two other parts of the main cloud with close to zero depolarization ratios do not coincide with any clear air. Figure C.12 must be compared with figure C.10 to decide whether they are areas with super cooled water droplets or horizontally oriented ice crystals. This comparison shows that the two areas in question coincide with areas in figure C.10 with a strong backscattering. But these areas are not the ones with the highest backscattering. The highest backscattering can be found in the higher parts of the cloud. This disconnection between the strongest backscattering and the lowest depolarization ratio was also seen in section 4.2.3. Figure C.2(a) in this section showed a much higher backscattering in the higher parts of the cloud than in the heights where the depolarization ratio was lowest. This makes the assumption that the low depolarisation ratio is caused by horizontally oriented ice crystals much more difficult to make. The high altitude and therefore low temperature of the cloud suggests that the cloud should not include any super cooled water. The rest of the cloud shows depolarization ratio values below 0.2 and will therefore probably consist of plate-like ice crystals, which are easily horizontally aligned. The areas with close to zero depolarisation are located close to the lower edge of the cloud. As described in figure 2.8 in section 2.3.2 will probability for the ice crystals to orient themselves horizontally change with the sizes of the ice crystals. For newly formed small ice crystals will Brownian motions randomize their orientation. This can account for the depolarization ratio >0 in the top part of the cloud. The horizontally oriented ice crystals in the middle of the cloud would have reach a size at which the Reynolds number in the flow around them will be between 20 and 200 (see figure 2.8). They will then orient themselves horizontally as the eddies in the rear of the ice crystals holds their fall pattern steady. Several effects will tend to counteract the horizontal orientation in the lower part of the cloud. Some of the ice crystals may have reached sizes where the Reynolds number has become too large to keep the crystals steady. Sublimation of the crystals at the edge of the cloud can also change the orientation of the ice crystals, because of changes in size and shape of the crystals. Turbulence created by the cooling created by the sublimation will also randomize the orientation of the ice crystals.

The areas with the lowest depolarization ratio are very small, as can be seen from figure C.12. This can explain some why the average shows a low BSR in the lower area of the cloud in figure C.2(a). The profiles which neither shows low depolarization ratio nor high backscattering in their lower parts tend to counteract the profiles that do show such values when an average is made. The upper part of the cloud shows high backscattering in all the profiles. The average will then show high values in this altitude too. One must suspect that this cloud consist of ice because of its high base altitude and low temperature. The only explanation that remains for the low depolarization ratio is then horizontally orientation of the ice crystals.

It can be seen from figure C.13 that the optical depth of this cloud is quite low. It does not exceed 0.16 for any part of the cloud. The optical depth is above the subvisible threshold for the main part of the cloud. The cloud should therefore have been visible from the ground even though it was quite thin. The optical depth of the cloud increases gradually from below subvisible levels at the arrival of the main cloud until the measurements are stopped and the optical depth reach its maximal value. The thickness of the cloud on the other hand does not show a similar development. The thickness of the cloud is between 0.5 km and 1 km with the maximal thickness in the middle of the main cloud approximately

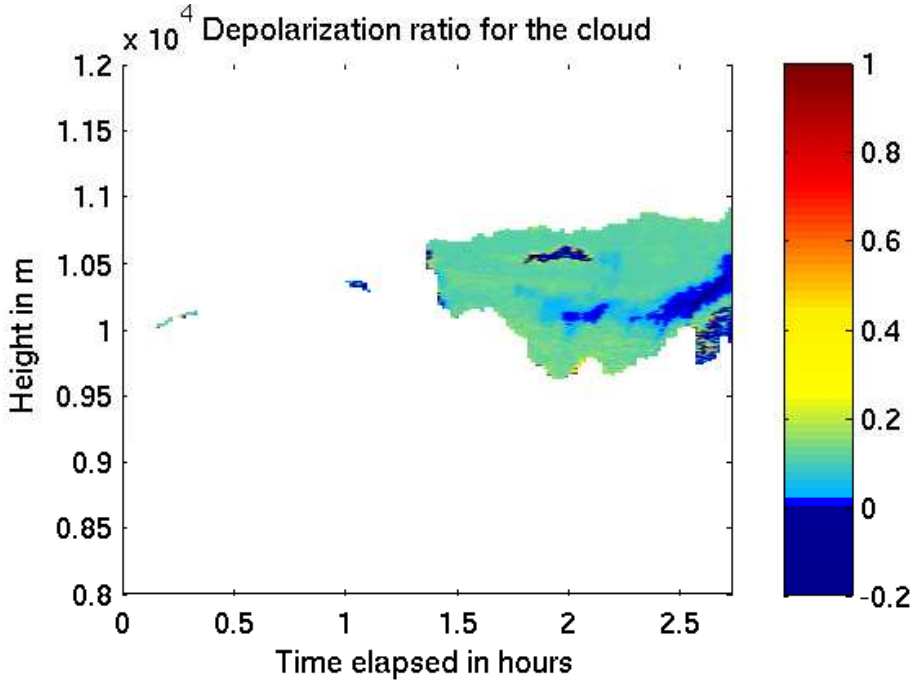

Figure C.12: Depolarization ratio for the detected cloud 05 October 2006

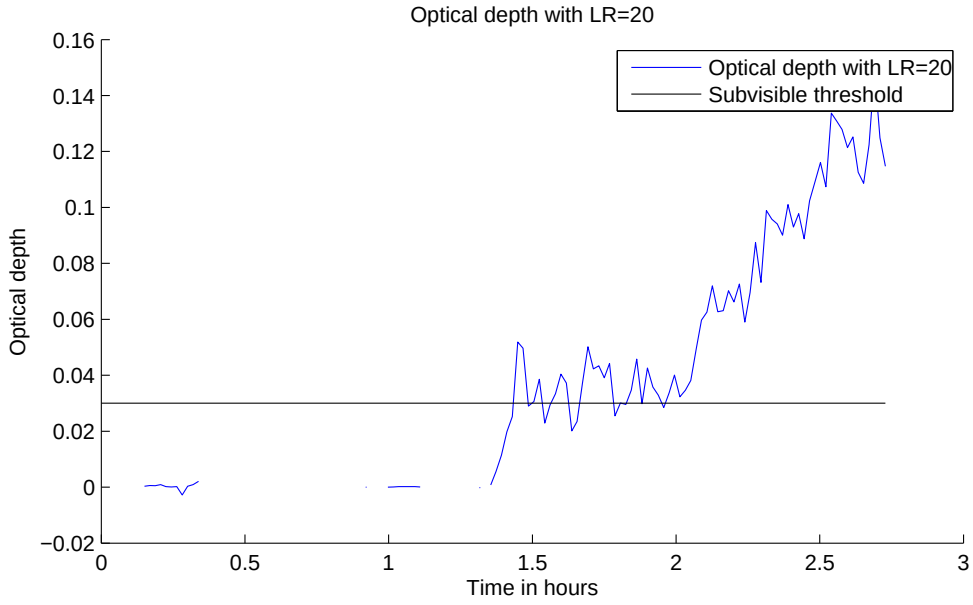

Figure C.13: Optical depth of detected cloud 05 October 2006

2 hours into the measurements. When the cloud is at its thickest is the optical depth actually very close to the subvisible limit. The optical depth begins to increase just after the thickest part of the cloud has passed. This could indicate that the last part of the cloud is much denser than the first part of the cloud. This also seems likely from figure C.10 where the RCS is much stronger during the last two hours of measurements. The high altitude, low depolarization ratio and low temperature all indicate that this cloud is

a regular cirrus cloud.

C.3.2 CALIPSO data

The CALIPSO satellite made two passes during this day. The first one passed over ALOMAR at around 03:00 and the other around 11:00. The information about the closest profiles from these two passes can be found in table C.2. From this table can it be seen that the first passing was around 12 hours before the ALOMAR measurements. The closest profile in space was also more than 450 km from the ALOMAR location. The second passing other hand, was only about 4 hours before the ALOMAR measurement time, and the closest position in space was only 66 km from the ALOMAR location. When viewing the closest profiles from this day, it was found that the profiles from around 11:00 did not display any cirrus. These profiles could therefore not be used in a comparison with the ALOMAR data. The 03:00 data have therefore been used to make the following plots, even though the passage was much further from ALOMAR both in time and location.

File	CAL_LID_L2_01kmCLay-Prov-V2-01.2006-10-05T10-18-48ZD.hdf	
	Closest in time	closest in space
time	11:11:20	11:04:45
latitude	80.56N	69.26N
longitude	-82.16.V	17.50V
distance (km)	2695.31 km	66.25 km
time difference (s)	14191 s	14586 s
time difference (h)	3.94 h	4.05h
File	CAL_LID_L2_01kmCLay-Prov-V2-01.2006-10-05T02-57-02ZN.hdf	
	Closest in time	closest in space
time	03:43:11	03:00:17
latitude	-79.44N	71.18N
longitude	-80.19V	5.82V
distance (km)	17508.93 km	456.30 km
time difference (s)	41080s	43654 s
time difference (h)	11.41 h	12.12 h

Table C.2: This table gives the time, latitude and longitude of the profile closest to the ALOMAR location, and the profile closest to the time of the ALOMAR data used in this case. The middle profile in the ALOMAR data is used fro the last calculation. The calculated differences in time, both in seconds and hours, and distance are also given for both possible files.

The path of the satellite for the chosen set of measurements can be seen in figure C.14(a). All the profiles used in this case lie within this path and a 500 km radius from the ALOMAR site.

There are two interesting clouds in the figure C.14(b). The first one by approximately 71°N is situated right at the tropopause between 10 and 11 km and some of the cloud is therefore not identified as cirrus, since the top altitude is above the tropopause level. The

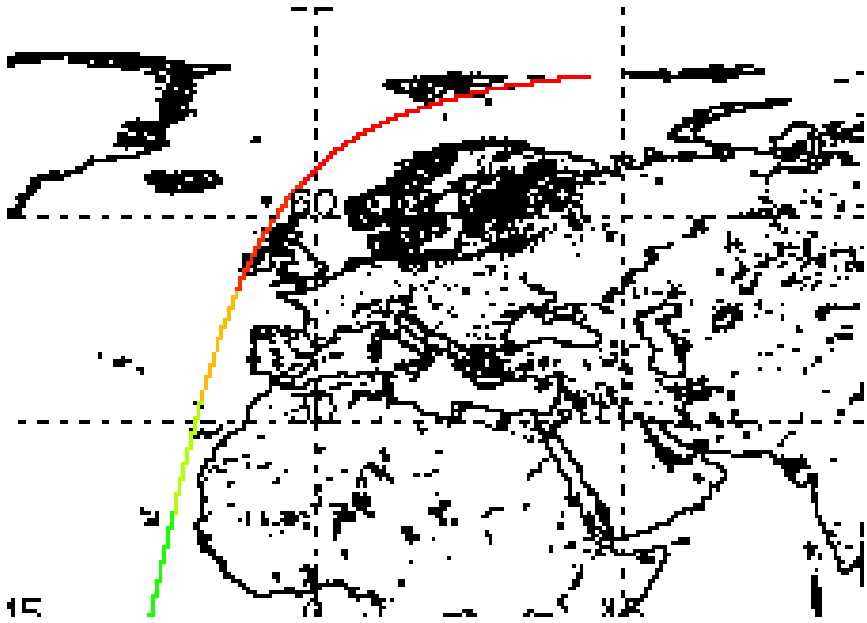

(a) Geolocated path of the CALIPSO satellite during the measurement used in this case

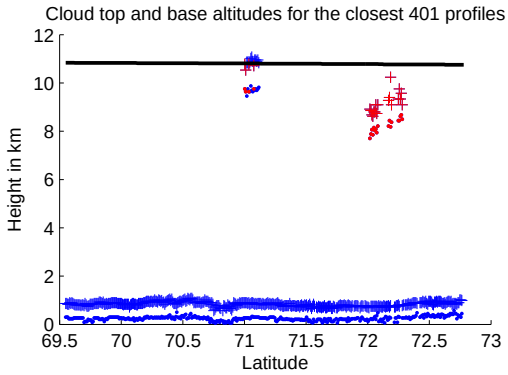

(b) Clouds found in the closest CALIPSO profiles. Crosses are cloud top heights and dots are cloud base heights. Red crosses and dots are probable cirrus clouds(altitudes between 6000m and tropopause height) blue crosses and dots are other features, presumably clouds. Black line indicates the tropopause height.

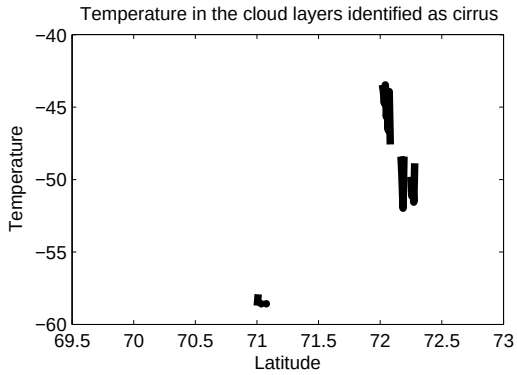

(c) Temperature for the clouds in The CALIPSO data

Figure C.14: CALIPSO results of the 05 October case

thickness of this first cloud is just above 1 km. The second cloud seems somewhat bigger and is situated between 10 and 8 km, just below the tropopause. The temperature of both clouds is very low as can be seen from the temperature in figure C.14(c). It is almost as low as $-60°C$ for the first and highest cloud, and the other cloud displays temperatures between $-43°C$ and $-53°C$.

There is no doubt that these clouds are ice clouds as for the cloud found in the ALOMAR data. The vertical extent of the CALIPSO clouds is also quite similar. They are both located around 10 km and are around 1 to 2 km thick.

C.4 09 October 2006

C.4.1 ALOMAR data

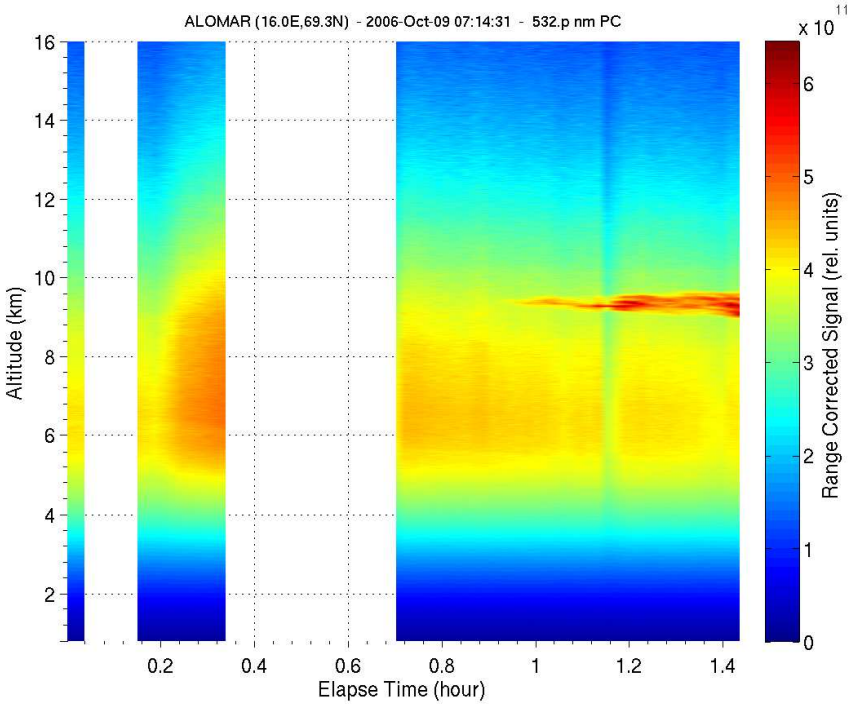

Figure C.15: Quickplot of all measurements from 09 October 2006

The measurements from this day are a bit noisy, and this affects the results. Three sets of measurements were made during this day, but just for a short period of time. It is only 1.4 hours between the start of the first measurement and the end of the last, as can be seen from figure C.15. The atmosphere where mostly clear during these measurements, but during the last set of measurements a thin cirrus layer appears around 10 km. The cloud displays a RCS from approximately $4(*10^{11})$ up to about $6(*10^{11})$. The clear atmosphere displays RCS in the range 0-4.5$(*10^{11})$ because of noise and this may pose a problem when trying to extract the cloud information from the data. The noise in this case is probably mostly noise coming from the system, because the measurements are made early in the morning during October. The atmospheric noise should therefore be relatively low. The noise issue in this case has also been discussed in section 4.2.3. The focus in this case will be on the cloud in the last set of measurements. This is probably a regular cirrus cloud as for the other thin clouds found in the ALOMAR data.

This cloud is quite thin as can be seen from the figure C.16. It is less than 1 km thick at the thickest point of the cloud. But most of the cloud is much thinner than this. The heights that have been calculated fit fairly well with the cloud in the figure, with the exception that some of the thinnest parts have not been detected. These parts are so thin that they have probably been misinterpreted as noise. The height calculations should overall be good enough to not make any major errors in the depolarization and optical depth calculations.

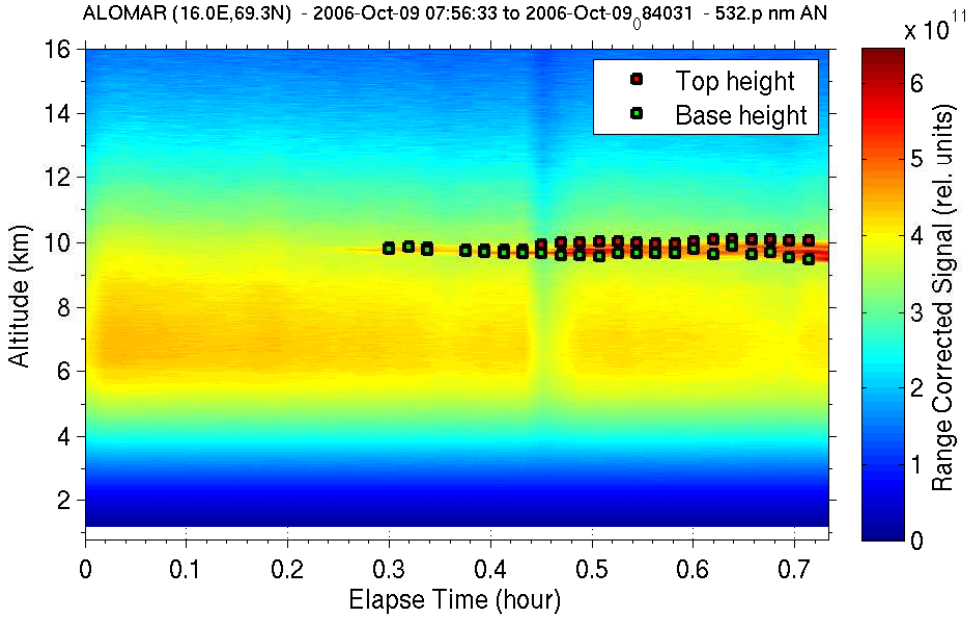

Figure C.16: Detected cloud top and base altitudes 09 October 2006

Figure C.17 displays the temperature profile for this day. The threshold for homogeneous nucleation is reached at approximately 7 km, as for most of the temperature profiles. The cloud can be found at 10 km. The temperature in this height is $-50°$ if the MSIS-model temperature is correct. This cloud would therefore clearly be an ice cloud. This is therefore clearly a regular cirrus case because of its high altitude. A low depolarization ratio can be expected, because the cloud is so thin.

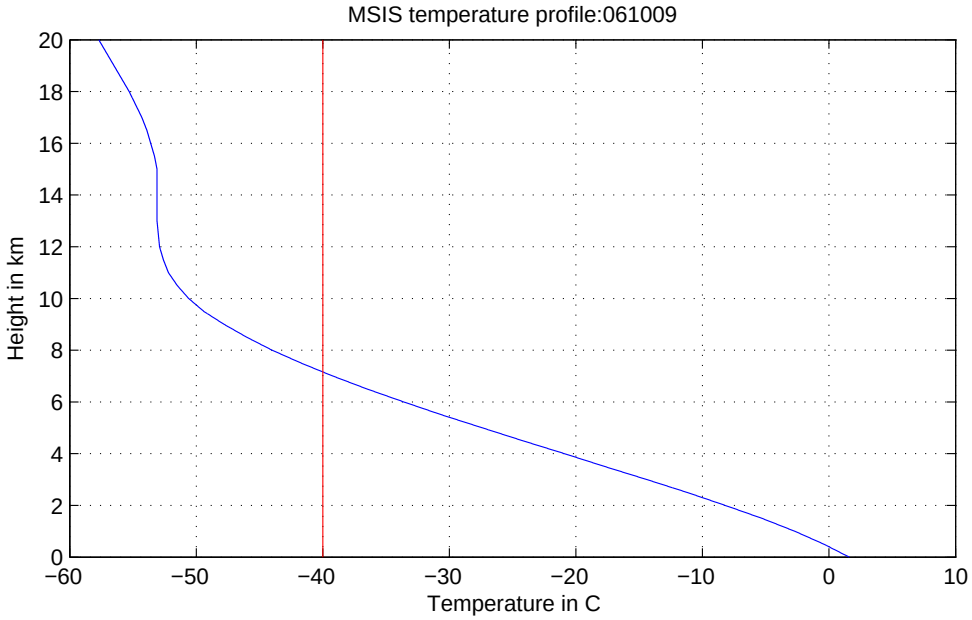

Figure C.17: Temperature profile (MSIS) 09 October 2006

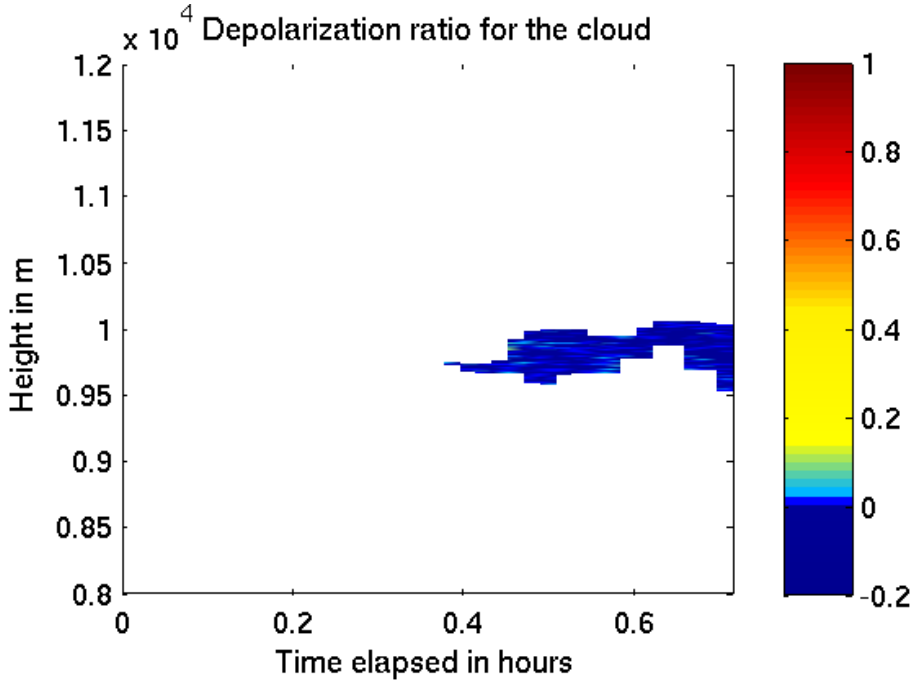

(a) Depolarization ratio for the detected cloud 09 October 2006

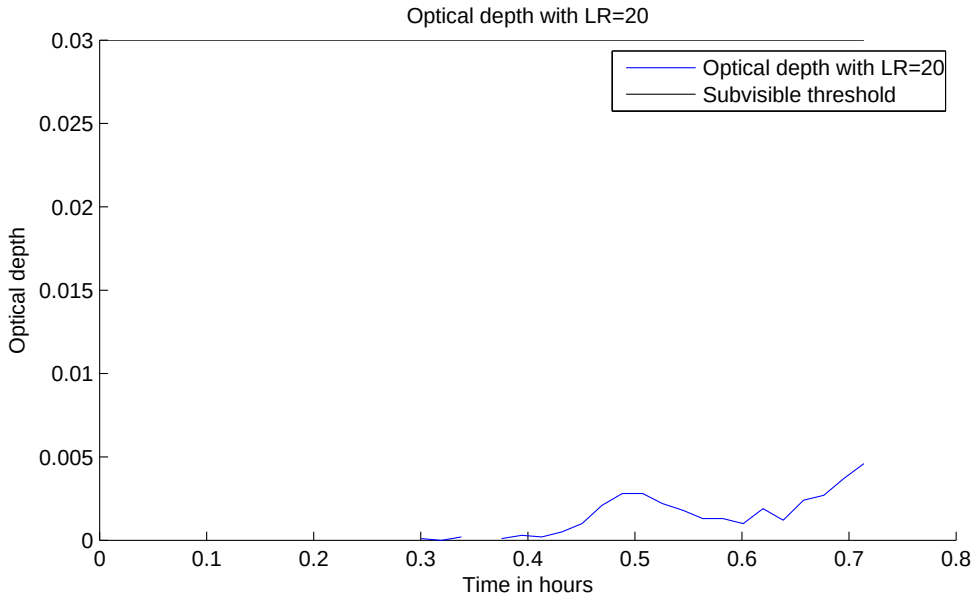

(b) Optical depth of detected cloud 09 October 2006

Figure C.18: Microphysical properties of the cirrus cloud in this case

The depolarization ratio for this cloud is mostly around zero. But this day is very much influenced by the noise in the data. The depolarization ratio is easily affected by any noise in the data as can be seen from the earlier discussions. Clouds that is as thin as this one will be more influenced by the noise than the thicker clouds. This is because the thicker clouds scatter more of the light and they are therefore easier to extract from the data. The low depolarization ratio and low temperature indicates that this cloud could be consisting of horizontally oriented ice crystals. The calculation of the depolarization ratio could have been too much affected by the noise to give reliable results, since none of the other clouds have shown indications of consisting only of horizontally oriented ice crystals.

The optical depth was as expected very low for this cloud. Figure C.18(b) shows that the depolarization ratio is well below the subvisible threshold. The depolarization ratio never exceeds 0.005 in this case. The noise levels in the data may have affected this value too. Noise issues could have been an important problem when concerning the calculation of the height of the cloud, because the heights are very important for the calculation of the optical depth. This cloud is a cirrus cloud because of its thin nature and high altitude, but more than this is difficult to say because of the noise problems in this case. As previously mentioned, these noise problems came from alignment problems with the LIDAR which led to the stop in measurements from November 2006 to March 2007.

C.4.2 CALIPSO data

There were two passes, as for most of the other cases, by the CALIPSO satellite during this day. The first one was around 03:00 and the other around 10:30. From table C.3 can it be seen that the time difference between the ALOMAR measurements and the 03:00 CALIPSO measurements is around 5 hours. This is not bad, but the other CALIPSO passing is closer in time with only around 2 hours of difference between the middle measurement of the ALOMAR measurement and the CALIPSO measurement. The closest position in space is not that different between the two passes. The first one is around 250 km and the other one is just above 280 km. The 03:00 measurements were used to make the following plots, but the other set of measurements could just as well have been used.

Figure C.19(a) gives the path of the CALIPSO satellite. High clouds were only detected in a small number of closest 851 profiles. This can be seen in figure C.19(b) where also a lower aerosol layer can be found. The small cloud that can be identified as cirrus is on the edge of the plot, and the cloud is therefore not particularly close to ALOMAR, but lies within the 500 km limit. The cloud is located between 66 and 67°N, and is situated between 8 and 10 km, with a thickness of approximately one km. The temperature of this cloud can be found in figure C.19(c), which shows a very cold cloud with temperature between $-47°C$ and $-48°C$.

How does this compare with the ALOMAR data? The cloud found in the ALOMAR data was of similar height as the one found in the CALIPSO data. Both clouds where located around 10 km. The temperature of the ALOMAR cloud was found to be around $-50°C$ which also is close to what was found for the CALIPSO cloud. The measurements were made with only around 5 hours difference which is quite close in time, the distance between the ALOMAR location and the location of the CALIPSO measurement on the other hand, was quite large. A discussion of whether these two clouds are the same cloud system or not could have been made if information about the wind velocity were available. This is however not the case, but would have been interesting to investigate. The two

File	CAL_LID_L2_01kmCLay-Prov-V2-01.2006-10-09T02-31-49ZN.hdf	
	Closest in time	closest in space
time	03:18:01	02:35:53
latitude	-78.38N	70.08N
longitude	-67.82V	10.34V
distance (km)	17218.95 km	251.12 km
time difference (s)	17964 s	20492s
time difference (h)	4.99 h	5.69 h
File	CAL_LID_L2_01kmCLay-Prov-V2-01.2006-10-09T09-53-35ZD.hdf	
	Closest in time	closest in space
time	09:53:34	10:40:19
latitude	-78.44N	70.24N
longitude	-166.99V	22.32V
distance (km)	18947.05 km	282.13 km
time difference (s)	-5769 s	-8574 s
time difference (h)	-1.60 h	-2.38 h

Table C.3: This table gives the time, latitude and longitude of the profile closest to the ALOMAR location, and the profile closest to the time of the ALOMAR data used in this case. The middle profile in the ALOMAR data is used for the last calculation. The calculated differences in time, both in seconds and hours, and distance are also given for both possible files.

clouds look somewhat similar. They have similar heights, thicknesses and temperatures. This could indicate that they at least where formed under much of the same conditions.

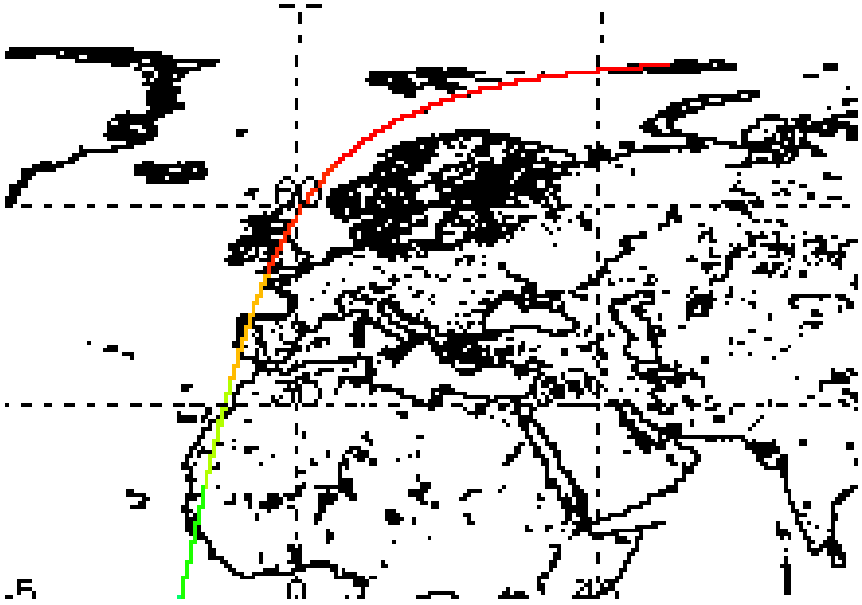

(a) Geolocated path of the CALIPSO satellite during the measurement used in this case

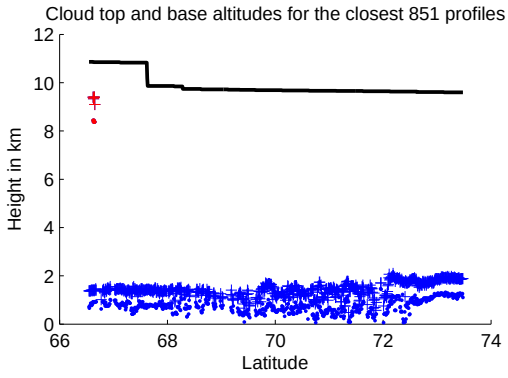

(b) Clouds found in the closest CALIPSO profiles. Crosses are cloud top heights and dots are cloud base heights. Red crosses and dots are probable cirrus clouds(altitudes between 6000m and tropopause height) blue crosses and dots are other features, presumably clouds. Black line indicates the tropopause height.

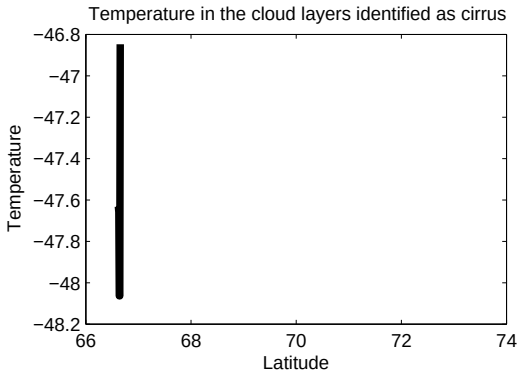

(c) Temperature for the clouds in The CALIPSO data

Figure C.19: CALIPSO results of the 09 October case

Bibliography

Alcorn, Marion (2007) *H*igh Level Clouds. URL: http://www.met.tamu.edu/class/Metr304/Exer10dir/highclouds.html. Texas A&M University, Accessed: 19.01.08.

Alomar (2006a) *A*lomar User Guide: Arctic Lidar Observatory for Middle Atmosphere Research. ALOMAR, Arctic Lidar Observatory. Revised Januar 2007.

Alomar (2006b) *T*ropospheric lidar: overview of data processing and first results. Max Frioud/Michael Gausa, by personal communication.

Arntzen, Ruth and Lystad, Sofus (2006) *R*adiosonde data fra norske radiosondestasjoner. Web: http://noserc.met.no/DS/radiosonde.html. Accessed: 12 April 08.

AVHRR (2008) *N*EODAAS The AVHRR Sensor. web: http://www.sat.dundee.ac.uk/avhrr.html. Accessed: 14 April 2008.

Bailey, M. and Hallett, J. (2002) *N*ucleation effects on the habit of vapour grown ice crystals from -18 to -42 C. Quartery Journal of the Royal Meteorological Society, Vol. 128(583): p. 1461–1483.

Biele, Jens; Beyerle, Georg and Baumgarten, Gerd (2000) *P*olarization lidar: Corrections of instrumental effects. Optics Express, Vol. 7(12): p. 427–435.

Cadet, Bertrand; Giraud, Vincent; Haeffelin, Martial; Keckhut, Philippe; Rechou, Anne and Baldy, Serge (2005) *I*mproved retrievals of the optical properties of cirrus clouds by a combination of lidar methods. Applied Optics.

Committee, The Norwegian Nobel (2007) *T*he Nobel Peace Price for 2007. http://nobelpeaceprize.org/eng_lau_announce2007.html. (Accessed:17.01.08).

Currey, J.Chris (2006) *C*loud - Aerosol LIDAR Infrared PathFinder Satellite Observations: Data Management System, Data Products Catalog. Technical Report version 2.3, NASA. URL: http://www-calipso.larc.nasa.gov/products/CALIPSO_DPC_Rev2x3.pdf accessed: 06.02.08.

Dunlop, Storm (2001) *D*ictionary of Weather. Oxford Paperback Reference (Oxford University press). Reissued 2005.

Frioud, Max (2003) *A*pplication of Backscatter Lidar to Determine the Aerosol Distribution above Complex Terrain. Ph.D.thesis, Observatoire Cantonal de Neuchâtel - Université de Neuchâtel.

Frioud, Max; Gausa, Michael; Baumgarten, Gerd; Kristjansson, Jon Egill and Føre, Ivan (2006a) *N*ew Troposphere LIDAR system in operation at ALOMAR. In *R*eviewed and Revised Papers presented at the 23rd international Laser Radar Conference,24-28 July, Nara(Japan), p. 179–182.

Frioud, Max; Gausa, Michael; Stebel, Kerstin; Hansen, Georg; Myhre, Cathrine; Singer, Werner; Latteck, Ralph; de Frutos, Angel; Cachorro, Victoria; Toledano, Carlos and Rodriguez, Edith (2006b) *O*bservation and characterization of aerosols above ALOMAR (69 degrees N) by tropospheric lidar, sun-photometer, and VHF radar. In *P*roceedings of SPIE, Vol. 6367 (SPIE).

Gayet, J.F.; I.S.Stachlewska; Jourdan, O.; Shceherbakov, V.; Schwarzenboek, A. and Neuber, R. (2007) *M*icrophysical and optical properties of precipitating drizzle and ice particles from alternated lidar and in situ measurements. Ann. Geophys., Vol. 25: p. 1487–1497.

Goldfarb, L.; Keckhut, P.; Chanin, M.-L. and A.Hauchecorne (2001) *C*irrus Climatological Results from Lidar Measurements at OHP (44°N,6°E). Geophysical Research letters.

Hedin, A.E. (2006) *M*SISE Model 1990. http://modelweb.gsfc.nasa.gov/atmos/msise.html. (Accessed: 09.04.08).

Heymsfield, Andrew J. and Platt, C.M.R. (1984) *A* Parametrisation of the Particle Size Spectrum of Ice Clouds in Terms of the Ambient Temperature and the Ice Water Content. Journal of the Atmospheric Sciences, Vol. 41(5): p. 846–855.

Intrieri, Janet M.; Stephens, Graeme L.; Eberhard, Wynn L. and Uttal, Taneil (1993) *A* Method for Determining Cirrus Cloud Particle Sizes Using Lidar and Radar Backscatter Technique. Journal of Applied Meteorology, Vol. 32(6): p. 1074–1082.

Korolev, A.V.; G.A.Isaac and J.Hallet (1999) *I*ce particle habits in arctic clouds. Geophysical research letters, Vol. 26(9): p. 1299–1302.

Kusterer, John M. (2007) *C*ALIPSO Quality Statements: Lidar Level 2 Cloud and Aerosol Layer Products Version Release 1.10. Technical report, NASA. URL: http://eosweb.larc.nasa.gov/PRODOCS/calipso/Quality_Summaries /CALIOP_L2LayerProducts.html, Last updatet: 18.12.07, accessed: 06.02.08.

Langley, NASA (2008) *C*ALIPSO Quality Statements. Technical report, NASA, Atmospheric Science Data Center, URL: http://eosweb.larc.nasa.gov/PRODOCS/calipso/Quality_Summaries/. Last Updated: 28.01.08, last accessed: 11.02.08.

Lawson, R.P.; B.A.Baker; C.G.Schmitt and T.R.Jensen (2001) *A*n overview of microphysical properties of Arctic clouds observed in May and July 1998 during FIRE ACE. Journal of geophysical research, Vol. 106(D14): p. 14,989–15,014.

Lindzen, Richard S.; Chou, Ming-Dah and Hou, Arthur Y. (2001) *D*oes the Earth Have an Adaptive Infrared Iris. Bulletin of the American Meteorological Society, Vol. 82(3): p. 417–432.

Liou, K.N. (1986) *I*nfluence of Cirrus Clouds on Weather and Climate Processes: A Global Perspective. Monthly Weather Review, Vol. 114(6): p. 1167–1199.

Liou, K.N. (2002) *A*n Introduction to Atmospheric Radiation, Vol. 84 of *I*nternational Geophysics Series, chapter 7.6, p. 427–436 (Academic Press), second edition.

Liu, Z.; Hu, Y.; Vaughan, M.; Reagan, J.; Hostetler, C.; Winker, D.; Hunt, W.; Powell, K. and Trepte, C. (2006) *V*alidation of Calipso Lidar (CALIOP) Calibration. In *I*LRC 2006 (ILRC 2006, Nara, Japan).

Liu, Zhaoyan; Omar, Ali H.; Hu, Yongxiang; Vaughan, Mark A. and Winker, David M. (2005) *C*ALIOP Algorithm Theoretical Basis Document. Part 3: Scene Classification Algorithms. Release 1.0, NASA Langley Research Center, Science Applications International Corp. (SAIC), National Institute of Aerospace (NIA), URL: http://www-calipso.larc.nasa.gov/reaources/pdfs/PC-SCI202_Part3_v1.0.pdf.

Lynch, David K.; Sassen, Kenneth; Starr, David D'O. and Stephens, Graeme (editors) (2002) *C*irrus (Oxford University Press, Inc.).

Mason, B.J. (1994) *T*he shapes of snow crystals - Fitness for purpose?. Quartery Journal of the Royal Meteorological Society.

Matthey, Renaud (2000) *D*evelopment of compact elastic backscatter lidars: from numerical simulations to atmospheric measurements. Ph.D.thesis, Universié de Neuchâtel.

Morille, Y.; Haeffelin, M.; Noel, V.; Keckhut, P.; Cadet, B.; David, C.; Jumelet, J. and Pelon, J. (2007) *C*oincident measurements between CALIPSO and IPSL ground-based Lidars (Institut Pierr-Simon Laplace, France). Poster at conference about Atrain, Lille 2007.

NOAA (2008) *N*EODAAS Satellite Information. web: http://www.sat.dundee.ac.uk/satellites.html. Accessed: 14 April 2008.

Noel, Vincent; Chepfer, Helene; Heaffelin, Martial and Morille, Yohann (2006) *C*lassification of Ice Crystal Shapes in Midlatitude Ice Clouds from Three Years of Lidar Observations over the SIRTA Observatory. Journal of the Atmospheric Sciences, Vol. 63: p. 2978–2991.

Noel, Vincent; Chepfer, Helene; Ledanois, Guy; Delaval, Arnaud and Flamant, Pierre H. (2002) *C*lassification of particle effective shape ratios in cirrus clouds based on the lidar depolarization ratio. Applied Optics, Vol. 41(21): p. 4245–4257.

Noel, Vincent; Ledanois, Guy; Chepfer, Helene and Flamant, Pierre H. (2001) *C*omputation of a single scattering matrix for nonspherical particles randomly or horizontally oriented in space. Applied Optics, Vol. 40(24): p. 4365–4375.

Noel, Vincent; Winkler, David M.; McGill, Matthew and Lawson, Paul (2004) *C*lassification of particle shapes from lidar depolarization ratio in convective ice clouds compared to in situ observations during CRYSTAL-FACE. Journal of Geophysical research, Vol. 109.

Orbital (2007) *F*act Sheet: OCO Orbiting Carbon Observatory. Technical report, Orbital Sciences Corporation, URL: http://www.orbital.com/NewsInfo/Publications/OCO_fact.pdf. Accessed: 22.01.08.

Platt, C.M.; Young, S.A.; Carswell, A.I.; Pal, S.R.; MCCormick, M.P.; Winkler, D.M.; DelGuasta, M.; Stefanutti, L.; Eberhard, W.L.; Hardesty, M; Flamant, P.H.; Valentin, R.; B.Forgan; G.G.Gimmestad; Jäger, H.; Khmelevtsov, S.S.; Kolev, I.; Kaprieolev, B.; ren Lu, Da; Sassen, K.; Shamanaev, V.S.; Uchino, O.; Mizuno, Y.; Wandinger, U.; Weitkamp, C.; Ansmann, A. and Wooldridge, C. (1994) *T*he Experimental Cloud Lidar Pilot Study (ECLIPS) for Cloud-Radiation Research. Bulletin of the American Meteorological Society, Vol. 75(9): p. 1635–1654.

Ramanathan, V. and Collins, W. (1991) *T*hermodynamic regulation of ocean warming by cirrus clouds deduced from observations of the 1987 El Niño. Nature, Vol. 351: p. 27–32.

Rogers, R.R. and Yau, M.K. (1989) *A* Short Course in Cloud Physics, Vol. 113 of *I*nternational Series in Natural Philosphy (Butterworth and Heinemann), third edition. Reprinted 1996.

Sassen, K. (1991) *T*he Polarization Lidar Technique for cloud research: A review and current assessment. Bulletin of the American Meteorological Society, Vol. 72(12): p. 1848–1866.

Schotland, R.M.; Sassen, K. and Stone, R. (1971) *O*bservations by Lidar of Linear Depolarization Ratios for Hydrometeors. Journal of Applied Meteorology, Vol. 10(5): p. 1011–1017.

SPEC (2008) *S*PEC inc. Innovation in Atmospheric Science Instrumentation. web: http://www-specinc.com/. Accessed: 11 April 08.

Stordal, F.; Myhre, G.; Stordal, E.J.G.; Rossow, W.B.; Lee, D.S.; Arlander, D.W. and Svendby, T. (2005) *I*s there a trend in cirrus cloud cover due to aircraft traffic?. Atmos. Chem. Phys., Vol. 5: p. 2155–2162.

Vaughan, Mark A.; Winker, David M. and Powell, Kathleen A. (2005) *C*ALIOP Algorithm Theoretical Basis Document. Part 2: Feature Detection and Layer Properties Algorithms. Release 1.01, NASA Langley Research Center, Science Applications International Corp. (SAIC), URL: http://www-calipso.larc.nasa.gov/reaources/pdfs/PC-SCI202_Part2_rev1x101.pdf.

Veerabuthiran, S. (2003a) *E*xploring the Atmosphere with Lidars: 1. Basics and Applications. Resonance, Vol. 8(4): p. 33–43.

Veerabuthiran, S. (2003b) *E*xploring the Atmosphere with Lidars: 2. Types of Lidars. Resonance, Vol. 8(5): p. 47–51.

Waagen Hans, met.no (2006) *K*lassifisering av skyer. http://met.no/met/met_lex/q_u/skyklassifisering/index.html. (in Norwegian, Accessed: 20.01.08.

Wallace, John M. and Hobbs, Peter V. (1977) *A*tmospheric Science an Introductory Survey (Academic Press).

Wang Pao, K. (2002) *I*ce Microdynamics (Academic Press). This volume is a paperback reprint of Pao K. Wang's article that appears in volume 45 of Advances in Geophysics.

Whiteway, James; Cook, Clive; Gallagher, Martin; Choularton, Tom; Harries, John; Connolly, Paul; Busen, Reinhold; Bower, Keith; Flynn, Michael; May, Peter; Aspey, Robin and Hacker, Jorg (2004) *A*natomy of cirrus clouds: Results from the Emeral airborne campaigns. Geophysical research letters, Vol. 31(L24102).

Winker, David M.; Hostetler, Chris A; Vaughan, Mark A. and Omar, Ali H. (2006) *C*ALIOP Algorithm Theoretical Basis Document. Part 1: CALIOP Instrument and Algorithms Overview. Release 2.0, NASA Langley Research Center, Science Applications International Corp. (SAIC), URL: http://www-calipso.larc.nasa.gov/reaources/pdfs/PC-SCI202.Part1_v2-Overview.pdf.

Winker, David M.; Pelon, Jacques and McCormick, M Patrik (2003) *T*he CALIPSO mission: Spaceborne lidar for observation of aerosols and clouds. In *P*roc. SPIE Int. Soc. Opt. Eng., Vol. 4893, p. 1–11.

Young, Andrew T. (1982) *R*ayleigh scattering. Physics today, Vol. 35: p. 42–48.

Zhang, Yuying and Mace, Gerald G. (2006) *R*etrieval of Cirrus Microphysical Properties with a Suite of Algorithms for Airborne and Spaceborne Lidar,Radar, and Radiometer Data. Journal of Applied Meteorology and Climatology, Vol. 45(12): p. 1665–1689.